AD-A123 396 PARAMETERIZATION OF BROADBAND SOLAR RADIATION TRANSFER IN CLEAR AND CLOUD.. (U) UTAH UNIV SALT LAKE CITY DEPT OF METEOROLOGY K HUTCHISON ET AL. 30 SEP 82 1/2

UNCLASSIFIED SCIENTIFIC-1 AFGL-TR-82-0364 F/G 4/1 NL

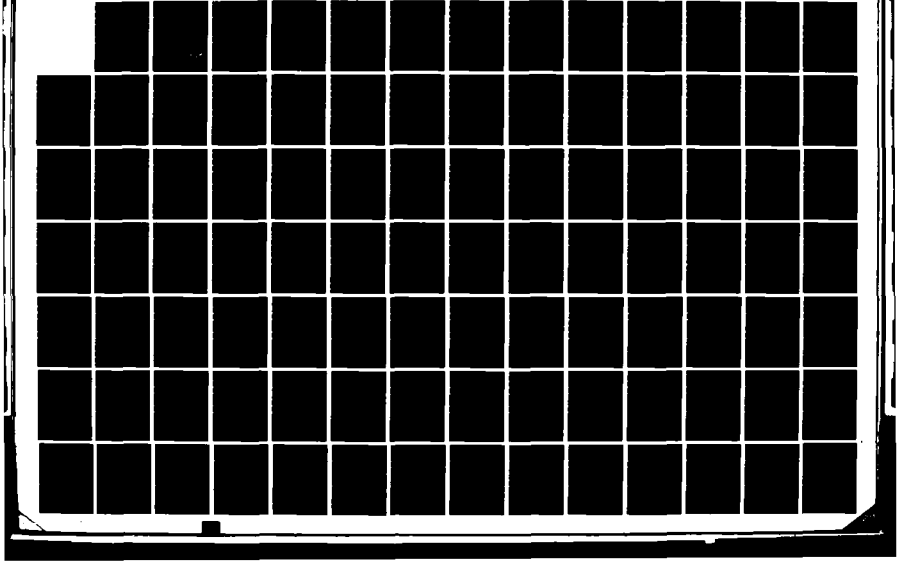

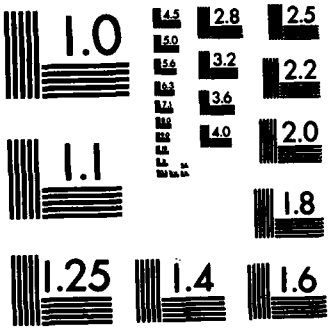

(12)

AFGL-TR-82-0364

AD A123396

PARAMETERIZATION OF BROADBAND SOLAR RADIATION TRANSFER IN CLEAR AND CLOUDY ATMOSPHERES

by

Keith Hutchison and Kuo-Nan Liou

Department of Meteorology

University of Utah

Salt Lake City, Utah 84112

30 September 1982

Scientific Report for Period

1 August 1981 to 30 September 1982

Approved for public release; distribution unlimited

AIR FORCE GEOPHYSICS LABORATORY

AIR FORCE SYSTEMS COMMAND

UNITED STATES AIR FORCE

HANSCOM AFB, MASSACHUSETTS 01731

Unclassified

SECURITY CLASSIFICATION OF THIS PAGE *(When Data Entered)*

REPORT DOCUMENTATION PAGE		READ INSTRUCTIONS BEFORE COMPLETING FORM
1. REPORT NUMBER AFGL-TR-82-0364	2. GOVT ACCESSION NO. AD-A123 386	3. RECIPIENT'S CATALOG NUMBER
4. TITLE *(and Subtitle)* PARAMETERIZATION OF BROADBAND SOLAR RADIATION TRANSFER IN CLEAR AND CLOUDY ATMOSPHERES		5. TYPE OF REPORT & PERIOD COVERED Scientific Report No. 1 8/1/81 - 9/30/82 6. PERFORMING ORG. REPORT NUMBER
7. AUTHOR(s) Keith Hutchison Kuo-Nan Liou		8. CONTRACT OR GRANT NUMBER(s) F19628-81-K-0042
9. PERFORMING ORGANIZATION NAME AND ADDRESS Department of Meteorology University of Utah Salt Lake City, Utah 84112		10. PROGRAM ELEMENT, PROJECT, TASK AREA & WORK UNIT NUMBERS 62101F 2310G7AA
11. CONTROLLING OFFICE NAME AND ADDRESS Air Force Geophysics Laboratory Hanscom AFB, Massachusetts 01731 Contract Monitor/Samuel Yee/LYP		12. REPORT DATE 30 September 1982 13. NUMBER OF PAGES 114
14. MONITORING AGENCY NAME & ADDRESS*(if different from Controlling Office)*		15. SECURITY CLASS. *(of this report)* Unclassified 15a. DECLASSIFICATION/DOWNGRADING SCHEDULE

16. DISTRIBUTION STATEMENT *(of this Report)*

Approved for public release; distribution unlimited.

17. DISTRIBUTION STATEMENT *(of the abstract entered in Block 20, if different from Report)*

18. SUPPLEMENTARY NOTES

19. KEY WORDS *(Continue on reverse side if necessary and identify by block number)*

Solar radiation
Radiative transfer
Parameterization
Cloud
Global dynamic model

20. ABSTRACT *(Continue on reverse side if necessary and identify by block number)*

This report describes a parameterization model for computing solar heating rate and net flux profiles in clear and cloudy atmospheres. Specifically, the model is designed to allow global circulation and climate modelers maximum flexibility when treating the effects of clouds on the atmosphere. Gaseous water vapor, ozone and carbon dioxide are the absorbers considered in the clear atmosphere. The effect of Rayleigh scatter on net flux profiles is also discussed. The parameterization method is compared with results

DD FORM 1 JAN 73 1473 EDITION OF 1 NOV 65 IS OBSOLETE

Unclassified

SECURITY CLASSIFICATION OF THIS PAGE *(When Data Entered)*

obtained by the discrete ordinate method and the comparisons for heating rate and net flux profiles are excellent for all solar zenith angles and surface albedos in the range 0.0-1.0. Reflection and transmission for cumulus, altostratus, cirrus and stratus are parameterized to allow variations in solar zenith angle, cloud thickness, and mean cloud temperature. The latter dependence means the cloud base becomes an independent variable.

TABLE OF CONTENTS

Section 1

INTRODUCTION

With the advent of high speed computers, complicated and intricate equations governing the transfer of solar radiation in clear and cloudy atmospheres can be solved numerically with high accuracy (see, e.g., Freeman and Liou, 1979). However, computation time requirements for the rigorous solutions to transfer equations and processes negate their usefulness in atmospheric dynamic and climate models with their large number of grid points and extended time integrations. Consequently, new economic and efficient yet accurate methods of introducing the effects of solar heating on the dynamics of the atmosphere must be sought to replace highly theoretical techniques.

Simplified methods to account for the solar radiation transfer in the atmosphere were presented by Manabe and Möller (1961) and subsequently by Manabe and Strickler (1964) which were incorporated in a general circulation model (GCM) developed at the Geophysical Fluid Dynamics Laboratory. Moreover, early attempts to include clouds in GCM involved assigning radiative properties to clouds based upon the climatological data such as those provided by Haurwitz (1948). Katayama (1972) followed this approach with a highly detailed parameterization which he developed for the GCM used at the University of California at Los Angeles. Katayama used empirical relations to represent absorption by water vapor, Rayleigh scattering, and attenuation by dust. His work was recently cited in the text by Haltiner and Williams (1979). Sasamori

(1972) likewise took this very simple approach to the problem of clouds when developing his solar radiation program which forms the basis for solar radiation input to the GCM used at the National Center for Atmospheric Research (NCAR).

Parameterized solar radiation schemes began to appear more sophisticated with the one developed by Lacis and Hansen (1974) for the GCM developed at the Goddard Institute for Space Studies (Sommerville et al., 1974). Their parameterization involved determining empirical formulae which accurately fit ozone and water vapor absorptivity measurements and using the two stream approximation to determine the reflectivity and transmissivity of a cloud directly from its optical path. Multiple scattering effects were approximately taken into account. However, in addition to the inherent inaccuracy of the two stream approximation, their assumption that all solar flux was diffuse after contacting a cloud, led to large heating rate errors below optically thin clouds such as cirrus. Additionally, use of the two stream approximation automatically omitted the solar angle dependence of cloud transmission and reflection. Recently, Fouquart and Bonnel (1981) presented a new parameterization for solar radiation which is used in the GCM at the Laboratory of Meteorology in Paris. The results they show are generally similar to those of Lacis and Hansen; however, detailed verification of their method was not given. Even fewer results are given by Geleyn and Hollingsworth (1979) of their radiation method which is used in the GCM at the European Center for Medium Range Weather Forecasts.

While each of the aforementioned schemes appears adequate in the context of computational requirements, verification of its accuracy is

minimal at best. Additionally, many simplifications in these models appear to be justified only by the results and have not been based upon physical and mathematical laws which govern the radiation field in planetary atmospheres. Finally, solar radiation interactions with clouds in general and high clouds in particular have not been accurately treated in these models.

In this report, a new parameterization approach for the transfer of solar radiation in the atmosphere is developed and is intended for use in a general circulation model. Effects of direct and diffuse radiation in clear and cloudy atmospheres will be separately treated, thus minimizing heating rate errors which normally occur below optically thin clouds. Heating rate calculations will be obtained at specific points through an analytic approach rather than the computationally more time-consuming and inaccurate finite difference schemes. Cloud reflection and transmission will be determined from vertical liquid water content and mean cloud temperature which affects the gaseous absorptivity within the cloud. Additionally, a solar zenith angle dependence for these properties will also be given. Finally, the present parameterization model will allow the internal fluxes within cloudy atmospheres to be determined. Ample verification of each aspect of the model will be presented.

Section 2 discusses general properties of an absorbing and scattering atmosphere, justifies the gases considered in the model and presents scattering characteristics of typical water and ice clouds. In the third Section, theoretical aspects of computing heating rates in a clear and cloudy atmosphere are shown. The basic radiative transfer equation in a scattering atmosphere is derived and the discrete

ordinate method (DOM) of solving it is discussed. In addition, changes which have been made in cloud reflection and transmission definitions given by Liou (1976) and alterations to the four stream DOM program developed by Freeman and Liou (1979) are listed. These changes are required so that consistent comparisons between results derived from a more exact radiation program and those from the parameterization method can be made. Theoretical justifications for this parameterization model are expressed at the beginning of Section 4. This is followed by analytical expressions for water vapor, ozone, and carbon dioxide heating rates and numerous graphs which show results obtained in a clear atmosphere. Parameterization of solar radiation transfer in a single cloud layer is covered in Section 5. Finally, the last Section summarizes the significance of the present parameterization method.

Section 2

ABSORPTION PROPERTIES OF ATMOSPHERIC GASES

2.1 Composition of the Atmosphere

The atmosphere is composed of a group of nearly permanent gases and a group of gases with variable concentration. In addition, it also contains various solid and liquid particles such as aerosols, water drops and ice crystals which are highly variable in space and time. Table 1 lists the concentration of the permanent and variable gases in the earth's atmosphere as shown by Liou (1980).

The mixing ratio of each permanent gas is constant from the earth's surface up to an altitude of about 60 km; however, it should be recognized that the concentration of carbon dioxide actually varies as a result of the combustion of fossil fuels and photosynthesis processes. The concentration of water vapor and ozone are highly variable in space and time. Water vapor density generally decreases with height in the troposphere while ozone has a maximum concentration in the 15-25 km region.

2.2 Gaseous Absorption

Absorption spectra due to electronic transitions of molecular and atomic oxygen and nitrogen, and ozone occur in the ultraviolet (UV) region of the solar spectrum while those due to vibrational and

Table 1. The Composition of the Atmosphere.

Permanent Constituents		Variable constituents	
Constituent	& by volume	Constituent	% by volume
Nitrogen (N_2)	78.084	Water vapor (H_2O)	0 - 0.04
Oxygen (O_2)	20.948	Ozone (O_3)	0 - $12x10^{-4}$
Argon (Ar)	0.934	Sulfur dioxide	$0.001x10^{-4}$*
Carbon dioxide (CO_2)	0.033	Nitrogen dioxide (NO_2)	$0.001x10^{-4}$*
Neon (Ne)	$18.18x10^{-4}$	Ammonia (NH_3)	$0.004x10^{-4}$*
Helimn (He)	$5.24x10^{-4}$	Nitric oxide (NO)	$0.0005x10^{-4}$*
Krypton (Kr)	$1.14x10^{-4}$	Hydrogen sulfide (H_2S)	$0.00005x10^{-4}$*
Xenon (Xe)	$0.089x10^{-4}$	Nitric acid vapor (HNO_3)	trace
Hydrogen (H_2)	$0.5x10^{-4}$		
Methane	$1.5x10^{-4}$		
Nitrous oxide (N_2O)*	$0.27x10^{-4}$		
Carbon monoxide (CO)*	$0.19x10^{-4}$		

*Concentration near the earth's surface.

rotational transitions of triatomic molecules such as H_2O, CO_2, and ozone lie in the infrared (IR) region. Figure 1 depicts the solar spectrum measured at the top of the atmosphere (Thekaekara, 1974), the earth's surface, and the areas of atmospheric absorption. Absorption of UV radiation occurs primarily in the stratosphere and mesosphere while energy in the longer wavelengths is absorbed in the troposphere.

Of the gases in the upper atmosphere, only ozone strongly absorbs at wavelengths above 2000 Å where significant solar energy is found. The ozone absorption spectrum begins at 2000 Å and continues to 11800 Å. The area of strongest absorption occurs between 2000-3000 Å in the Hartley band complex. Another area of strong ozone absorption is found in the Huggins band complex located in the 3000-3600 Å region. These bands are characterized by highly variable absorption coefficients. The much weaker Chappius bands absorb in the 4400-11800 Å band interval.

Water vapor is the most important absorber in the near infrared region of the solar spectrum and it almost exclusively is responsible for atmospheric heating below 10 kilometers. This absorption occurs in six bands. They are the overtone and combination bands centered at 0.94, 1.1, 1.38, and 1.87 μm, the 2.7, and 3.2 μm bands. Although the 2.7 μm band is the most important, significant absorption also occurs in the 3.2 μm band and the overtone and combination bands. One additional water vapor absorption band is located at 6.3 μm where a negligible solar flux is observed.

Carbon dioxide exhibits a number of weak absorption bands in the near IR region of the solar spectrum. Those centered at 5.1, 4.8, 4.3, 2.0, 1.6, and 1.4 μm are very weak and can be ignored. The 2.7

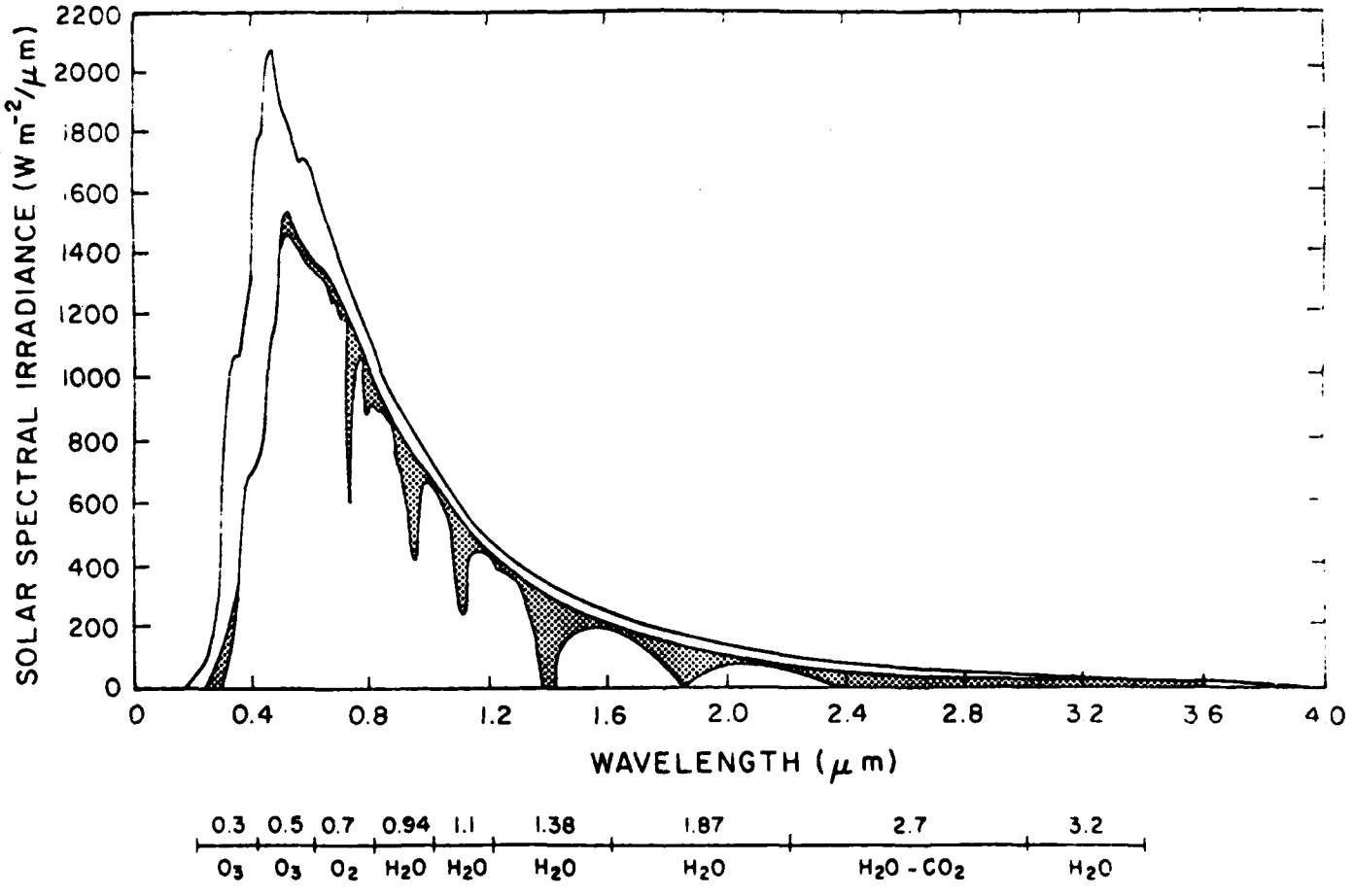

Fig. 1. Spectral energy curve at the top of the atmosphere. Spectral bands used in the solar radiation program are indicated. The inner curve is the solar spectrum at the bottom of the atmosphere, and shaded areas are absorption bands. (After Liou, 1980.)

μm band is somewhat stronger. Carbon dioxide absorption is complicated in this band since it overlaps with the 2.7 μm water vapor band.

Oxygen absorbs very strongly, as does nitrogen, at wavelengths smaller than 2000 Å but Park and London (1974) have demonstrated that it is of minor importance in heating rate calculations below 75 kilometers. Since the area of interest in this study extends to only 60 km, this research will concentrate on gaseous absorption by water vapor, ozone and carbon dioxide.

2.2.1 Absorption by Ozone

In the 15-60 km region, atmospheric heating results primarily from the absorption of solar radiation by ozone. Ozone absorption occurs in two complex band systems as shown in Figs. 2 and 3. In the Hartley and Huggins bands (2000-3600 Å), ozone absorbs very strongly while it absorbs much less strongly in the Chappius bands (4400-11800 Å).

Ozone absorption was modeled by an absorbing layer overlaying a reflecting layer as described by Lacis and Hansen (1974). The spectral absorptivity for the solar flux having a cosine of solar zenith angle μ_0 and corresponding to an ozone path length u_3 (cm NTP) is

$$A_{\nu i} = 1 - e^{-k_i u_3/\mu_0} , \qquad (1)$$

where k_i is the monochromatic ozone absorption coefficient after Inn and Tanaka (1953) and Vigroux (1953) as compiled by Howard (1961). These data are listed in Table 2. Absorption coefficients in the Hartley and Huggins band complex have a temperature dependence (data listed correspond to -44° C) while those in the Chappius band

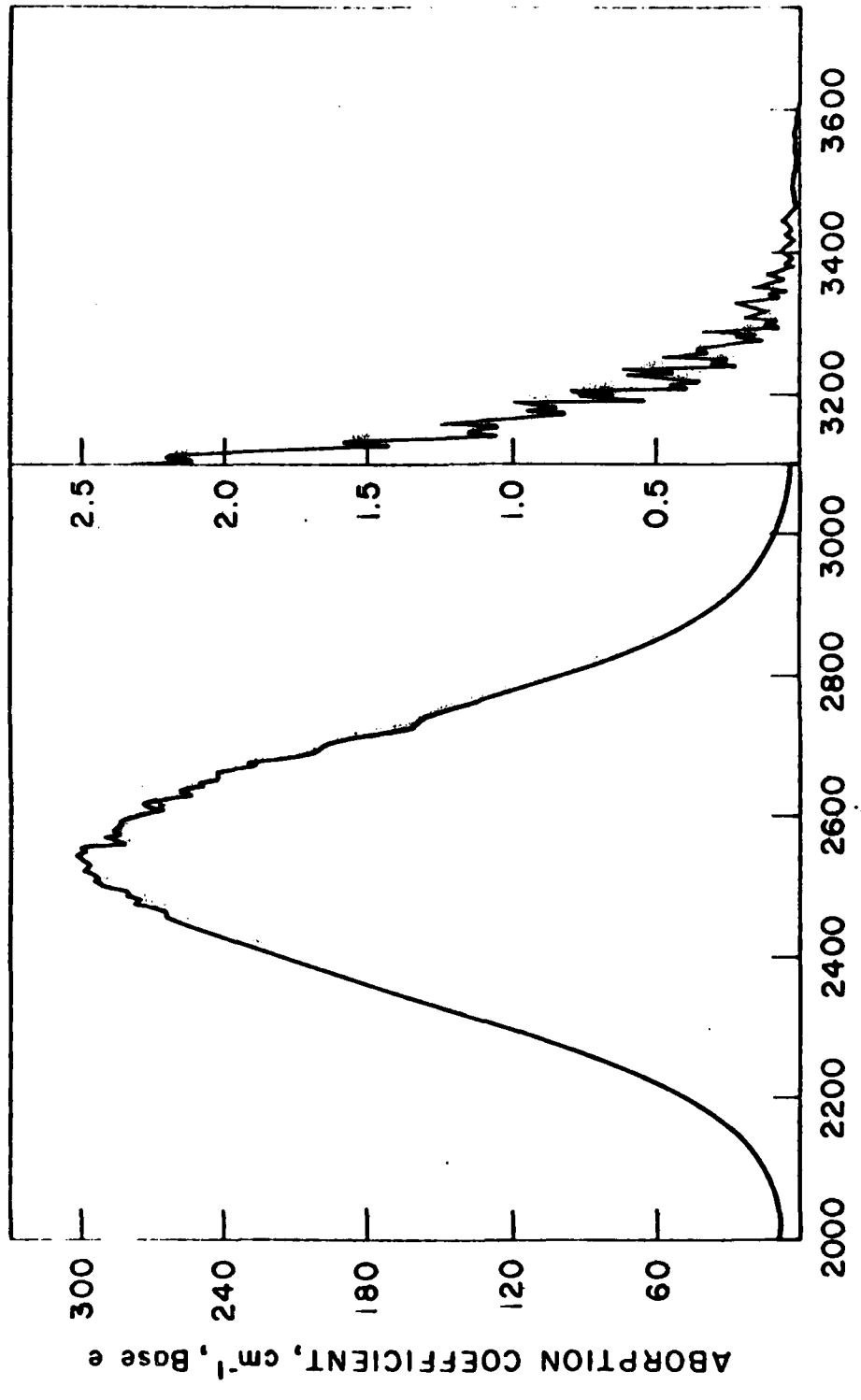

Fig. 2. Absorption spectrum for ozone in the Hartley and Huggins band complex from 2000 to 3600 Å.

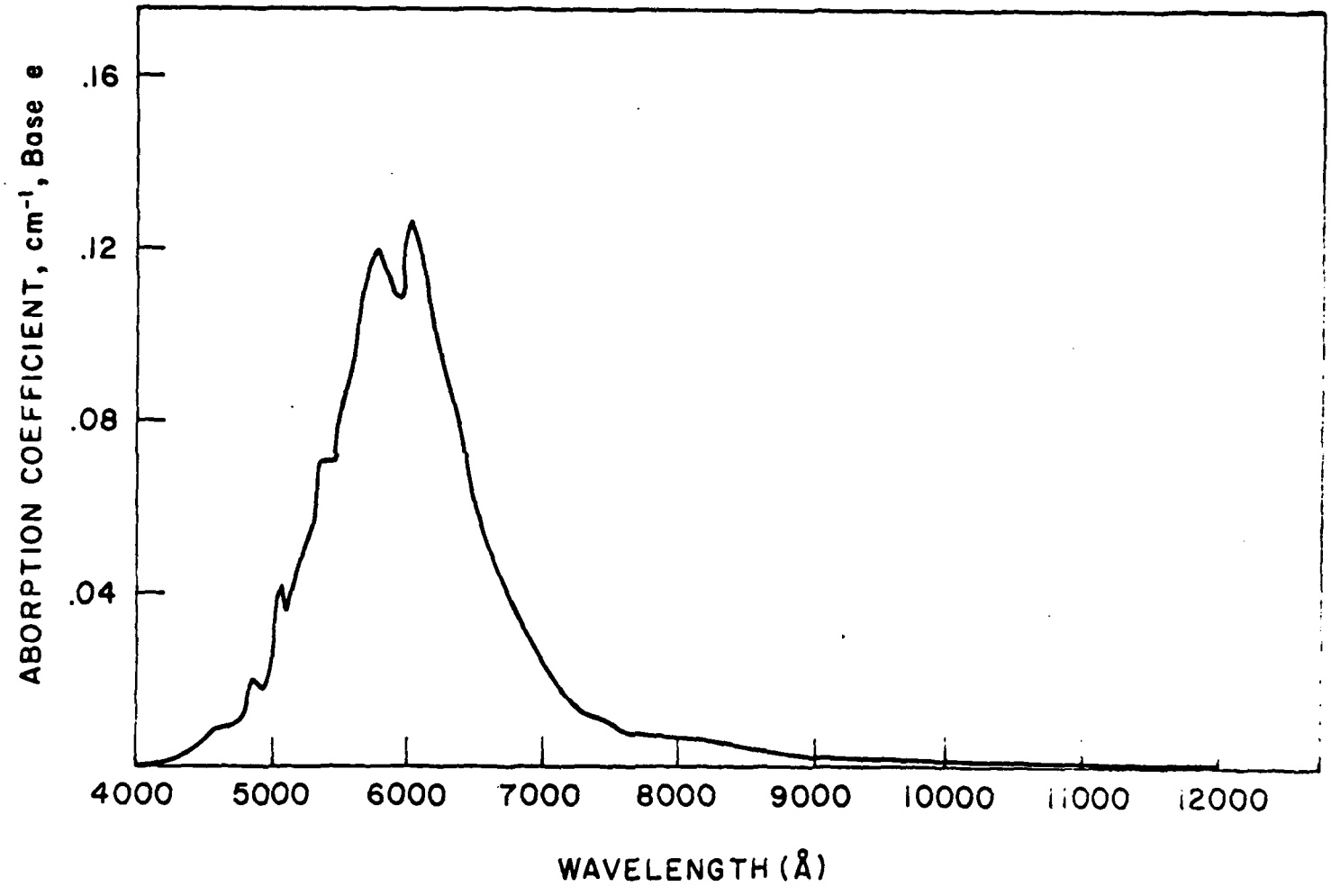

Fig. 3. Absorption spectrum for ozone in the Chappius band complex from 4000 to 11800 Å.

Table 2. Monochromatic Absorption Coefficients for Ozone.

$\lambda(\mu m)$	$A_\nu(cm^{-1})$
.20	8.61
.21	14.7
.22	48.4
.23	122.0
.24	216.0
.25	299.0
.26	292.0
.27	210.0
.28	106.0
.30	10.1
.32	.898
.34	6.40×10^{-2}
.36	1.80×10^{-3}
.45	3.50×10^{-3}
.50	3.45×10^{-2}
.55	9.20×10^{-2}
.60	.132
.65	6.20×10^{-2}
.70	2.30×10^{-2}
.80	1.00×10^{-2}

complex have practically no temperature dependence. Absorption coefficients for wavelengths greater than 8000 Å are very small and are neglected in ozone heating calculations.

A few words are in order about the units used to express ozone density, since it can be quite confusing. The familiar cgs units of gm cm^{-3} are seldom used in ozone calculations but an older unit which is frequently used is the 10^{-3} cm NTP km^{-1}. The conversion is

$$\rho_3(g\ cm^{-3}) = 21.4\ \rho_3\ (10^{-3}\ cm\ NTP\ km^{-1})\ . \qquad (2)$$

2.2.2 Water Vapor Absorption

Howard et al. (1956) published results of extensive laboratory experiments which measured the total absorption of the 0.94, 1.1, 1.38, 1.87, 2.7, and 3.2 μm water vapor bands for various path lengths and under different atmospheric pressures. They derived two formulas for this total absorption. For small values of total absorption

$$A = \int A_\nu d\nu = c u_1^{1/2}\ (P_a + e)^k\ ,\quad A > A_c \qquad (3)$$

and for large values of total absorption

$$A = \int A_\nu d\nu = C + D \log u_1 + K \log (P_a + e)\ ,\quad A > A_c \qquad (4)$$

where ν is the wavenumber (cm^{-1}), A the band area (cm^{-1}), A_ν the fractional absorption within the band at ν, u_1 the water vapor path length (g cm^{-2}), e the partial pressure of the absorbing gas (mm Hg), P_a the partial pressure of the non-absorbing gases (mm Hg), A_c the critical band area above which the strong band equation [Eq. (2)] applies, and c, k, C, D, and K are empirical constants listed in Table 3.

Table 3. Empirical Constants for H_2O Bands.

H_2O band $\lambda(\mu m)$	c	k	C	D	K	A (cm^{-1})	$\Delta\nu$ (cm^{-1})	K/D	x_0
0.94	38	0.27	-135	230	125	200	1400	0.54	3.86
1.1	31	0.26	-292	345	180	200	1000	0.52	7.02
1.38	163	0.30	202	460	198	350	1500	0.43	0.36
1.87	152	0.30	127	232	144	257	1100	0.62	0.28
2.70	316	0.32	337	246	150	200	1000	0.62	0.04
3.20	40.2	0.32	-144	295	151	500	540	0.51	3.25

Since these two formulas were not continuous when $A = A_c$, Liou and Sasamori (1975) derived a single formula to approximate the mean band absorptivity, $A_{\bar{\nu}}$, for both weak and strong absorptivity in the following form:

$$A_{\bar{\nu}} = A/\Delta\nu = \frac{1}{\Delta\nu} [C + D \log_{10} (x + x_0)] , \tag{5}$$

where

$$x = u_1 \bar{P}_a^{K/D} , \tag{6}$$

$$x_0 = 10^{-C/D} , \tag{7}$$

and

$$\bar{P} = \int_0^{u_1} P(u)\, du \;/\; \int_0^{u_1} du . \tag{8}$$

The reduced pressure accounts for the pressure dependence of absorption in a non-homogeneous atmosphere. It is an empirical method and places all the absorbing matter along a pressure gradient at one pressure, $\bar{P}$.

2.2.3 Absorption by Carbon Dioxide

As previously indicated in Table 1, CO_2 was assumed to be a permanent constituent in the atmosphere with a mixing ratio of 330 parts-per-million (ppm) by volume. It absorbs solar radiation most strongly in the 2.7 μm band region where it overlaps with water vapor. Other minor CO_2 absorption bands occur at 1.4, 1.6, 2.0, 4.3, 4.8, and 5.2 μm, but were neglected because absorption is very weak in comparison with water vapor absorption.

Howard et al. (1956) also measured the total absorptivity of each CO_2 band and developed formulas to approximate it. Similarly, Liou and Sasamori (1975) combined these formulae into Eq. (5). The pertinent constants are listed in Table 4 for CO_2. Absorber path length units for CO_2 are in cm-atm.

In another of the series of papers published on gaseous absorption by Howard et al. (1956), they theorized the accepted method for computing the total absorptivity due to water vapor and carbon dioxide overlapping in the same spectral region. The total gaseous absorption in the 2.7 μm water vapor and carbon dioxide overlap band was given as

$$\int_\nu A_\nu(H_2O + CO_2)\, d\nu = \int_\nu A_\nu(H_2O)\, d\nu + \int_\nu \delta\, A_\nu(CO_2)\, d\nu \,, \qquad \nu = 2.7\ \mu m \qquad (9)$$

where δ *is a weighting factor which ranges between 0 and 1, depending* on the total water vapor absorptivity in the 2.7 μm band. Its values are given in Fig. 4. The values of δ were calculated using one of the following equations after assuming Fig. 4 could be described accurately by two straight lines. If the total water vapor absorption, $A_5(u_1/\mu_0)\ \Delta\nu_5$, in the band is greater than or equal to 300 cm^{-1},

$$\delta = -\frac{0.7}{200} A_5(u_1/\mu_0)\ \Delta\nu_5 + 1.0 \,, \qquad (10)$$

otherwise

$$\delta = -\frac{0.3}{200} [A_5(u_1/\mu_0)\ \Delta\nu_5 - 300)] + 0.3 \,, \qquad (11)$$

Table 4. Empirical Constants for CO_2 Bands

CO_2 band $\lambda(\mu m)$	c	k	C	D	K	A_c (cm^{-1})	$\Delta\nu$ (cm^{-1})	K/D	x_0
1.4	0.058	0.41	----	----	----	80	600	----	----
1.6	0.963	0.38	----	----	----	80	550	----	----
2.0	0.492	0.39	-536	138	114	80	450	----	----
2.7	3.15	0.43	-137	77	68	50	320	.88	60.15
4.3	----	----	27.5	34	31.5	50	340	----	----
4.8	0.12	0.37	----	----	----	60	180	----	----
5.2	0.024	0.40	----	----	----	30	110	----	----
15.0	3.16	0.44	----	----	----	50	250	----	----

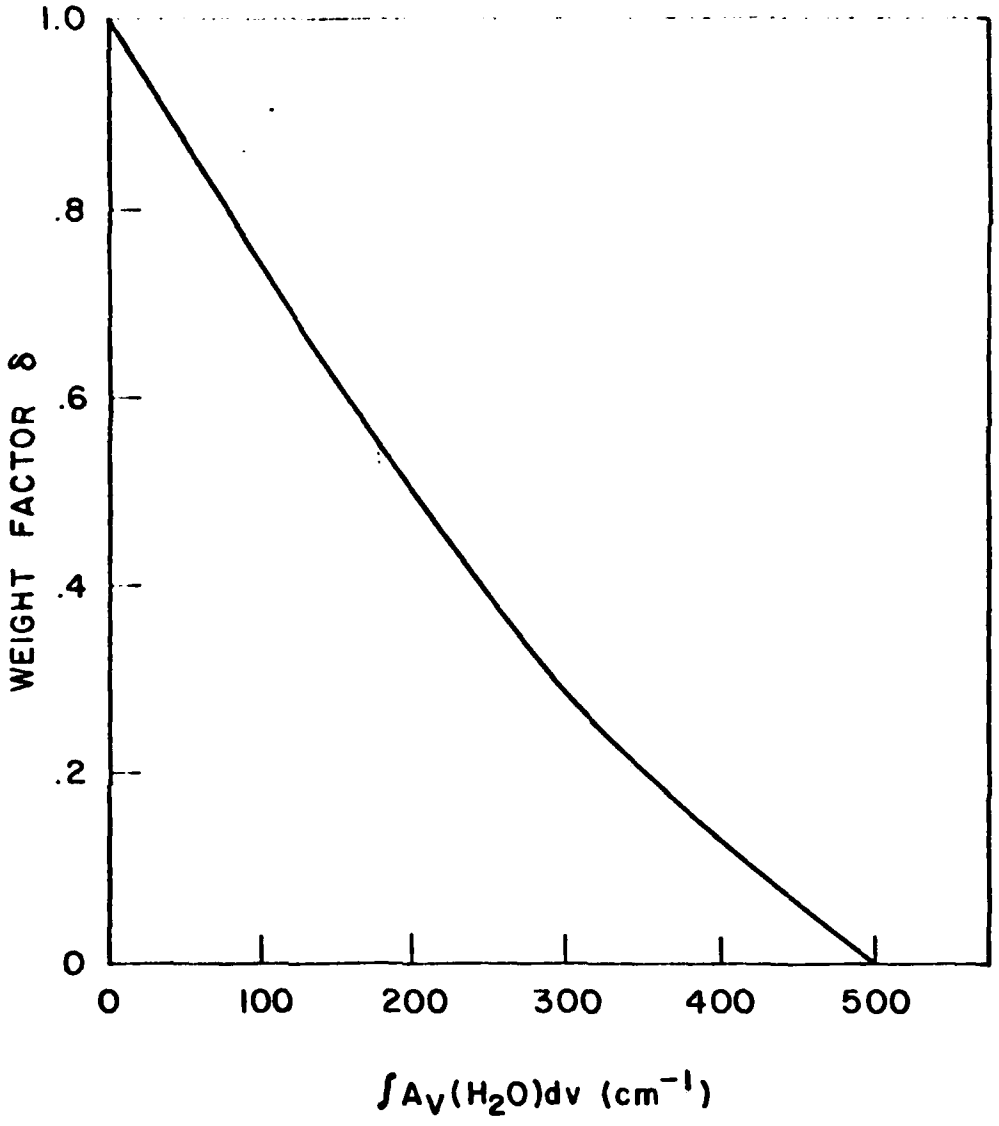

Fig. 4 Carbon dioxide weight factor as a function of total water vapor absorption in 2.7 μm band.

Section 3

RADIATIVE TRANSFER IN THE ATMOSPHERE

3.1 General

The exact solution to the radiative transfer equation can be computed with high accuracy if computational time constraints are not important. This section discusses the derivation of the radiative transfer equation (RTE) for diffuse intensity in a plane-parallel atmosphere, the discrete-ordinate method (DOM) of approximating the exact solution to the RTE, the four stream DOM analytical solution and modifications made to the University of Utah's four stream DOM program used for comparison with the parameterized model.

The concepts discussed in the derivation of the RTE for diffuse intensity in a plane-parallel atmosphere follow closely the description given in Liou (1980).

3.2 Derivation of the Radiative Transfer Equation for Diffuse Intensity in a Plane-Parallel Atmosphere

In a plane-parallel atmosphere, the differential diffuse intensity in a directional stream of radiation defined by a solid angle is reduced by single scattering of energy out of the direction $\vec{\Omega}$ and absorption by gases and particles. This is expressed by

$$dI(z,\vec{\Omega}) = - \bar{\sigma}_e \frac{N}{\cos\theta} I(z,\vec{\Omega})\, dz \ , \qquad (12)$$

where dz is the differential thickness of a layer, $\bar{\sigma}_e$ the mean extinction

cross section of a particle, N the total number of particles per volume, and $\vec{\Omega}$ the directional element of solid angle that represents the pencil of radiation (see Fig. 5). $\vec{\Omega}$ is described by azimuth, ϕ, and zenith, μ, angles. Meanwhile, the differential diffuse intensity in the direction $\vec{\Omega}$ may be increased by multiple scattering of radiation in the direction $\vec{\Omega}'$. This is given by

$$dI(z,\vec{\Omega}) = \frac{\bar{\sigma}_s N}{\cos\theta} dz \int_{\Omega'} I(z,\vec{\Omega}') \frac{P(\vec{\Omega},\vec{\Omega}')}{4\pi} d\Omega' \quad , \tag{13}$$

where $\bar{\sigma}_s$ is the mean scattering cross section and the phase function, $P(\vec{\Omega},\vec{\Omega}')$, introduces the appropriate radiation stream from $\vec{\Omega}'$ to $\vec{\Omega}$. Thus integration over all solid angles gives all possible contributions of multiply scattered energy from $\vec{\Omega}'$ to $\vec{\Omega}$. Finally, the differential diffuse intensity in direction $\vec{\Omega}$ may be increased by single scattering of the direct solar radiation whose direction is represented by $-\vec{\Omega}_0$, where the minus sign denotes the downward direction of the direct solar beam. If the direct solar flux arriving at level z is F(z), then this effect is given by

$$dI(z,\vec{\Omega}) = \frac{\bar{\sigma}_s N dz}{\cos\theta} F(z) \frac{P(\vec{\Omega},-\vec{\Omega}_0)}{4\pi} \quad , \tag{14}$$

where

$$F(z) = \pi F_0 \exp\left\{ - \frac{1}{\cos\theta_0} \int_z^\infty \bar{\sigma}_e(z') N(z') dz' \right\} \quad , \tag{15}$$

and πF_0 is the flux of solar energy arriving at the top of the atmosphere at angle θ_0 to the local zenith. Upon combining these three terms and introducing the optical depth, τ, we get

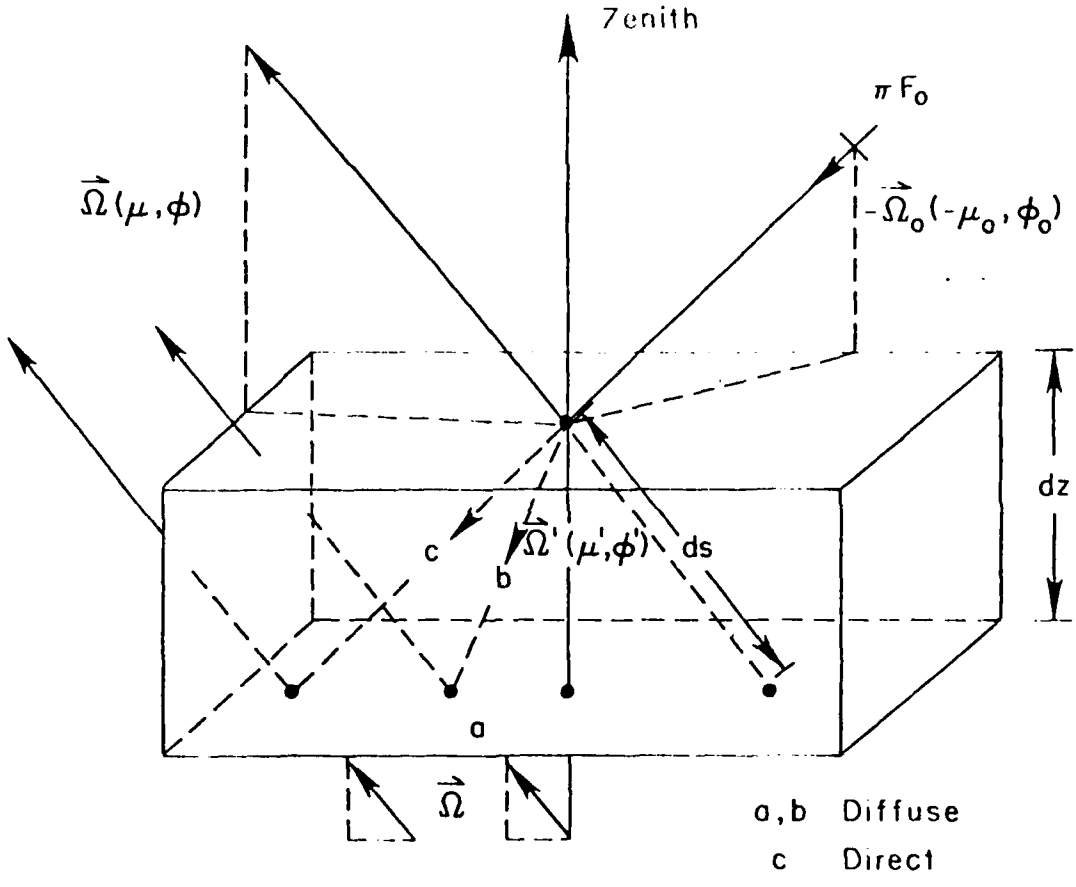

Fig. 5 Transfer of solar radiation in plane-parallel layers.
a: attenuation by extinction, b: multiple scattering,
c: single scattering of the unscattered solar flux.

$$\frac{dI(\tau,\vec{\Omega})}{d\tau} = I(\tau,\vec{\Omega}) - \frac{\tilde{\omega}}{4\pi}\int_{\Omega} I(\tau,\vec{\Omega}')\ P(\vec{\Omega},\vec{\Omega}')\ d\Omega'$$

$$- \frac{\tilde{\omega}}{4\pi}\ \pi F_0\ P(\vec{\Omega},-\vec{\Omega}_0)\ e^{-\tau/\mu_0}\ , \qquad (16)$$

where

$$\tau = \int_z \bar{\sigma}_e(z')\ N(z')\ dz'\ , \qquad (17)$$

and

$$d\tau = -\ \bar{\sigma}_e\ N(z)\ dz\ . \qquad (18)$$

The single scattering albedo $\tilde{\omega}$ is defined as the ratio of scattering cross section σ_s to extinction cross-section σ_e. In this report, we describe for documentation purposes the discrete-ordinates method for the solution of the radiative transfer equation governing the inhomogeneous gaseous atmosphere.

3.3. The Discrete-Ordinates Method

3.3.1 Intensity in a Non-Homogeneous Atmosphere

Since only fluxes are needed in the calculation of solar heating rates, Eq. (16) may be written for the azimuthally independent diffuse intensity of solar radiation in a plane-parallel homogeneous layer, ℓ, as

$$\mu \frac{dI^{\ell}}{d\tau} = I^{\ell}(\tau,\mu) - \frac{1}{2}\int_{-1}^{+1} P^{\ell}(\mu,\mu')\, I^{\ell}(\tau,\mu')\, d\mu'$$

$$- \frac{1}{4} F_0\, P^{\ell}(\mu,\mu_0) \exp(-\tau/\mu_0) \qquad (19)$$

Liou (1973) has shown the analytical solutions for Eq. (19) based upon the discrete ordinate method for radiative transfer are given by

$$I^{\ell}(\tau,\mu_i) = \sum_j L_j^{\ell}\, \phi_j^{\ell}(\mu_i) \exp(-k_j^{\ell}\tau) + z^{\ell}(\mu_i) \exp(-\tau/\mu_0)$$
$$\ell = 1, \ldots, N,$$
$$i = -n, \ldots, n. \qquad (20)$$

In Eq. (20) $\sum_j$ denotes j from -n to n ($n \neq 0$), and the eigenfunctions are derived from the associated homogeneous system as

$$\phi_j^{\ell}(\mu_i) = \frac{1}{1+\mu_i k_j^{\ell}} \sum_{m=0}^{M} \tilde{\omega}_m^{\ell}\, \xi_m(k_j^{\ell})\, p_m^{\ell}(\mu_i)\,, \qquad (21)$$

where M denotes the number of terms in the Legendre polynomial, p_m^{ℓ}, expansion, $\tilde{\omega}_m^{\ell}$ is a set of M + 1 constants, and ξ_m is a constant of proportionality and can be determined by

$$\xi_{m+1} = \frac{\partial m+1 - \tilde{\omega}_m^{\ell}}{k^{\ell}(m+1)}\, \xi_m - \frac{m}{m+1}\, \xi_{m-1}\,, \quad m = 0,1, \ldots, M-1\,. \qquad (22)$$

By taking $\xi_0 = 1$, all values of ξ can be evaluated. The eigenvalues, k^{ℓ}, may also be determined from

$$f(k^{\ell}) = 1 - \frac{1}{2}\sum_i a_i\, \phi_j^{\ell}(\mu_i) = 0\,. \qquad (23)$$

The last term in Eq. (20) represents a particular solution where

$$z^{\ell}(\mu_i) = \frac{1}{4}\,\mu_0\,F_0\,\frac{H^{\ell}(\mu_0)\,H^{\ell}(-\mu_0)}{\mu_0+\mu_i}\sum_{m=0}^{M}\tilde{\omega}_m^{\ell}\,\xi_m\left(\frac{1}{\mu_0}\right)\,p_m^{\ell}(\mu_i)\ , \qquad (24)$$

and the H function is given by

$$H^{\ell}(\mu) = \frac{1}{\mu_1\mu_2\cdots\mu_n}\prod_{i=1}^{n}(\mu+\mu_i)\left[\prod_{j=1}^{n}(1+k_j^{\ell}\mu)\right]^{-1}\ . \qquad (25)$$

The solution expressed in Eq. (20) is valid only for nonconservative scattering. For conservative scattering a slightly different form is needed but neglected here for simplicity.

The L_j in Eq. (20) are a set of N x 2n coefficients to be determinded from boundary and continuity equations in a non-homogeneous atmosphere. The atmosphere is inhomogeneous in that the single-scattering albedo and phase function are generally nonlinear functions of the optical depth. To account for this inhomogeneity, it is customary to divide the atmosphere into a number of layers such that each layer may be considered to be optically homogeneous.

The boundary conditions which describe the diffuse intensity for solar radiation at the top and bottom of the atmosphere are, respectively,

$$I^{1}(0,\mu_i) = 0 \qquad i = 1,2,\ldots,n\ , \qquad (26)$$

$$I^{N}(\tau^{N},+\mu_i) = \frac{r_g}{\pi}\left[F^{+}(\tau^{N}) + \mu_0\,\pi\,F_0\,\exp\left(-\tau^{N}/\mu_0\right)\right]\ ,$$

$$i = 1, 2, \ldots, n\ , \qquad (27)$$

where

$$F^{\downarrow}(\tau^N) = 2\pi \sum_{i=1}^{n} I^N(\tau^N, -\mu_i)\, a_i\, \mu_i \ , \qquad (28)$$

with a_i being the Gaussian quadrature weights and assuming an isotropic reflecting surface. These conditions state that there is no downward ($-\mu_i$) diffuse intensity at the top of the atmosphere, while at the bottom of the atmosphere, the upward ($+\mu_i$) diffuse intensity is the product of the surface albedo (r_g) and the total flux reaching the surface τ^N.

The continuity condition for atmospheric layers is

$$I^{\ell}(\tau^{\ell}, \mu_i) = I^{\ell+1}(\tau^{\ell}, \mu_i) \ , \quad i = -n, \ldots, n \ , \quad \ell = 1, \ldots N-1 \ . \qquad (29)$$

This condition requires no energy loss, in either the upward or downward radiation streams, at the interface separating each homogeneous layer. Note that τ^{ℓ} represents the optical depth from the top of the atmosphere to the bottom of the ℓ layer.

Substituting Eq. (20) into Eqs. (26) - (28) produces a set of equations for determining the L_j^{ℓ} constants. They are

$$\sum_j L_j^{\ell}\, \phi_j^{\ell}(-\mu_i) = - z^{\ell}(-\mu_i) \ , \quad i = 1,2, \ldots, n \ , \qquad (30)$$

$$\sum_j \left[L_j^{\ell}\, \gamma_j^{\ell}(\mu_i) + L_j^{\ell+1}\, \delta_j^{\ell+1}(\mu_i)\right] = - {}_{\ell}\eta^{\ell+1}(\mu_i) \ ,$$

$$i = -n, \ldots -1, 1, \ldots n \qquad \ell = 1,2, \ldots, N-1 \qquad (31)$$

$$\sum_j L_j^N \beta_j^N(\mu_i) = -\varepsilon^N(+\mu_i) \ , \qquad i = 1,2, \ldots , n \tag{32}$$

where

$$\gamma_j^\ell(\mu_i) = \phi_j^\ell(\mu_i) \exp\ (-k_j^\ell \tau^\ell) \ , \tag{33}$$

$$\delta_j^{\ell+1}(\mu_i) = -\phi_j^{\ell+1}(\mu_i) \exp\ (-k_j^{\ell+1} \tau^\ell) \ , \tag{34}$$

$$\beta_j^N(+\mu_i) = [\phi_j^N(+\mu_i) - 2\, r_g \sum_{j=1}^{N} \phi_j^N(-\mu_i)\, a_i\, \mu_i]$$

$$x \exp\ (-k_j^N \tau^N) \ , \tag{35}$$

$$^\ell\eta^{\ell+1} = [z^\ell(\mu_i) - z^{\ell+1}(\mu_i)] \exp\ (-\tau^\ell/\mu_0) \ , \tag{36}$$

$$\varepsilon^N(+\mu_i) = [z^N(+\mu_i) - 2\, r_g \sum_{i=1}^{N} z^N(-\mu_i)\, a_i\, \mu_i$$

$$- \frac{r_g}{\pi}\, \mu_0\, \pi\, F_0] \exp\ (-\tau^N/\mu_0). \tag{37}$$

Hence, there are N x 2 n equations for the determination of N x 2n unknown constants L_j^ℓ. In terms of matrix operations, this system of equations becomes

$$\vec{\Phi}\, \vec{L} = \vec{X} \ , \tag{38}$$

where

$$\vec{L} = \begin{bmatrix} L^1_{-n} \\ \vdots \\ L^1_n \\ \vdots \\ L^2_{-n} \\ \vdots \\ L^2_n \\ \vdots \\ L^N_{-n} \\ \vdots \\ L^N_n \end{bmatrix} \qquad (39)$$

$$\vec{X} = \begin{bmatrix} Z^1(-\mu_n) \\ \vdots \\ Z^1(-\mu_1) \\ {}^1\eta^2(-\mu_n) \\ \vdots \\ {}^1\eta^2(+\mu_n) \\ \vdots \\ \varepsilon^N(+\mu_1) \\ \vdots \\ \varepsilon^N(+\mu_0) \end{bmatrix} \qquad (40)$$

and

$$\vec{\Phi} = \begin{bmatrix} \phi^1_{-n}(-\mu_n) & \cdots & \phi^1_n(-\mu_n) & & & & & \\ \vdots & & \vdots & & & & & \\ \phi^1_{-n}(-\mu_1) & \cdots & \phi^1_n(-\mu_1) & & & & & \\ \gamma^1_{-n}(-\mu_n) & \cdots & \gamma^1_n(-\mu_n) & \delta^2_{-n}(-\mu_n) & \cdots & \delta^2_n(-\mu_n) & & \\ \vdots & & \vdots & \vdots & & \vdots & & \\ \gamma^1_{-n}(\mu_n) & \cdots & \gamma^1_n(\mu_n) & \delta^2_{-n}(\mu_n) & \cdots & \delta^2_n(\mu_n) & & \\ & & & \vdots & & \vdots & \vdots & \vdots \\ & & & & & & \beta^N_{-n}(\mu_1) & \cdots & \beta^N_n(\mu_1) \\ & & & & & & \vdots & & \vdots \\ & & & & & & \beta^N_{-n}(\mu_n) & \cdots & \beta^N_n(\mu_n) \end{bmatrix} \qquad (41)$$

where blank spaces denote zero elements. With this information, the coefficients, L_j^{ℓ}, may be determined simultaneously by employing any matrix inversion method. Substituting the L_j^{ℓ} back into Eq. (20) produces the intensity field within each layer.

The modified radiative transfer program now allows 21 levels and 20 layers in the atmospheric model. It can use any of the five climatological atmospheric profiles compiled by McClatchey et al. (1972). After the optical depths are calculated for each sub-band at each of the 21 levels, solutions defined by Eq. (20) are computed for each level in the atmosphere and for each of the four discrete streams of radiation. There is a separate set of solutions for each sub-band; consequently, the L's shown in Eq. (20) must be determined 42 times, 24 times for water vapor and 18 times for ozone. Each of these 42 sets of L's are found by inverting a 80x80 matrix. After computing the L's, the upward and downward intensities of the radiation stream at a given level can then be calculated.

3.3.2 Fluxes and Heating Rates

Once the intensities have been determined for each layer, the sub-band upward and downward fluxes are computed for each layer (see Figure 6). The fluxes are given by

$$F^{\uparrow}(\tau) = 2\pi \sum_{i=1}^{n} a_i \mu_i I(\tau,\mu_i) , \qquad (42)$$

for upward fluxes, and

$$F^{\downarrow}(\tau) = - 2\pi \sum_{i=1}^{n} a_i \mu_i I(\tau,-\mu_i) - S(\tau,\mu_0) , \qquad (43)$$

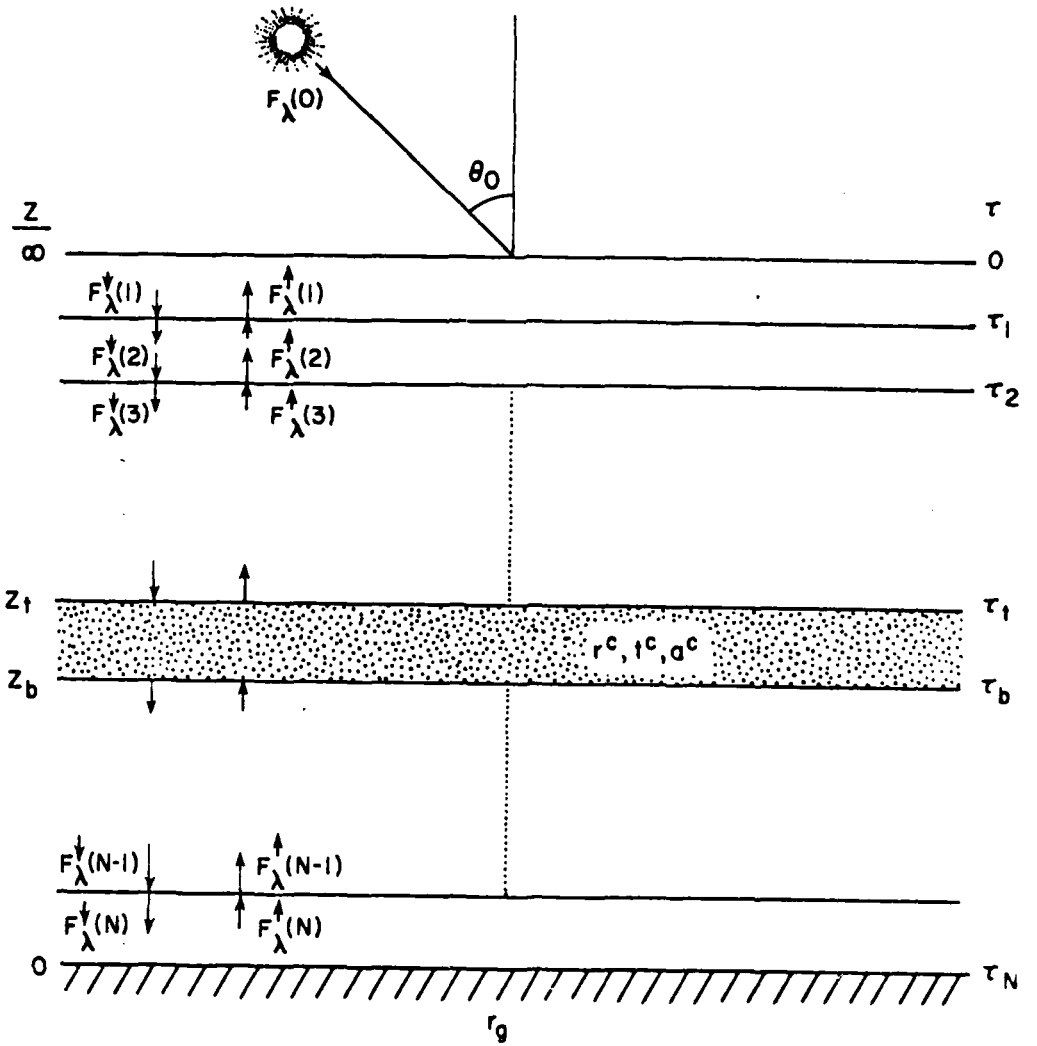

Fig. 6. Configuration of solar radiation flux transfer in cloudy atmospheres.

for downward fluxes, where $S(\tau,\mu_0)$ is the direct solar flux arriving at optical depth τ/μ_0 and is given by

$$S(\tau,\mu_0) = \mu_0 F_0 \exp(-\tau/\mu_0) . \quad (44)$$

The net flux for a given layer may be computed from

$$F(\tau) = F^{\uparrow}(\tau) + F^{\downarrow}(\tau) , \quad (45)$$

and the sub-band heating rate for a layer of air resulting from the absorption by atmospheric gases and cloud particles for any given band can be calculated from

$$\left(\frac{\partial T}{\partial t}\right) = -\frac{1}{C_p \bar{\rho}_a}\left(\frac{\partial F}{\partial z}\right) = -\frac{1}{C_p \bar{\rho}_a}\frac{F(z_{\ell+1}) - F(z_\ell)}{\Delta z} , \quad (46)$$

where $\bar{\rho}_a$ is the mean density of air in layer ℓ and C_p is the specific heat of air for constant pressure. The sub-band heating rates are summed together and weighted according to the solar flux in each sub-band to produce the total heating rate for a layer.

3.3.3 Cloud Optical Properties

Clouds regularly occupy about 50% of the sky on a global scale and are the single most important regulators of the earth's radiation balance. They absorb and scatter incoming solar radiation at all wavelengths. However, introduction of clouds into an atmospheric profile vastly complicates the radiative calculations because the scattering source function in the transfer equation involves Mie scatter which is a complex function of cloud microphysics.

To obtain the reflection, absorption, and transmission of the cloud for the entire solar spectrum, proper summation over the fluxes in each spectral region is required.

Consider a cloudy atmosphere containing one cloud layer with top and base heights denoted as z_t and z_b as shown in Figure 6 and assume the upward and downward fluxes are known at each level. The cloud reflection is defined as the ratio of the reflected flux density to the incident solar flux density normal to the cloud top. Thus

$$r_c = \sum_i f_i \, F^{\uparrow}(z_t) \; / \; \sum_i f_i \, F^{\downarrow}(z_t) \tag{47}$$

where f_i denotes the fractional solar flux in the i^{th} spectral band. The cloud transmission, t_c, is defined as the ratio of the downward flux density at the cloud base to the incident solar flux normal to the cloud top and is given by

$$t_c = \sum_i f_i \, F^{\downarrow}(z_b) \; / \; \sum_i f_i \, F^{\downarrow}(z_t) \; . \tag{48}$$

Finally, the cloud absorption, α_c, is defined as the ratio of the net flux density divergence of the cloud layer to the incident solar flux normal to the cloud top. Thus,

$$\alpha_c = \frac{\sum_i f_i \, [F^{\downarrow}(z_t) - F^{\downarrow}(z_b)]}{\sum_i f_i \, F^{\downarrow}(z_t)} \; . \tag{49}$$

Heating rates for cloud layers are computed as previously described for clear layers, once the upward and downward fluxes are known at the cloud top and cloud base.

It should be noted that these cloud radiative properties definitions are not the same as those previously defined by Liou (1976) and Liou and Wittman (1979) which defined broadband cloud radiative properties using inaccurate summations over wavelength.

3.3.4. The Four Stream Solution

For discrete streams of 16, (n = 8), the discrete ordinate method (DOM) produces results which are generally accurate up to 3-4 digits when compared to doubling computations which have an accuracy of about five decimal points according to van de Hulst and Grossman (1968). The discrete ordinate method has been found to be quite satisfactory because it allows the solutions to Eq. (20) to be explicitly derived and can easily take into account various distribution, thickness, and cloud types making the scheme well suited to studying climatic effects of the clouds.

Liou (1973) found the accuracy of results produced by the four stream (n = 2) discrete ordinate method to be within about 1% of those generated by 16 streams for flux calculations; thus, the four stream DOM model developed by Freeman and Liou (1979) was considered a more exact solution for comparing with the parameterized model. However, since the previous solar transfer program developed at the University of Utah had a different emphasis than the present study, several modifications were necessary before it could be properly used for comparison purposes. These modifications include:

(1) In Freeman and Liou's (1979) work the objective of the research was not centered upon ozone heating rates. Consequently, the radiation model extended up to only 30 km and contained just two absorption

coefficients for ozone; one in the Hartley-Huggins band complex, another for the Chappius band complex. This model was modified to allow 12 absorption coefficients in the former and six in the latter ozone band complexes while the height was extended to 60 km. The ozone absorption wavelength interval, mean absorption coefficient, and fractional solar flux in each of these 18 bands are listed in Table 5. The mean ozone absorption coefficient in each wavelength interval in Table 5 was calculated by weighting the mean absorption coefficient in each 0.05 μm sub-interval with the fractional solar flux in the sub-interval, then dividing by the total solar flux in the interval. Note that Table 4 only depicts the monochromatic absorption coefficient at the wavelengths shown.

(2) The previous solar radiation program developed at the University of Utah only computes heating rates in a clear atmosphere or an atmosphere containing one cloud. Considerable programming was required to allow multiple cloud layers to be introduced into the model atmosphere. The present program will now allow up to four cloud layers in an atmosphere.

(3) The six water vapor bands were each subdivided into five sub-bands in which the absorption coefficient was assumed constant. Thus, the optical depth was calculated for each wavelength interval at each level in the atmosphere using Eq. (17). However, water vapor absorption coefficients in an earlier version of the solar radiation program were recomputed. This [illegible] because wavelength intervals larger than those derived by Liou and Sasamori (1975) were used in the present program which was intended to allow absorption and scattering processes to be considered in the transfer calculation. For

Table 5. Ozone Wavelength Interval with Associated Mean Absorption Coefficient and Fractional Solar Flux

Wavelength Interval (μm)	Absorption Coefficient (cm^{-1})	Fractional Solar Flux
.20-.21	9.8	1.24×10^{-4}
.21-.22	27	2.97×10^{-4}
.22-.23	75	4.599×10^{-4}
.23-.24	164	4.59×10^{-4}
.24-.25	254	5.14×10^{-4}
.25-.26	290	7.55×10^{-4}
.26-.27	241	1.35×10^{-3}
.27-.28	145	1.59×10^{-3}
.28-.30	33.7	6.46×10^{-3}
.30-.32	2.8	1.01×10^{-2}
.32-.34	.16	1.50×10^{-2}
.34-.35	.014	7.95×10^{-3}
.45-.50	.011	7.46×10^{-2}
.50-.55	.055	6.78×10^{-2}
.55-.60	.11	6.30×10^{-2}
.60-.65	.09	5.87×10^{-2}
.65-.70	.038	5.33×10^{-2}
.70-.80	.015	9.14×10^{-2}

comparisons between results computed from parameterization and more exact transfer programs we have derived a new set of equivalent absorption coefficients, k_m, and weighting factors, w_m, for each sub-band in the six water vapor bands and the larger band frequency interval which appear in Table 6.

(4) Finally, the definition of cloud absorptivity, reflectivity, and transmissivity used by Liou and Wittman (1979) was modified to coincide more accurately with the broadband parameterization approach. The broadband definitions for cloud radiative properties are given in Eqs. (47) - (49).

Table 6. Equivalent Absorption Coefficient k_m and the Weighting Factor w_m Derived from the Exponential Fit Based on Successive Reduction Method.

Band (μm)	$\Delta\nu$ (cm^{-1})	k_m				w_m			
		1	2	3	4	1	2	3	4
0.94	2500	.00016	.02027	.17363	1.18313	.8660	.09446	.03803	.00156
1.1	1667	.00044	.01968	.15033	.99010	.75361	.19280	.05284	.00075
1.38	2083	.00090	.02250	.23590	1.92500	.46576	.24018	.19843	.09587
1.87	1705	.00033	.02178	.23816	2.08330	.65050	.15353	.12594	.07000
2.7	1212	.00279	.06799	.73472	7.90850	.41760	.22207	.19719	.16317
3.2	701	.00374	.03140	.19420	1.13377	.49492	.31451	.16985	.01082

Section 4

THE BROADBAND PARAMETERIZATION APPROACH IN A CLEAR ATMOSPHERE

4.1 General

In the previous section, the four stream DOM solution for the RTE was described. This type of solution is quite time consuming and expensive since heating rates must be computed for each wavelength interval then integrated across the frequency spectrum to produce the total heating rate for a layer. The broadband approach simplifies this procedure by integrating the absorption coefficient over wavelength, producing an absorptivity which is wavelength independent, so the RTE need only be solved once.

4.2 Gaseous Absorption in Clear Skies

In clear skies, atmospheric heating results basically from gaseous absorption, thus the radiative transfer equation simplifies to

$$\mu_0 \frac{dI_\lambda(u)}{k_\lambda du} = - I_\lambda \ , \tag{50}$$

where du is the path length of the absorbing gas. The solution to this equation, known as Beer's Law, is

$$I_\lambda^{\downarrow}(u) = I_\lambda(0) \exp \left\{ - \int_0^u k_\lambda \, du \, / \, \mu_0 \right\} \ , \tag{51}$$

which, after integrating over solid angles gives

$$F_\lambda^{\downarrow}(u) = F_\lambda(0) \exp\left[-\int_0^u k_\lambda \, du / \mu_0\right] . \tag{52}$$

where $I_\lambda(0)$ and $F_\lambda(0)$ denote the monochromatic intensity and flux density, respectively, at $u = 0$.

The downward flux density along the solar beam is found by integrating the monochromatic flux density across wavelength such that

$$F^{\downarrow}(u) = \int_0^\infty F_\lambda^{\downarrow}(u) \, d\lambda = \int_0^\infty F_\lambda^{\downarrow}(0) \exp\left[-\int_0^u k_\lambda \, du / \mu_0\right] d\lambda . \tag{53}$$

The monochromatic absorptivity in a non-scattering medium is defined by

$$A_\lambda(u) = 1 - \exp\left[-\int_0^u k_\lambda \, du\right] . \tag{54}$$

Thus, Eq. (53) becomes

$$F^{\downarrow}(u) = \int_0^\infty F_\lambda^{\downarrow}(0) \, [1 - A_\lambda(u/\mu_0)] \, d\lambda . \tag{55}$$

Defining the solar constant such that

$$S_0 = \int_0^\infty F_\lambda^{\downarrow}(0) \, d\lambda , \tag{56}$$

then the downward flux density perpendicular to the layer of stratification is given by

$$F^{\downarrow}(u) = \mu_0 \, S_0 \, [1 - A(u/\mu_0)] \tag{57}$$

The heating rate at level z(u) is given by

$$\frac{\partial T}{\partial t} = - \frac{1}{C_p \rho_a} \frac{\partial F^{\downarrow}}{\partial z} = - \frac{\rho}{C_p \rho_a} \frac{\partial F^{\downarrow}}{\partial u} \quad , \tag{58}$$

where ρ_a is the air density at level z, ρ and u apply to the absorbing gas.

Thus, the broadband concept requires a gaseous absorptivity which is wavelength independent and applies to the entire solar spectrum. This may be achieved by noting that

$$A(u_j/\mu_0) = \sum_i f_i \, A_i(u_j/\mu_0) \quad , \tag{59}$$

where f_i is the fractional solar flux for the i^{th} wavelength interval and A_i is the monochromatic gaseous absorptivity given in Section 2 for each gas type. Subscript j denotes the type of absorbing gas where 1, 2, and 3 refer to water vapor, carbon dioxide, and ozone, respectively.

4.2.1 Ozone Absorption and Heating Rate Profiles

The broadband ozone absorptivity is given by Eq. (59) where i = 1, . . . , 18 and the total ozone absorptivity is given by

$$A(u_3/\mu_0) = \sum_{i=1}^{18} [1 - \exp (-\bar{k}_i u_3/\mu_0)] \quad , \tag{60}$$

where $\bar{k}_i$ is the mean absorptivity and f_i is the fractional flux in the i^{th} spectral interval as given in Table 6.

In Fig. 7, the ozone broadband absorptivity computed by Eq. (59) for path lengths of 0.0001 to 10 cm-NTP are compared with other published data. The broadband absorptivity compares very favorably with

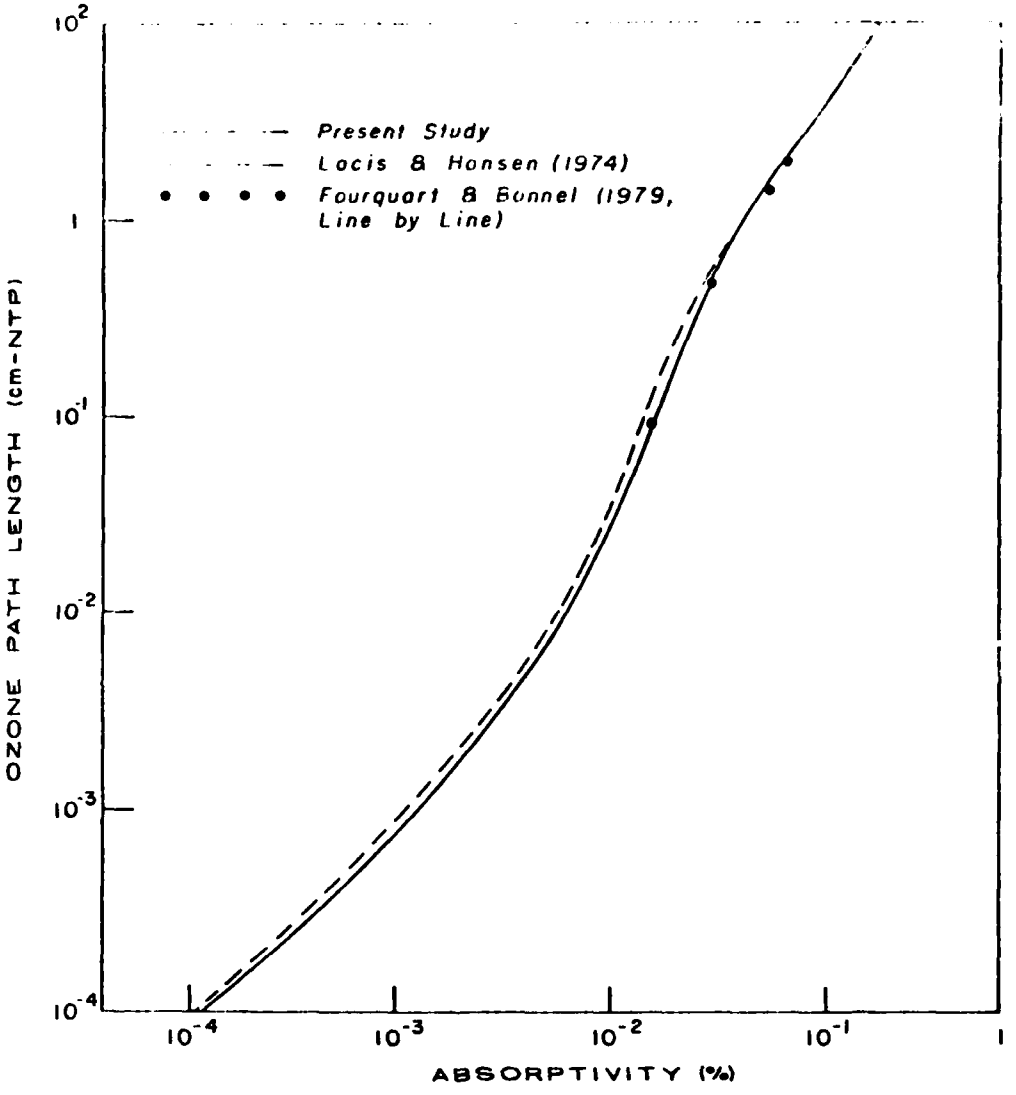

Fig. 7 Ozone broadband absorptivity compared to other published data.

the line-by-line calculations taken from Fouquart and Bonnel (1980) and also is in good agreement with that of Lacis and Hansen (1974), although slightly larger at very small path lengths.

The ozone heating rate may be determined in using Eq. (58). The rate of change of downward solar flux is readily calculated by substituting Eq. (55) into Eq. (58). This gives

$$\frac{\partial F^{\downarrow}}{\partial u_3} = - S_0 \sum_{i=1}^{18} f_i \, \bar{k}_i \exp (-\bar{k}_i u_3/\mu_0) \, . \tag{61}$$

The importance of Rayleigh scattering and the surface albedo on the solar energy absorbed by ozone has been shown by Dave and Furukawa (1967). Since the ozone heating rate virtually approaches zero at about 10 km, ozone was modeled as an absorbing layer overlaying a scattering layer. In a clear atmosphere, Lacis and Hansen (1974) have derived a parameterized equation for Rayleigh scattering albedo at the top of this scattering layer, given by

$$r_a(\mu_0) = 0.28 \; / \; (1 + 6.43 \; \mu_0) \, . \tag{62}$$

Using this expression, the total reflection at the top of this scattering layer, $r(\mu_0)$, including the surface albedo, may be determined by a ray tracing geometric method. As shown in Fig. 8, the total reflection at the top of the Rayleigh scattering layer is given by an infinite series as follows:

$$r(\mu_0) = r_a + t_a(\mu_0) \, r_g \, \bar{t}_a + t_a(\mu_0) \, r_g^2 \, \bar{r}_a \, \bar{t}_a + t_a(\mu_0) \, r_g^3 \, \bar{r}_a \, \bar{t}_a$$

$$+ t_a(\mu_0) \, r_g^4 \, \bar{r}_a^3 \, \bar{t}_a + \ldots$$

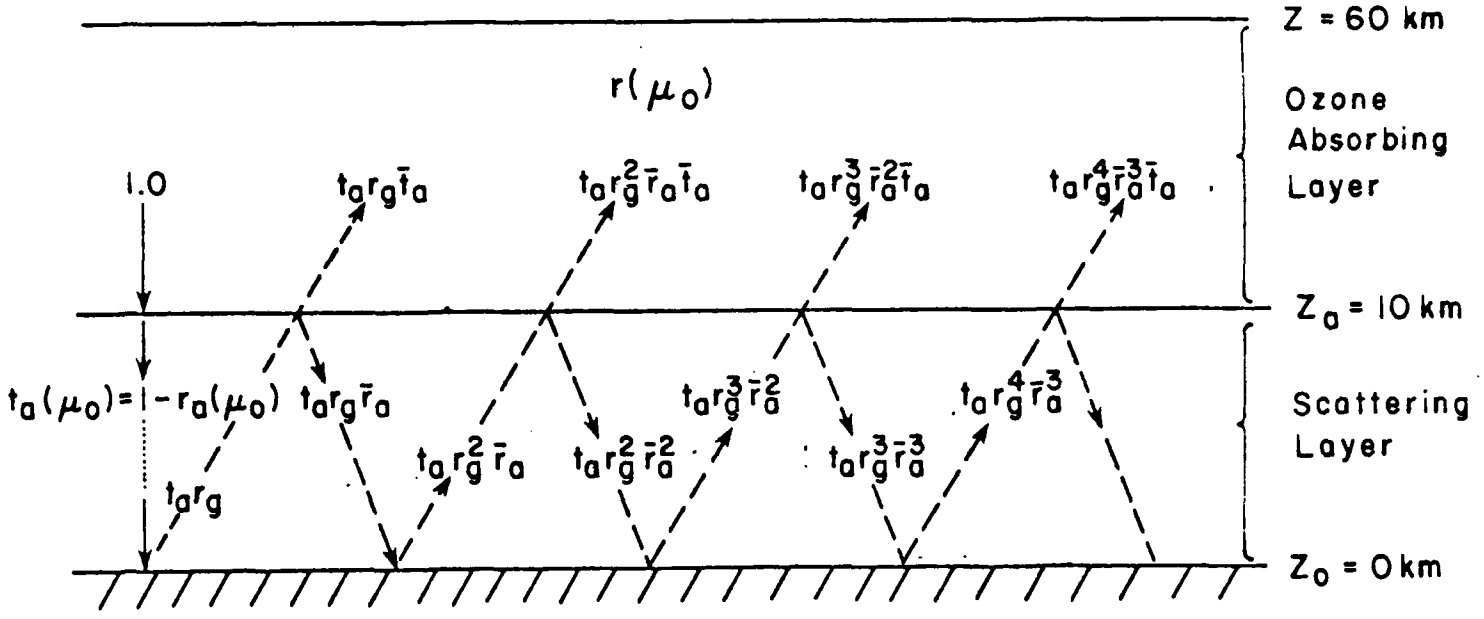

Fig. 8 Total reflection at the top of the ozone scattering layer by a ray tracing method.

$$= r_a(\mu_0) + [1 - \bar{r}_a(\mu_0)]\, r_g\, (1 - \bar{r}_a)\, [1 - r_g\, \bar{r}_a + r_g^2\, \bar{r}_a^2 + \ldots]$$

$$= r_a(\mu_0) + [1 - \bar{r}_a(\mu_0)\,]\, (1 - \bar{r}_a)\, r_g\, /\, (1 - r_g\, \bar{r}_a)\,, \qquad (63)$$

where r_g is the reflectivity of a Lambert reflecting surface and

$$\bar{t}_a = 1 - \bar{r}_a\,, \quad t_a(\mu_0) = 1 - r_a(\mu_0)\,. \qquad (64)$$

The spherical albedo of a Rayleigh scattering atmosphere, $\bar{r}_a$, is defined by

$$\bar{r}_a = 2 \int_0^1 r_a(\mu_0)\, \mu_0\, d\mu_0\,. \qquad (65)$$

The numerical value of $\bar{r}_a$ was determined to be 0.0685.

Now, the rate of change of diffuse upward flux at any $z > z_a$ may be readily calculated by replacing the zenith angle dependent argument of the broadband absorptivity, (u_3/μ_0), with the diffuse path length, $(1.66\ u_3)$, as described by Goody (1964). Thus

$$\frac{\partial F^{\uparrow}}{\partial u_3} = \frac{\partial}{\partial u_3} \{F^{\uparrow}(z_a)\, [1 - A\ (1.66\ u_3]\}$$

$$= -\ 1.66\ F\ (z_a) \sum_{i=1}^{18} f_i\, \bar{k}_i\, \exp\,(-1.66\, \bar{k}_i\, u_3)\,, \qquad (66)$$

where the upward flux at $z = z_a$ is given by

$$F^{\uparrow}(z_a) = S_0\, \mu_0\, [1 - A(u/\mu_0)]\, r(\mu_0)\,, \qquad (67)$$

and $A(u/\mu_0)$ is the total gaseous broadband absorptivity of water vapor, carbon dioxide and ozone in the column from the top of the atmosphere to z_a.

The instantaneous ozone heating rate at any height above the top of the ozone scattering layer is given by

$$\left(\frac{\partial T}{\partial t}\right)_a = -\frac{g}{c_p p_a}\left(\frac{\partial F^{\downarrow}}{\partial u} + \frac{\partial F^{\uparrow}}{\partial u}\right) = \frac{\mu_3}{c_p p_a}\left\{S_0 \sum_{i=1}^{18} f_i \bar{T}_i e^{-\quad} \quad 1.66\, F^{\uparrow}(z_a) \sum_{i=1}^{18} f_i \bar{k}_i \exp\left(-1.66\, \bar{k}_i u_{\quad}\right)\right\} \tag{68}$$

Ozone heating rates were calculated for a clear midlatitude winter atmospheric profile (McClatchy et al., 1972) and solar zenith angles of 0.2, 0.5, and 1.0. Figure 9 shows the results obtained from the parameterization model in the dashed curve and those obtained from the DOM in the solid line for a surface albedo of zero. The two methods produce results which are almost indistinguishable except at about 40 km where the parameterization was about 1° C/24 hour day larger than the more exact method. This figure illustrates an interesting aspect of ozone heating rates. Even though the maximum ozone concentration is located at about 20-25 km, the maximum heating rate occurs at about 45-55 km, depending on the solar zenith angle. As Lacis and Hansen (1974) have explained, this is caused by the strong absorption of energy in the ultraviolet region of the solar spectrum by the Hartley-Huggins band complex at altitudes where the air density is very small.

Results in Fig. 10 were obtained under similar circumstances to those of Fig. 9, except the surface albedo was increased to 100%. The sets of curves are again in remarkably good agreement. It should be noted, however, that the increased surface albedo had its maximum effect in the 10-35 km range where the diffuse upward radiation contacted the maximum ozone concentration in the atmosphere. The area of

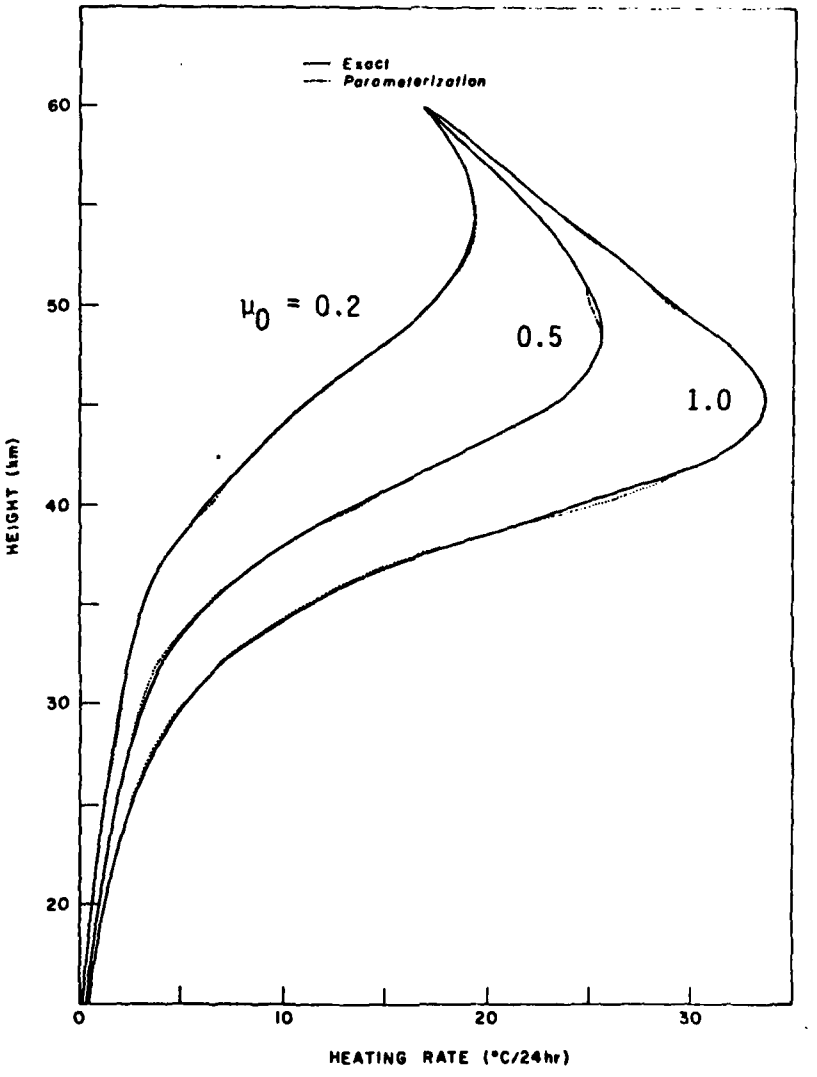

Fig. 9 Ozone heating rates in a clear midlatitude winter profile with a surface albedo of 0.

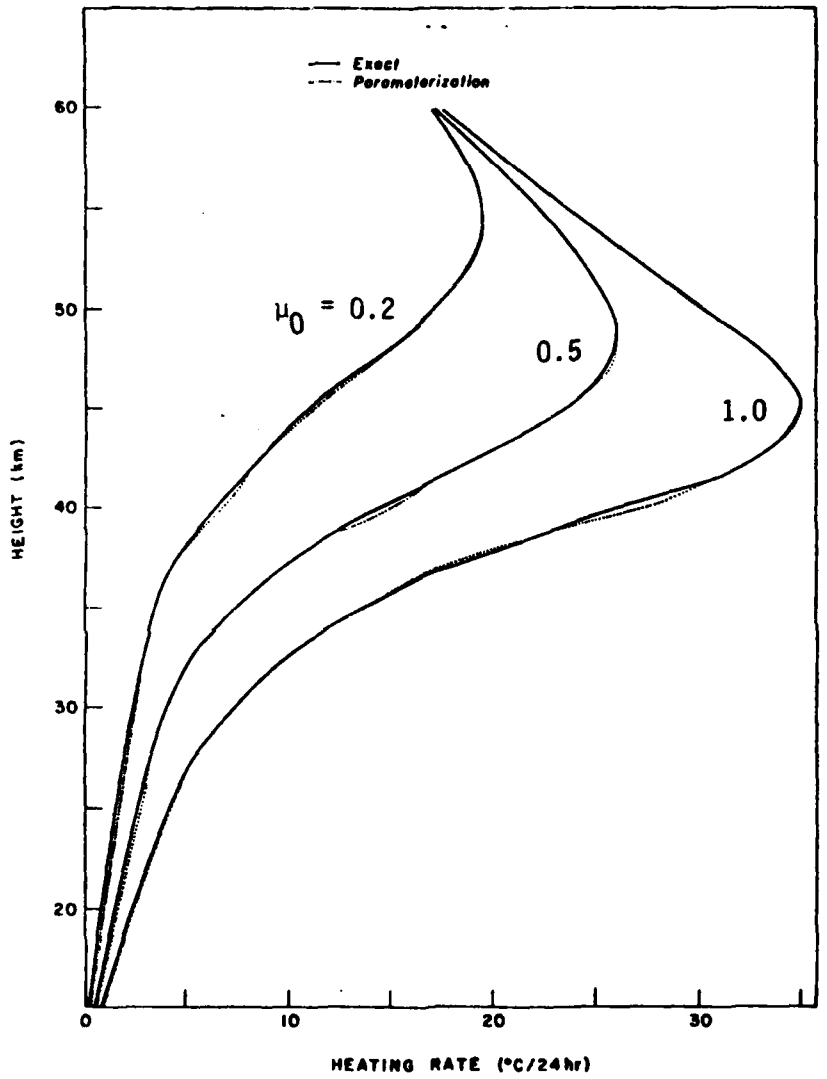

Fig. 10 Ozone heating rates in a clear midlatitude winter profile with a surface albedo of 1.

maximum ozone heating increases only slightly by increasing the surface albedo from zero to 100% because the Hartley-Huggins bands were nearly saturated by the absorption of the direct solar flux.

4.2.2 Water Vapor Absorptivity and Heating Rate Profiles

The water vapor broadband absorptivity is also described by Eq. (59). Table 7 lists the wavelength interval over which Howard et al. (1956) originally measured the total absorptivity of each water vapor band. Also listed are the solar flux in each interval after Thekaekara (1974) and the computed fractional solar flux.

In Fig. 11, the broadband absorptivity for water vapor path lengths of 0.01 to 10 g cm^{-2}, computed at STP by Eq. (59), are compared with other published data. Two important points are present in this figure. First, the broadband absorptivity curve is closest to the line-by-line calculations taken from Fouquart and Bonnel (1980), in both the small and large water vapor path lengths. Secondly, the slopes of the broadband and line-by-line absorptivity curves are nearly parallel. Since the heating rate is directly proportional to the slope of the absorptivity curve, the heating rate curves produced by the broadband water vapor absorptivity should be quite accurate.

The rate of decrease in downward flux due to water vapor absorptivity may be obtained by substituting Eq. (5) into Eq. (55) and after differentiating with respect to water vapor path length u_1, we obtain

$$\frac{\partial F^{\downarrow}}{\partial u_1} = -S_0 \mu_0 \log_{10} e \sum_{i=1}^{6} \frac{D_i f_i}{\Delta\nu_i} \left[\frac{\frac{1}{\mu_0} \bar{p}^{\varepsilon_i} + \varepsilon_i \frac{u_1}{\mu_0} \bar{p}^{\varepsilon_i - 1} \frac{d\bar{p}}{du_1}}{\frac{u_1}{\mu_0} \bar{p}^{\varepsilon_i} + \gamma_{0i}} \right] \tag{69}$$

Table 7 Fractional Solar Flux in H_2O Bands

H_2O band	Interval (μm)	Solar Flux ($W\ m^{-2}$)	Fractional Flux
0.94	0.8700-0.9900	102.810	0.0760
1.1	1.0753-1.2048	71.488	0.0528
1.38	1.2500-1.5385	99.034	0.0732
1.87	1.6949-2.0833	52.256	0.0388
2.70	2.3041-2.9940	32.733	0.0242
3.20	2.9940-3.5714	11.921	0.0088

where $\epsilon_i = K_i/D_i$. Moreover, from Eq. (8) we find

$$\frac{d\bar{P}}{du_1} = -\frac{1}{u_1^2}\int_0^{u_1} P(u)\,du + \frac{P}{u_1} = \frac{P-\bar{P}}{u_1} \quad . \tag{70}$$

Thus, we write

$$\frac{\partial F^{\downarrow}}{\partial u_1} = -S_0 \sum_{i=1}^{6} Y_i(u_1/\mu_0) \quad , \tag{71}$$

where

$$Y_i(u_1/\mu_0) = \log_{10} e\, \frac{D_i f_i \bar{P}^{\,i}}{\Delta\nu_i} \left[\frac{1 - \epsilon_i + \epsilon_i\, P/\bar{P}}{u_1\, \bar{P}^{\epsilon_i}/\mu_0 + \chi_{0i}}\right] \quad . \tag{72}$$

The rate of change of diffuse upward flux due to water vapor absorption is determined exactly as it was for ozone in Eq. (66) with the

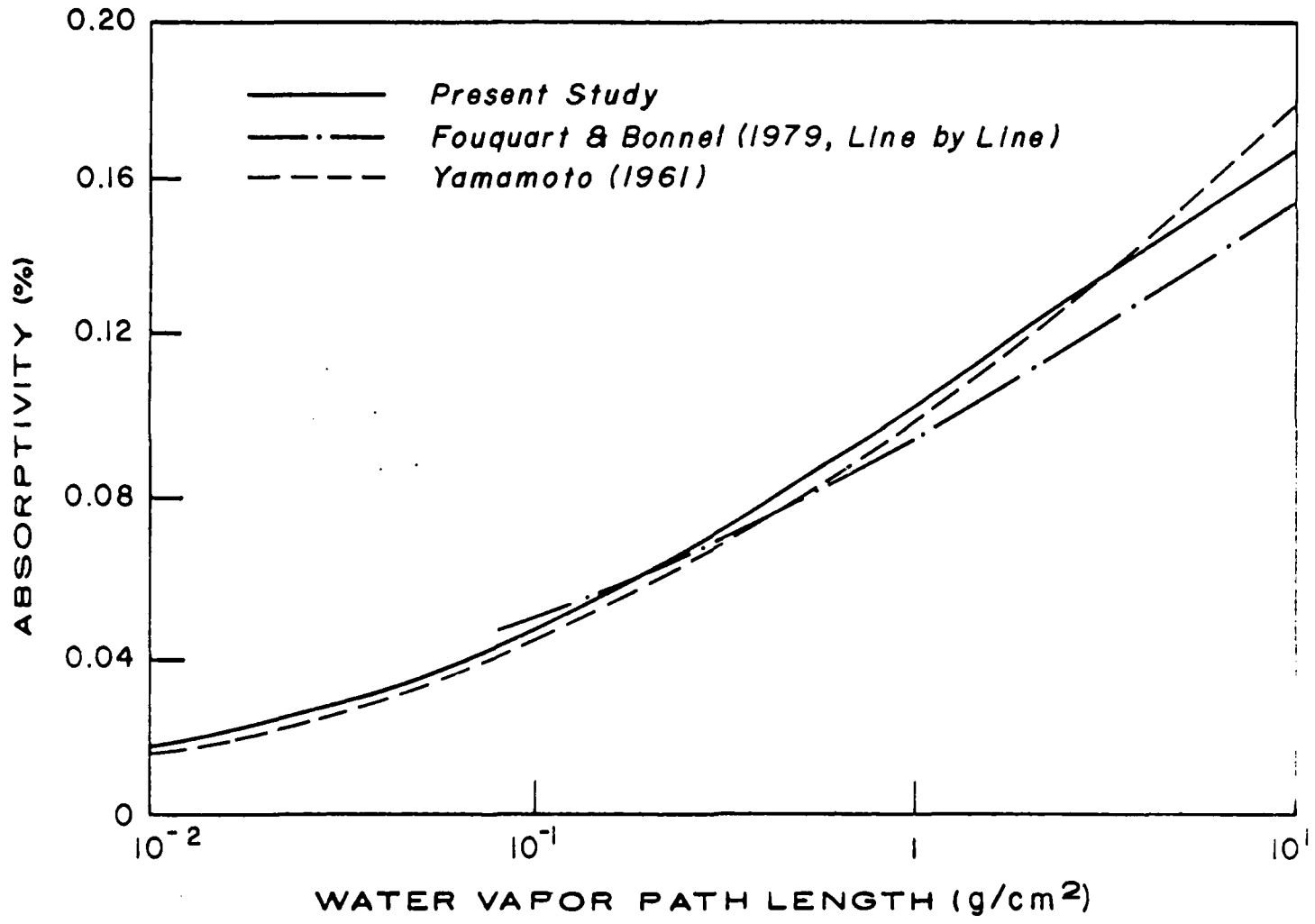

Fig. 11 Broadband water vapor absorptivity compared against other published data, at STP.

exception that $F^{\uparrow}(z_a)$ is replaced by $F^{\uparrow}(z_0)$ with $z_0 = 0$. It must also be recognized that the limits of integration have been reversed in the reduced pressure expression. The total heating rate at level $z(u_1)$, due to water vapor absorption of direct and diffuse solar radiation is then given by

$$\left(\frac{\partial T}{\partial t}\right)_1 = \frac{\rho_1}{C_p \rho_a} \left[S_0 \sum_{i=1}^{6} Y_i(u_1/\mu_0) + 1.66\, F^{\uparrow}(z_0) \sum_{i=1}^{6} Y_i\,(1.66\, u_1)\right] . \tag{73}$$

Figure 12 depicts the exact and parameterized water vapor heating rate using a midlatitude winter profile (McClatchey et al., 1972) for a clear sky, a surface albedo of zero, and solar zenith angles of 0.2, 0.5, and 1.0 for the incident solar beam. Setting the surface albedo to zero produced heating rates which were due only to the absorption of direct solar flux. In general, the parameterization and the exact curves agree within about 0.1° C in the lower troposphere per 24 hrs of heating. Above about 9 km, the disagreement increases to a maximum of 0.25° C per 24 hrs with the sun directly overhead for the entire time period.

In Fig. 13, the surface albedo was set to 100% to maximize the effect of absorption of the diffuse radiation component in the same atmospheric profile. A comparison of this curve with the preceding one reveals the effect of the diffuse component was confined to the lowest 6 km of the troposphere and increased toward the ground where the water vapor concentration was a maximum. Also, the magnitude of the heating rate caused by absorption of diffuse radiation was considerable, approximately tripling at the surface but becoming less than 0.1° C

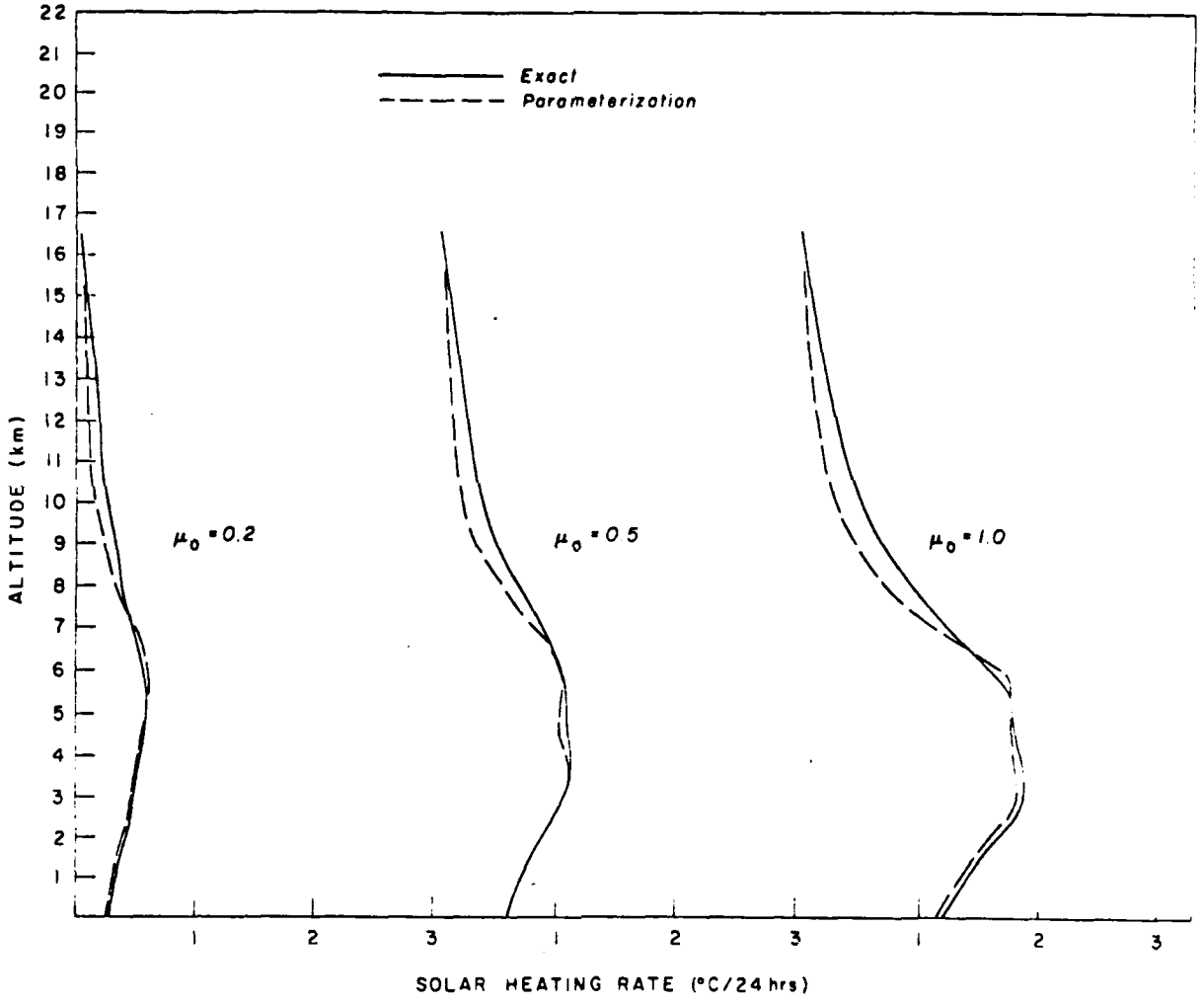

Fig. 12 Water vapor heating rates for a clear midlatitude winter profile. The surface albedo r_g is set to be zero.

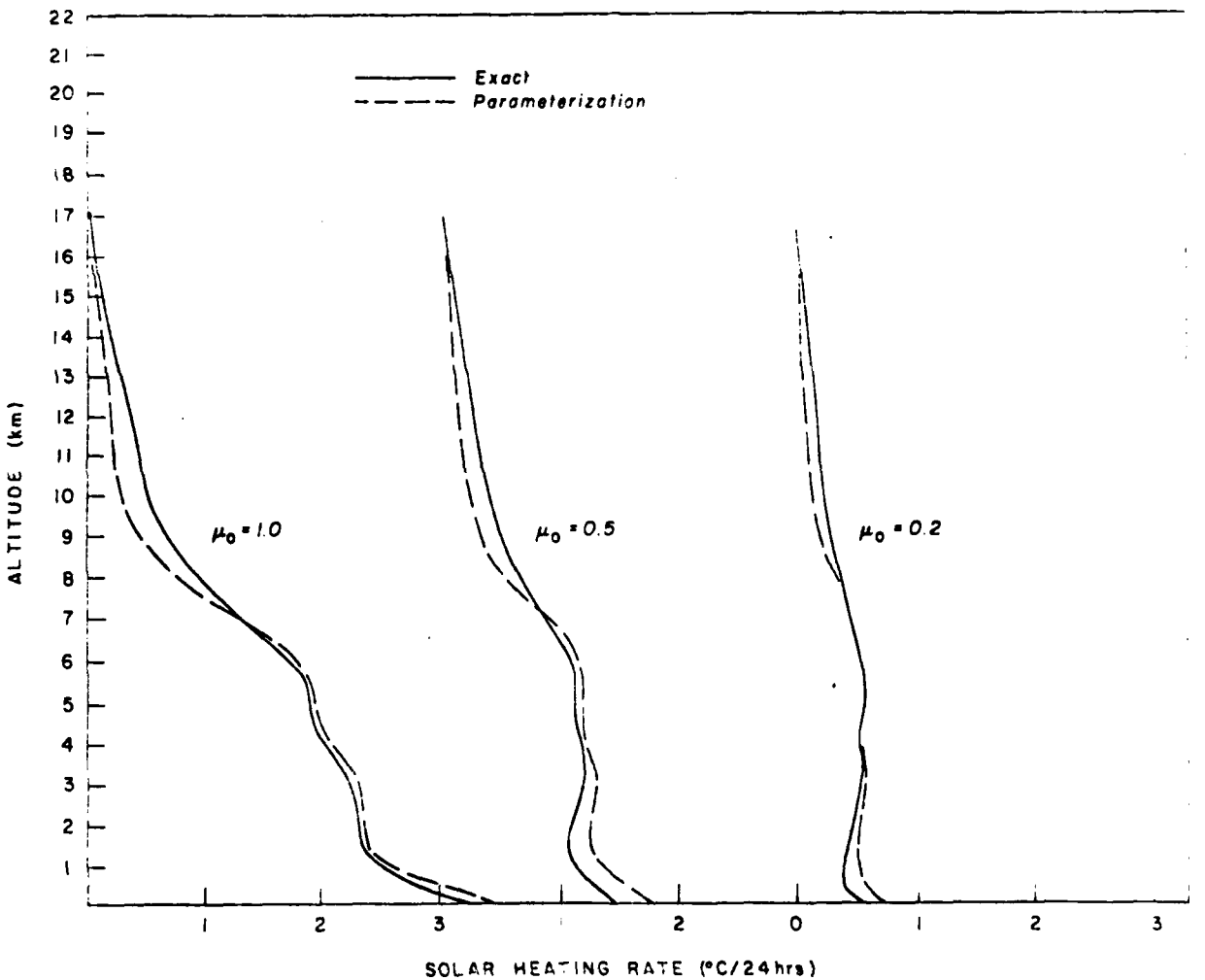

Fig. 13 Water vapor heating rates for a clear midlatitude winter profile. The surface albedo is set to be 1.

at 6 km. The error introduced by using the diffusivity factor to represent the scattering over all zenith angles is highlighted by the parameterized heating rates becoming larger than those produced by the exact method in the lower troposphere when the surface albedo was increased to 100%. In Fig. 12, the parameterized method produced smaller heating rates throughout the same region.

Figure 14 compares the same methods for a clear atmosphere using the midlatitude summer profile compiled by McClatchey et al. (1972) with a surface albedo of 15%. This albedo is an average albedo for the earth, consequently this figure shows the magnitude of heating rate errors which will typically occur using the parameterization method.

4.2.3 Carbon Dioxide Absorption and Heating Rate Profiles

Since the spectral interval in which CO_2 absorbs solar radiation in the 2.7 μm band is completely contained in the water vapor band, the broadband water vapor absorptivity can easily be modified to include its effects. As previously pointed out, the contribution of carbon dioxide to the total atmospheric absorptivity in the 2.7 μm area of the electromagnetic spectrum increases as the total water vapor absorptivity decreases in this area. This idea is represented by

$$A(H_2O + CO_2) = \int_\nu A_\nu(H_2O)\, d\nu + \delta \int_\nu A_\nu(CO_2)\, d\nu \,, \quad \nu = 2.7\ \mu m \tag{74}$$

where δ takes a value between 0 and 1 as depicted in Fig. 4.

Using the concept shown in Eq. (59), the combined water vapor and carbon dioxide broadband absorptivity is then

$$A(u_{12}/\mu_0) = \sum_{i=1}^{6} f_i^h\, A_i(u_1/\mu_0) + \delta\, f_5^c\, A_5^c\, (u_2/\mu_0) \tag{75}$$

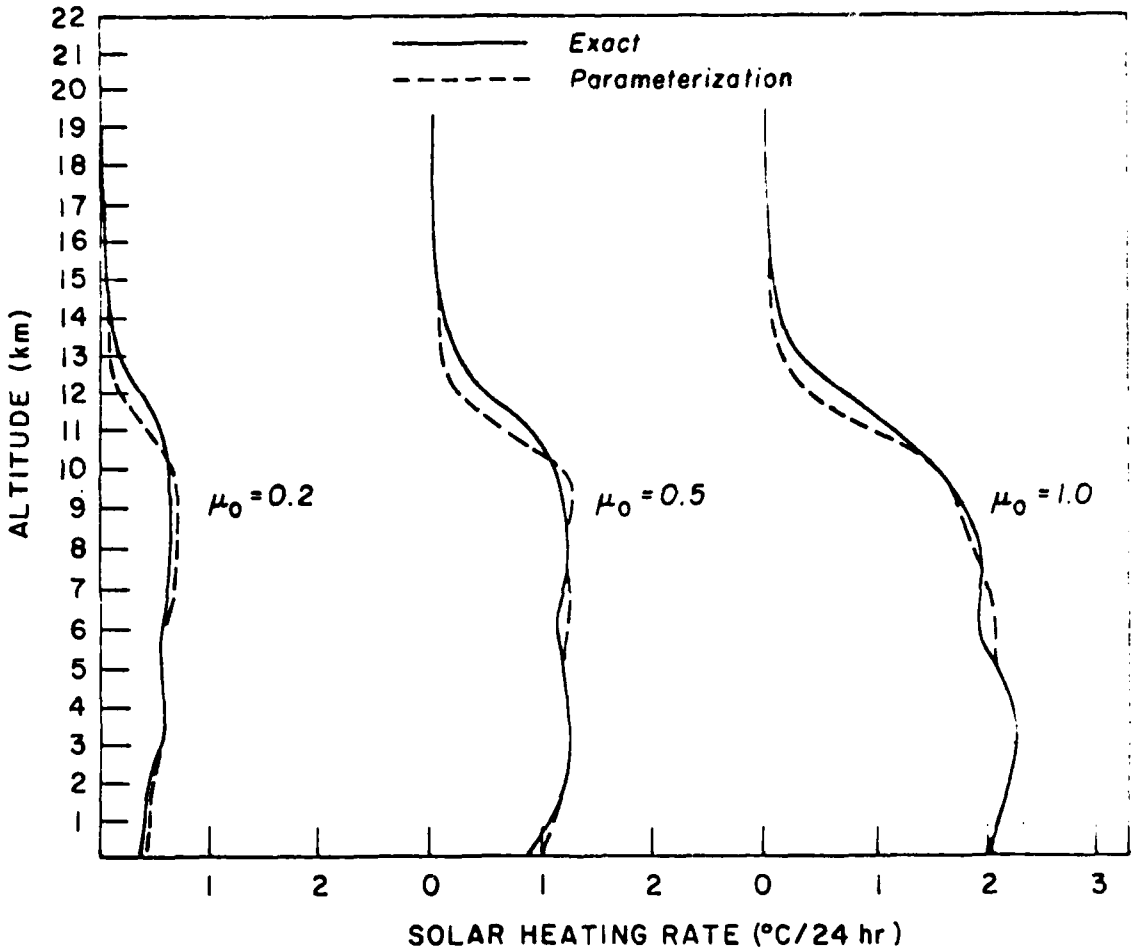

Fig. 14 Water vapor heating rates for a clear midlatitude summer profile. The surface albedo is 0.15.

where f^c is the fractional solar flux in the carbon dioxide 3480-3800 cm^{-1} frequency interval with a value of 0.0073, and subscript 5 refers to the 2.7 μm band.

Atmospheric heating caused by absorption of solar flux by carbon dioxide may be calculated similarly to that of water vapor, using Eqs. (57) and (58). The rate of change of downward solar flux due to CO_2 absorption is

$$\frac{\partial F^{\downarrow}}{\partial u_2} = \frac{\partial}{\partial u_2} \left\{ S_0 \mu_0 [1 - \delta f_5^c A_5^c (u_2/\mu_0)] \right\}$$

$$= -S_0 \mu_0 \left\{ \delta Y(u_2/\mu_0) + f_5^c A_5^c (u_2/\mu_0) \frac{\partial \delta}{\partial u_2} \right\} . \qquad (76)$$

The rate of change of weighting factor with respect to carbon dioxide path length, u_2, is found by a finite difference routine. The rate of change of diffuse upward solar flux is always zero since the total water vapor absorptivity for diffuse radiation in the 2.7 μm band is greater than 500 cm^{-1} so δ is always zero. This occurs because the water vapor path length for the diffuse beam is integrated from the surface to the top of the atmosphere. Consequently, the CO_2 heating rate equation is given by substituting Eq. (76) into Eq. (55):

$$\left(\frac{\partial T}{\partial t}\right)_2 = \frac{\rho_2}{C_p \rho_a} S_0 \mu_0 \{\delta Y_5(u_2/\mu_0) + f_5^c A_5^c (u_2/\mu_0) \frac{d\delta}{du_2}\} . \qquad (77)$$

A typical heating rate curve for carbon dioxide is shown in Fig. 15 for a solar zenith angle of 0.5. Two important points are shown in this figure. First, there is no heating produced below about 12 km where H_2O absorption becomes large and the weight factor for CO_2 absorption

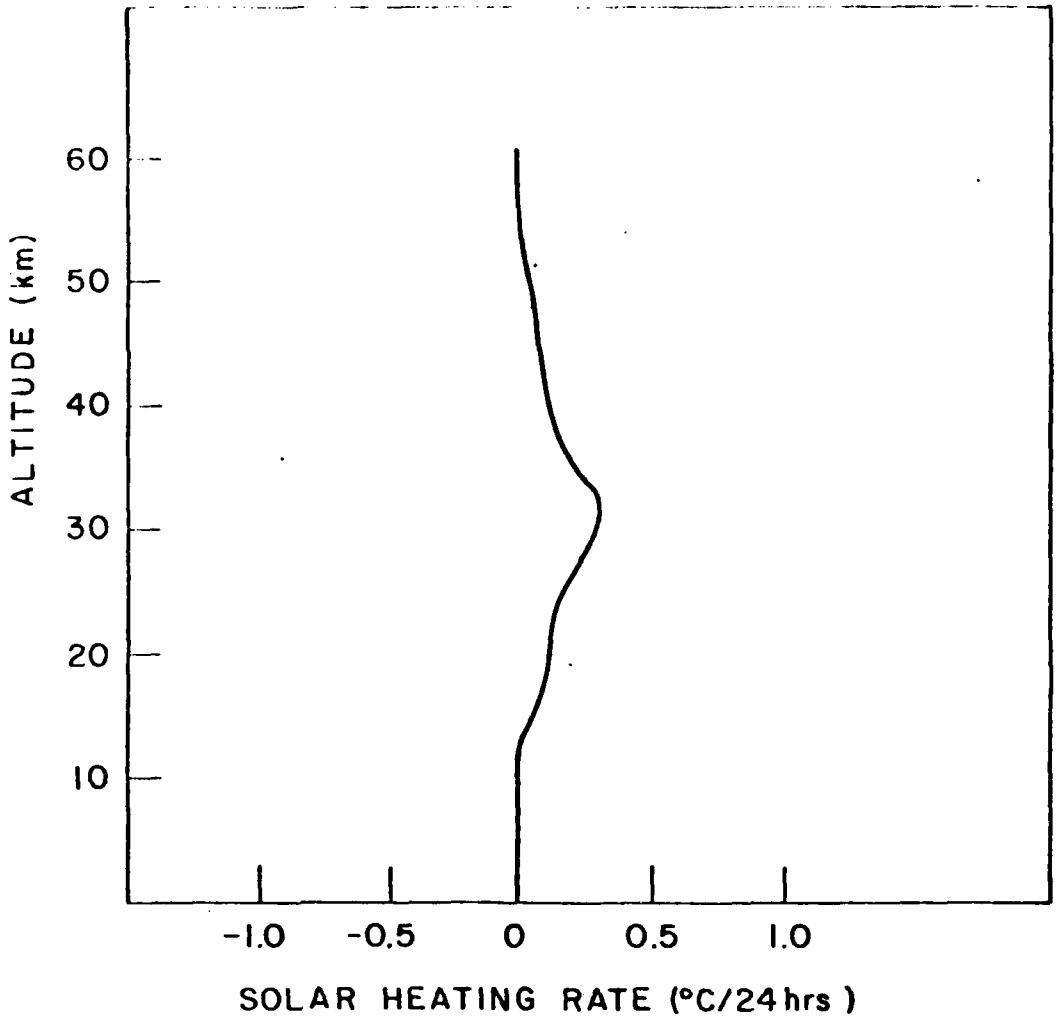

Fig. 15 Carbon dioxide heating rate for a clear midlatitude summer profile ($\mu_0 = 0.5$, $r_g = 1.15$).

approaches zero. Secondly, the maximum carbon dioxide heating occurs about 30 km where the weight factor, δ, has a value of one along with small air densities.

4.3 Total Heating Rate and Net Flux Profiles

Climate modeling not only requires accurate heating rate computation but also accurate net fluxes, especially at the top and bottom of the atmospheric model. The total heating rate is the sum of the individual heating rates for water vapor, ozone, and carbon dioxide at each level. However, the net flux is complicated by Rayleigh scattering. Molecular scattering tends to decrease the direct solar beam and increases the diffuse upward beam as can be seen in Fig. 16 which depicts the downward and upward fluxes for both methods for a tropical profile. The zenith angle is 0.6 and the surface albedo is 0.9. This effect is greatest in the lower troposphere where the air density is largest. It is apparent that the net fluxes, defined by Eq. (45), for these two methods disagree by about 50-75 W m^{-2} throughout the profile, even though the heating profiles, depicted in Fig. 17, show good agreement. An empirical correction must be made to the net flux calculation of the parameterization model if agreement is to be otained with a more exact model which includes Rayleigh scattering effect.

The upward flux at z_a, as given by Eq. (67), is denoted here as $F^{\uparrow}(z_a)$. We then match the upward flux from this equation with the upward flux resulting from diffuse absorption by water vapor in the area below z_a. The latter expression is given by

$$F^{\uparrow}(z_a)_1 = F^{\downarrow}(z_a)\ (1 - r_a - a_1)\ r_g\ (1 - \bar{a}_1)\ . \qquad (78)$$

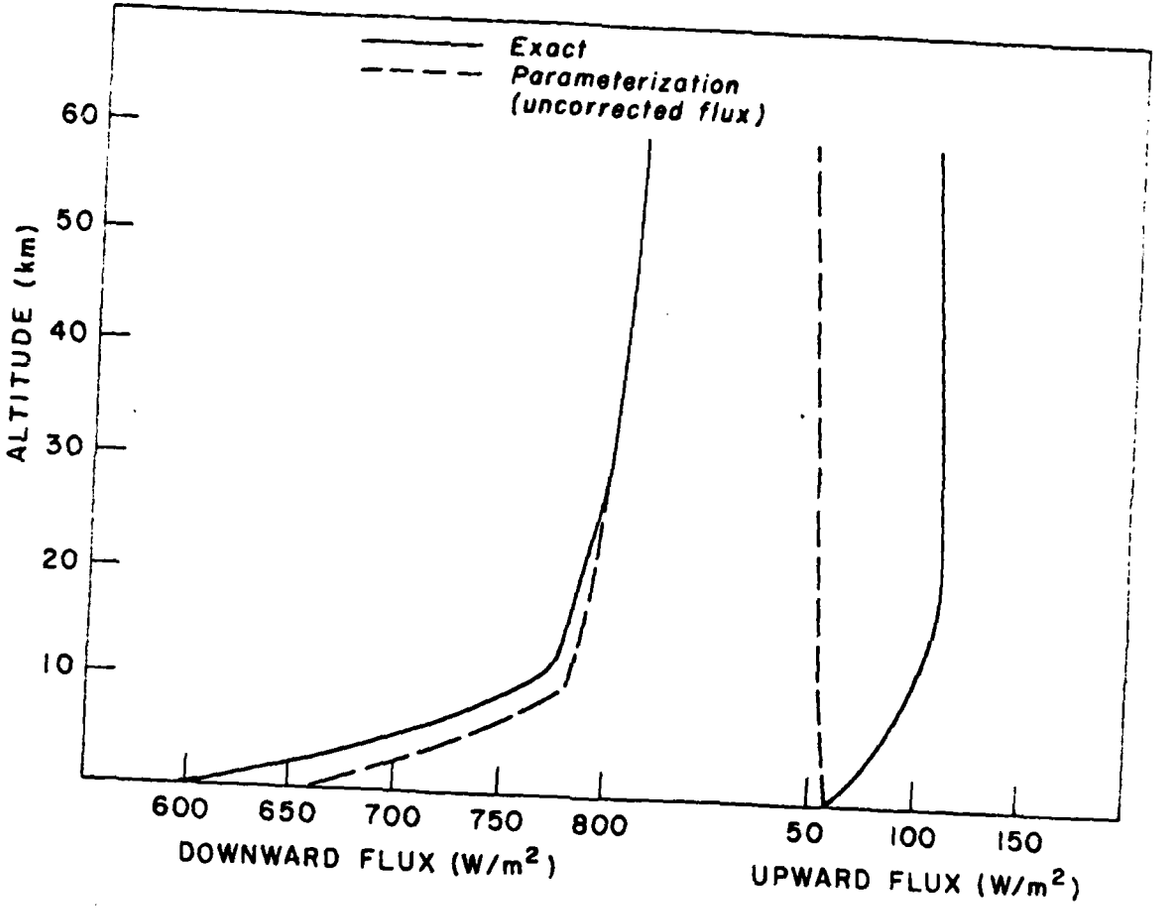

Fig. 16 Downward and upward fluxes for a clear tropical profile ($\mu_0 = 0.6$, $r_g = 0.09$).

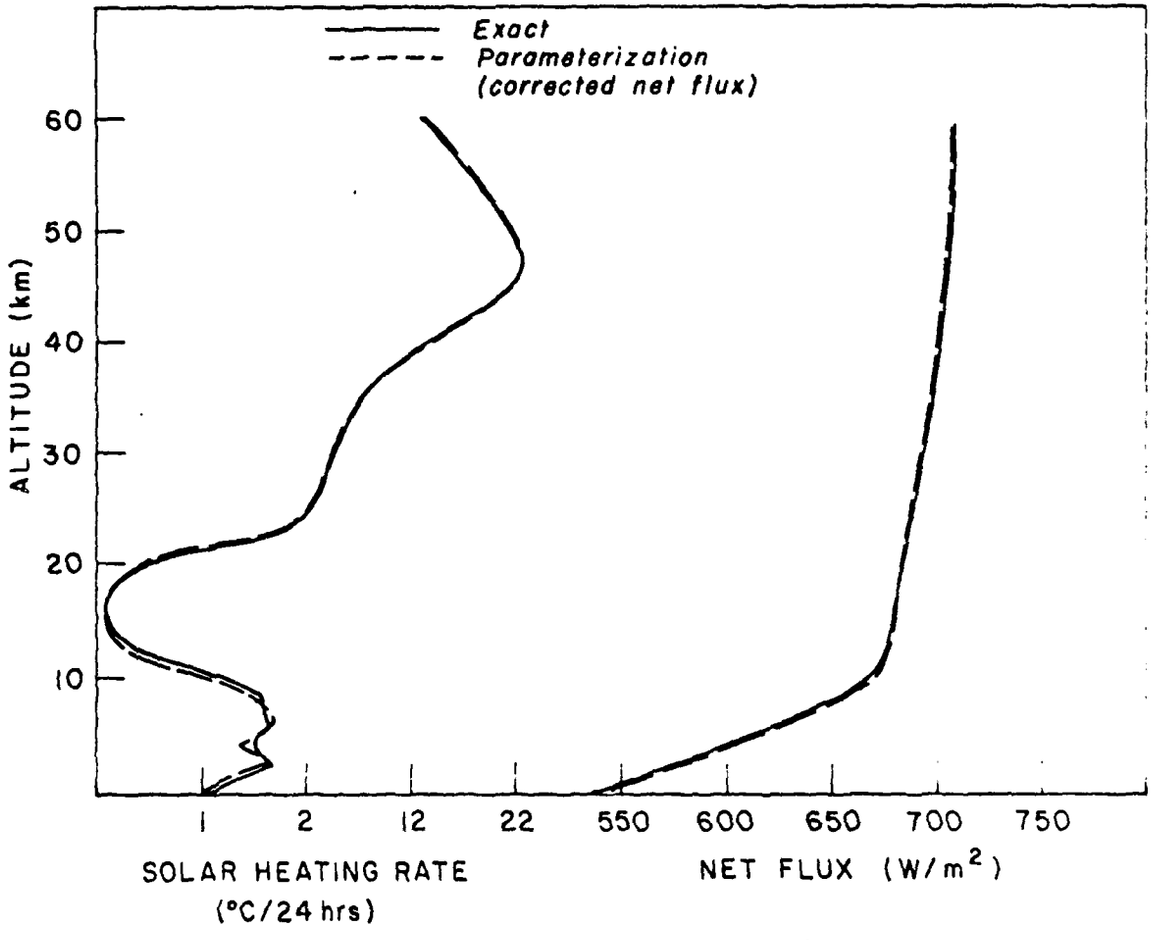

Fig. 17 Atmospheric heating and corrected net fluxes for a clear tropical profile ($\mu_0 = 0.6$, $r_g = 0.09$).

The empirical correction is the difference between these two fluxes, i.e.,

$$C = F^{\uparrow}(z_a) - F^{\uparrow}(z_a)_1 \ . \tag{79}$$

The upward fluxes at all heights below z_a are now adjusted by adding this correction to all upward fluxes initially calculated using Eq. (78). The result of computing the net flux profile in this manner is demonstrated in Fig. 17 which is for the same atmospheric profile used in the preceding figure. Good agreement is now observed in the net flux profile. Extensive experiments utilizing various atmospheric profiles, solar zenith angles and surface albedos also show good agreement (within about 5 W m^{-2}) for net flux profiles between the parameterization and a more exact method.

Section 5

THE BROADBAND APPROACH IN A CLOUDY ATMOSPHERE

5.1 General

Most parameterization schemes use constants or some form of the two-stream/Eddington approximation to calculate cloud reflection and transmission. These types of approximations are inherently inaccurate but their use is justified on the grounds of computational simplicity. They are based on the assumption that all radiation transmitted through the cloud is diffuse and fail to take into account zenith angle dependence on cloud reflection and transmission.

In conjunction with gaseous broadband absorptivities previously defined, clouds and the reflecting surface are considered as a system in developing parameterization equations for fluxes and heating rate calculations. Direct and diffuse broadband solar radiation streams are kept separated in the formulation of upward and downward fluxes. Multiple reflections within the cloud-ground system are handled by a modification to the adding method using diffuse radiation generation functions which are defined at the top of each reflecting layer inside the system. The heating rate within a cloud layer is computed using the flux density divergence for the layer containing the cloud.

5.2 Parameterization of Cloud Optical Properties

Liou and Wittman (1979) have shown that cloud radiative properties

(i.e., absorptivity, transmissivity, and reflectivity) are adequately described by vertical liquid water content (W) and solar zenith angle (μ_0) once the cloud microphysical properties have been established. However, their parameterization, which employed 16 coefficients each for cloud reflection and transmission, proved to be cumbersome. In addition, their definitions were not in complete agreement with the broadband gaseous absorptivity developed in this study as pointed out in Section 3. Thus, a new cloud parameterization was carried out for reflection and transmission. After trial and error using a number of known mathematical functions, the best cloud reflection and transmission parameterization takes the form

$$S(W,\mu_0) = \left[\sum_{n=1}^{4} a_n(W)\ \mu_0^{n-1}\right]^{-1} , \tag{80}$$

where

$$a_n(W) = \sum_{m=1}^{4} b_{n,m}\ W^{m-1} , \quad n = 1,2,3,4 , \tag{81}$$

and $S(W,\mu_0)$ refers to both cloud reflection and transmission. In these equations, superscripts n and m on μ_0 and W represent the index power.

This parameterization is accomplished in the following manner. Cloud optical properties are obtained for five cloud thicknesses and five solar zenith angles making 25 data points for each cloud optical property. The number of data points needed to define reflection and transmission is reduced significantly from the 90 used by Liou and Wittman (1979), since the shape of the curves fitted are known in advance. The cloud radiative property is plotted against the solar zenith angle for a constant vertical liquid water content as depicted

in Fig. 18 (the stratus cloud transmission is employed here for illustration). This produces a family of curves which is then fitted by polynomials described in Eq. (80). Next, values of $a_n(W)$ are plotted against W as shown in Fig. 19 (cumulus reflection is used for illustration) and this family of curves are fit by a polynomial of the type given in Eq. (81). The result is that each cloud optical property is parameterized using six to nine coefficients except for cirrus which require 16 coefficients. The accuracy of the fit for each cloud radiative property is shown in Table 8 along with the cloud thicknesses and range of vertical liquid water content used in the parameterization. This parameterization method fits the cloud reflection generated by the discrete-ordinates method within about 0.5% on the average, while the cloud transmission is fit within about 0.25%. A more detailed comparison of the cloud radiative properties generated by the discrete-ordinates method and the parameterization are given in Figs. 20 and 21. Figure 20 shows the comparison between the altostratus transmission at various W and μ_0, while Fig. 21 gives the comparison between the cirrus reflection. The predictor coefficients given by Eq. (81) are listed in Tables 9 - 16 for the four cloud types.

This method required the surface albedo to be set to zero and assumed that Rayleigh scattering was negligible, which it is for all clouds except cirrus. When cirrus is the only cloud present in the atmosphere and the surface albedo is zero, the effect of Rayleigh scattering can be seen by summing the absorption, transmission, and reflection for each case as shown in Table 17. The sum should be one, which it is for all other cloud types, but is greater than one in all cirrus cases. This occurs because in clouds with high transmission, Rayleigh

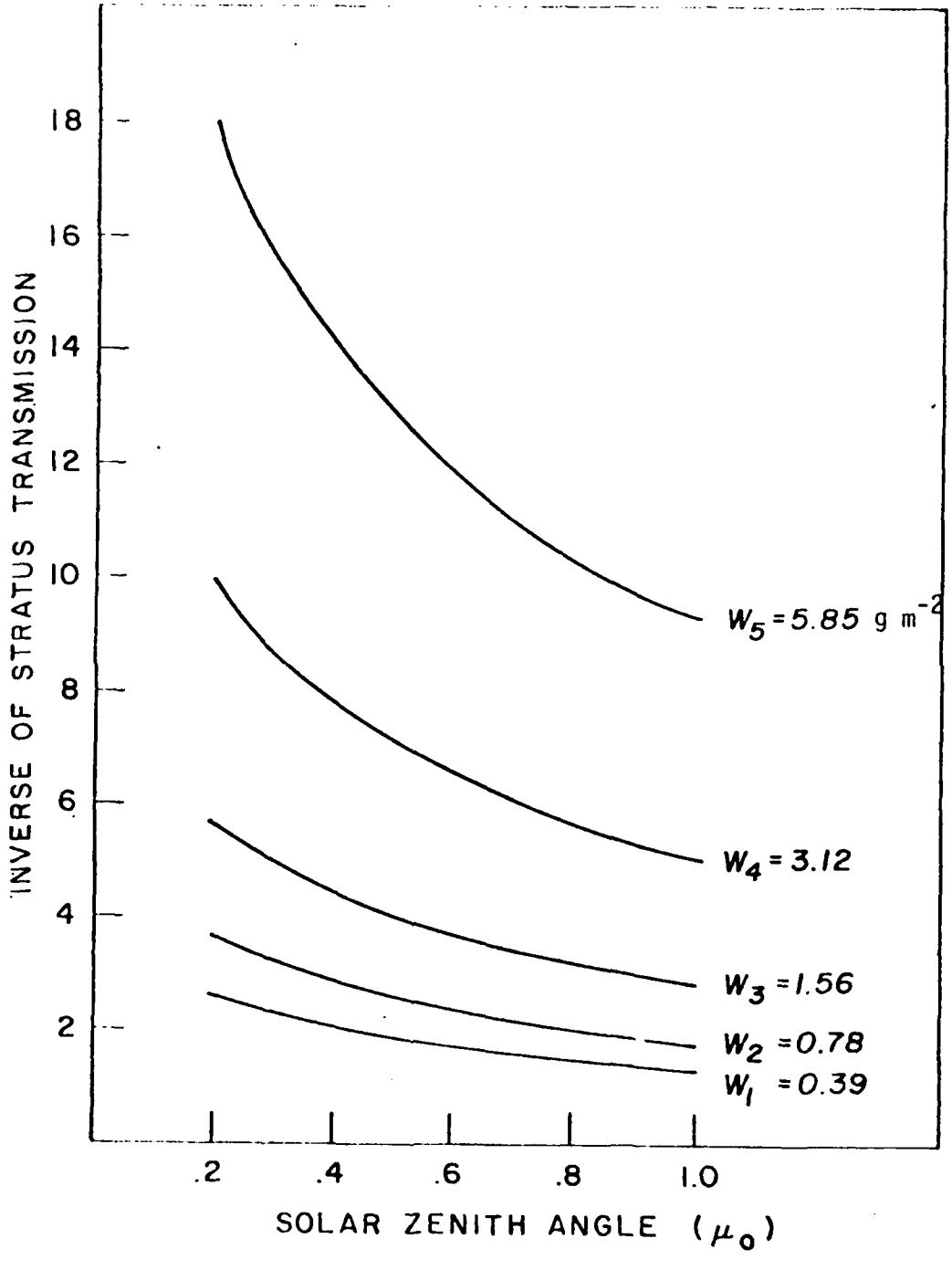

Fig. 18 Inverse of the stratus transmission versus the solar zenith angle for a constant liquid water content.

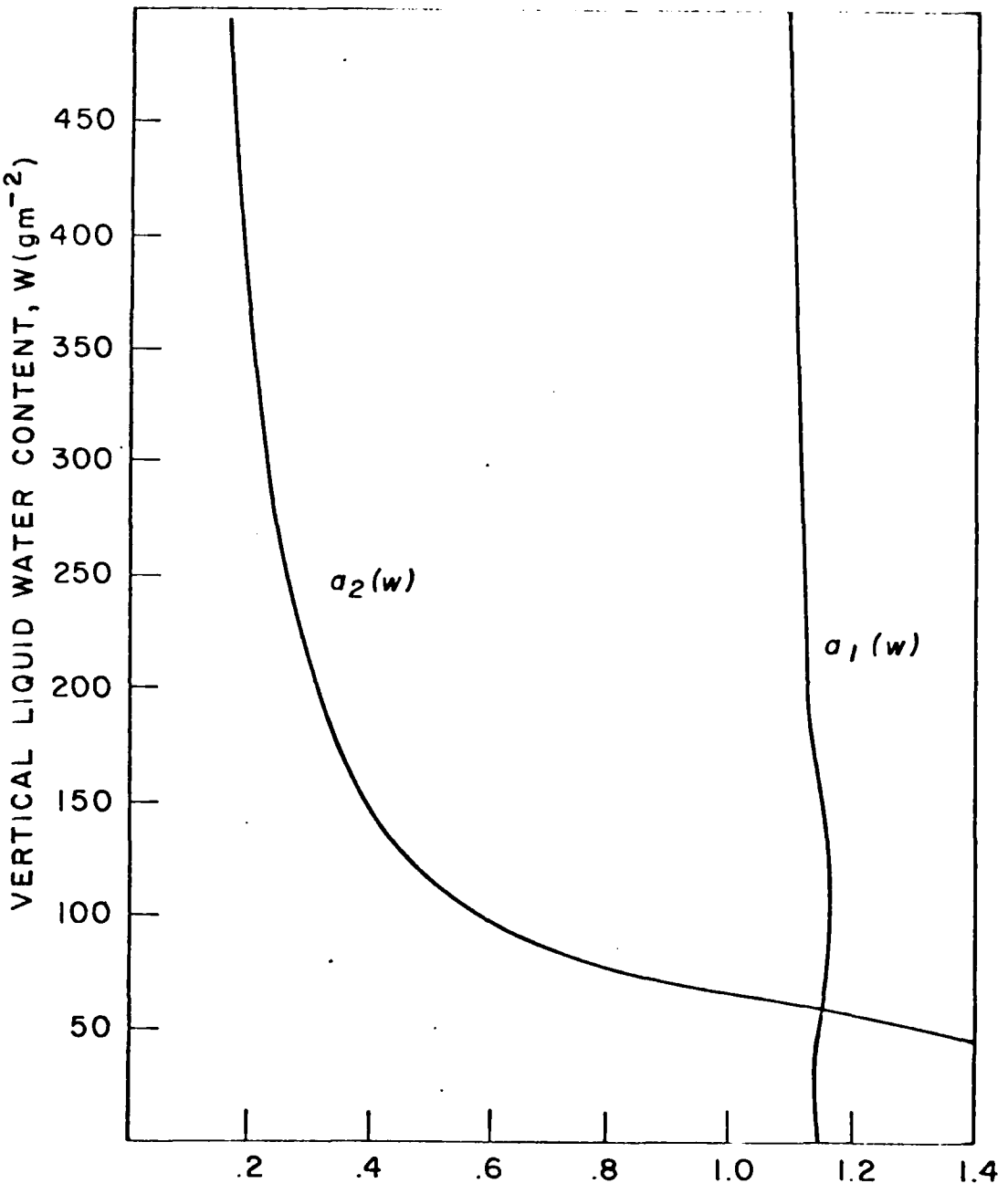

Fig. 19 Coefficients $a_{1,m}(w)$ and $a_{2,m}(w)$ versus the vertical liquid water content, W, for the cumulus reflection.

Table 8 Comparisons of the parameterization values of reflection and transmission to those obtained by the discrete-ordinates method.

Cloud Type	Test Range of Cloud Thickness (km)	Test Range of Vertical Liquid Water/ Ice Content (10^2 g m^{-2})	Range of Data For Reflection	Average Accuracy of Fit	Range of Data for Transmission	Average Accuracy of Fit
Stratus	.10-.75	.78-5.85	.394-.869	.0063	.055-.746	.0029
Cumulus	.15-1.5	.495-4.95	.398-.893	.0060	.045-.567	.0023
Alto-stratus	.15-1.5	.36-3.60	.617-.903	.0082	.015-.308	.0014
Cirrus	.10-1.5	0.0034-0.05	.044-.478	.0049	.418-.977	.0026

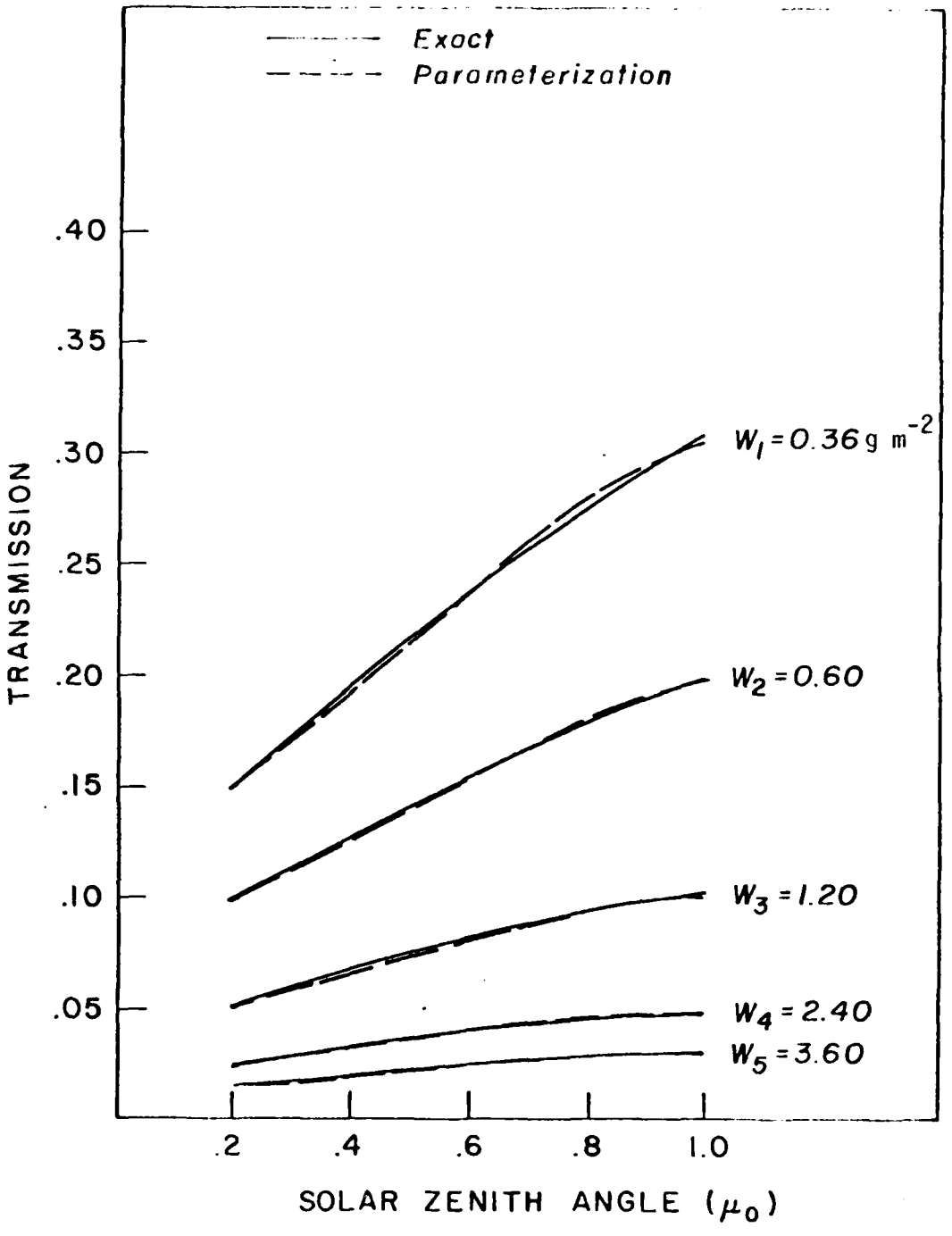

Fig. 20 Comparison of the exact (——) and parameterized (----) methods for the altostratus transmission for various solar zenith angles and liquid water contents.

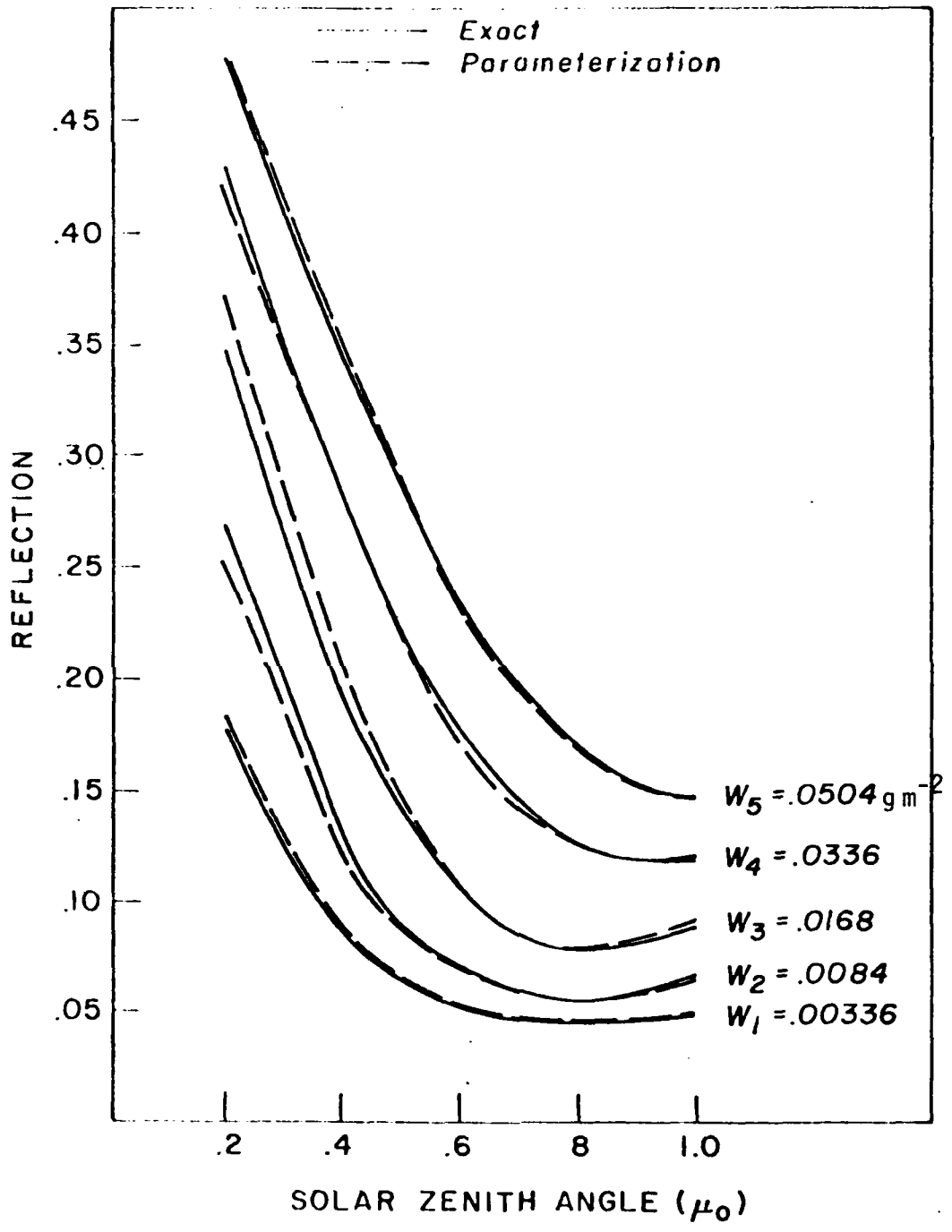

Fig. 21 Comparison of the exact (——) and parameterized (----) methods for the cirrus reflection for various vertical ice contents and solar zenith angles.

Table 9 Predictor coefficients for the stratus reflection with a cloud base at 1 km.

$b_{n,m}$ \ m	1	2	3
$b_{1,m}$	1.1770387	-0.00117267	-0.00155989
$b_{2,m}$	-0.28671732	1.3770553	-0.08290901

Table 10 Predictor coefficients for the stratus transmission with a cloud base at 1 km.

$b_{n,m}$ \ m	1	2	3
$b_{1,m}$	2.1467536	3.0933553	0.06150582
$b_{2,m}$	-2.5417457	-3.2657469	-0.06695797
$b_{3,m}$	1.2185517	1.4555492	0.03479150

Table 11 Predictor coefficients for the cumulus reflection with a cloud base at 2 km.

$b_{n,m}$ \ m	1	2	3
$b_{1,m}$	1.1628220	-0.01345690	-0.00016240
$b_{2,m}$	-0.18836070	2.0125731	-0.15793160

Table 12 Predictor coefficients for the cumulus transmission with a cloud base at 2 km.

$b_{n,m}$ \ m	1	2	3
$b_{1,m}$	2.0945402	4.8603017	0.07852117
$b_{2,m}$	-2.5646724	-5.332700	-0.11783940
$b_{3,m}$	1.2151820	2.5195630	0.05836719

Table 13 Predictor coefficients for the altostratus reflection with a cloud base at 4 km.

$b_{n,m}$ \ m	1	2	3
$b_{1,m}$	1.1818476	-0.06928557	0.01251502
$b_{2,m}$	0.74679249	4.7541147	-0.71275650

Table 14 Predictor coefficients for the altostratus transmission with a cloud base at 4 km.

$b_{n,m}$ \ m	1	2	3
$b_{1,m}$	2.1468193	17.022049	1.4969625
$b_{2,m}$	-2.8530089	-18.961483	-2.0434877
$b_{3,m}$	1.4058295	8.9499630	1.0196345

Table 15 Predictor coefficients for the cirrus reflection with a cloud base at 8 km.

m $b_{n,m}$	1	2	3	4
$b_{1,m}$	0.875416	0.856228×10^{1}	-0.361108×10^{5}	0.393977×10^{6}
$b_{2,m}$	0.185111×10^{2}	-0.855647×10^{4}	0.354341×10^{6}	-0.386822×10^{7}
$b_{3,m}$	0.667364×10^{2}	0.117047×10^{5}	-0.595519×10^{6}	0.689059×10^{7}
$b_{4,m}$	-0.622586×10^{2}	-0.529730×10^{4}	0.313787×10^{6}	-0.376506×10^{7}

Table 16 Predictor coefficients for the cirrus transmission with a cloud base at 8 km.

m $b_{n,m}$	1	2	3	4
$b_{1,m}$	0.107355×10^{1}	0.111099×10^{3}	-0.243151×10^{4}	0.222924×10^{5}
$b_{2,m}$	-0.352062	-0.401698×10^{3}	0.111740×10^{5}	-0.106569×10^{6}
$b_{3,m}$	0.505344	-0.491364×10^{3}	-0.152987×10^{5}	0.150421×10^{6}
$b_{4,m}$	-0.225506	-0.193980×10^{3}	0.649287×10^{4}	-0.655727×10^{5}

Table 17 Sum of Cloud Reflection, Transmission, and Absorption in a Cirrus Cloudy Atmosphere (r_g = 0.0)

Cloud Thickness (km) / Solar Zenith Angle (μ_0)	.1	.25	.5	1.0	1.5
.2	1.05640	1.04325	1.03339	1.02554	1.02139
.4	1.05083	1.04866	1.04466	1.03738	1.03195
.6	1.04530	1.04639	1.04632	1.04314	1.03912
.8	1.03949	1.04059	1.04152	1.04149	1.04024
1.0	1.03335	1.03252	1.03215	1.03321	1.03476

scattering will reflect flux arriving below the cloud upward again. In the discrete-ordinates method, this additional upward flux cannot be distinguished from flux originally transmitting through the cloud. However, the effect of Rayleigh scattering on cirrus clouds can be parameterized in the same way that cloud reflection and transmission are parameterized for all cloud types. Figure 22 depicts the inverse of the Rayleigh effect on cirrus clouds plotted against the solar zenith angle for a constant liquid water content. Coefficients $a_n(W)$ in Eq. (80) are again obtained by fitting this family of curves by a third-order polynomial in the zenith angle. Figure 23 shows the plot of these coefficients versus liquid water content from which $b_{n,m}$ in Eq. (81) are obtained after fitting this family of curves with the same type of polynomials. The accuracy of this fit on the average is within 0.026% of the values obtained by the discrete-ordinates method. The coefficients, $b_{n,m}$, are listed in Table 18.

Several points should be understood when applying these prediction coefficients listed in Tables 9 through 17. First, they apply to solar zenith angles within the range 0.2 - 1.0. Secondly, for the reflection of stratus, cumulus, and altostratus clouds, they predict b_2^{-1} not b_2. It was necessary to predict b_2^{-1} if the number of coefficients used to predict reflection is to be kept to six.

An inflection point exists at $\mu_0 = .2$ for most cloud types; thus, large errors could result if these coefficients are applied with solar zenith angles less than 0.2. Errors are also probable when used with cloud thicknesses smaller than those shown in Table 17 but only small errors would result by using thicker clouds. The vertical liquid water/ice content of the cloud is given by

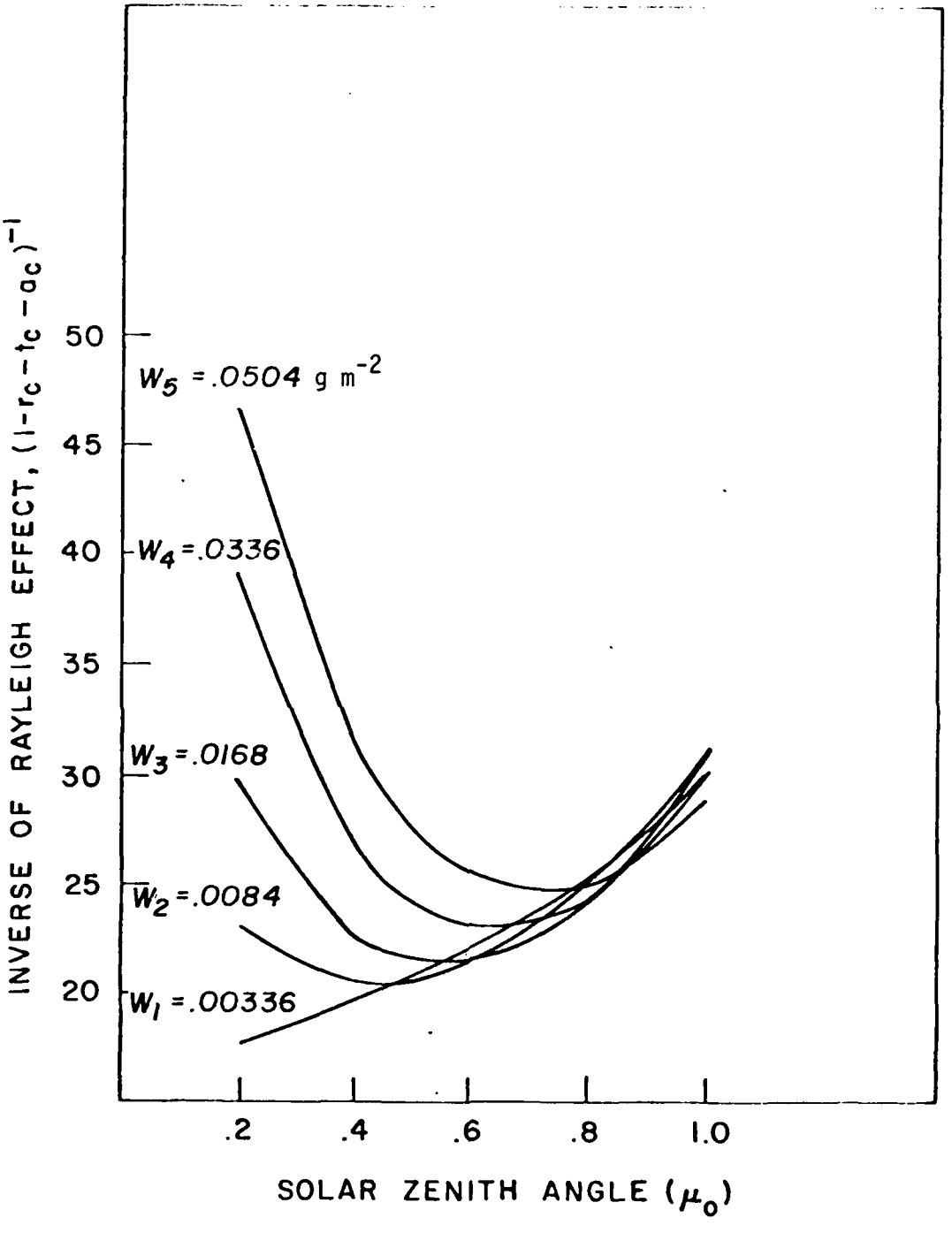

Fig. 22 Inverse of the Rayleigh scattering effect on cirrus clouds versus solar zenith angle for a constant liquid water content.

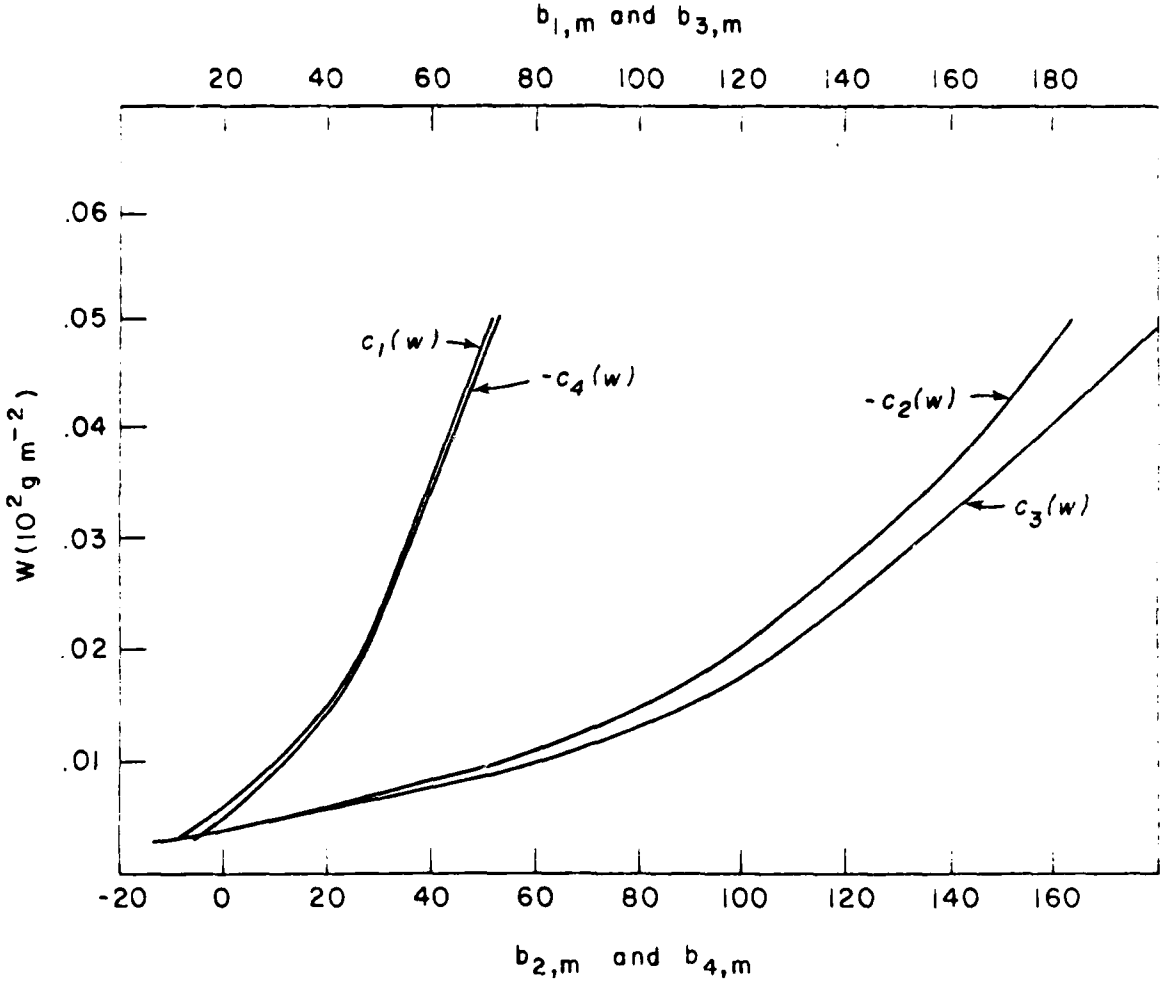

Fig. 23 Coefficients $b_{1,m}(w)$, $b_{2,m}(w)$, $b_{3,m}(w)$ and $b_{4,m}(w)$ due to the Rayleigh effect versus the vertical ice content.

Table 18 Predictor coefficients due to the Rayleigh effect with a cloud base at 8 km.

$b_{n,m}$ \ m	1	2	3	4
$b_{1,m}$	0.543956×10^{1}	0.330860×10^{4}	-0.705047×10^{5}	0.625258×10^{6}
$b_{2,m}$	0.500547×10^{2}	-0.126917×10^{5}	0.305654×10^{6}	-0.274697×10^{7}
$b_{3,m}$	-0.492899×10^{2}	0.138483×10^{5}	-0.349088×10^{6}	0.321333×10^{7}
$b_{4,m}$	0.231012×10^{2}	-0.422886×10^{4}	0.104622×10^{6}	-0.100449×10^{7}

$$W = w\,\Delta z \ , \tag{82}$$

where Δz is the cloud thickness in meters and w is 0.78, 0.33, 0.24, and 0.00336 g m^{-3} for stratus, cumulus, altostratus, and cirrus, respectively. The units of W are in 10^2 g m^{-2}.

Additionally, a temperature correction to the cloud reflection and transmission can be made using the form,

$$S(w,\mu_0,\bar{T}) = S(w,\mu_0) + C(\bar{T}) \ , \tag{83}$$

where $S(w,\mu_0)$ is determined from Eq. (80) and $C(\bar{T})$ the temperature correction depends on the mean temperature of the cloud. The temperature correction to cloud reflection and transmission is an important new concept in the parameterization of cloud radiative properties because it allows the mean temperature and consequently the base of the cloud to vary.

The correction, $C(\bar{T})$, was found for a 40 degree temperature range for each cloud type considered in the research. The temperature correction was made by varying the temperature of the cloud in the more exact method and plotting the resulting radiative property against the mean cloud temperature for a given solar zenith angle as shown in Fig. 24. Since each curve closely approximates a straight line, the parameterization could easily be made by describing the slope of each curve as a function of zenith angle for a given vertical liquid water content, as shown in Fig. 25. The result is a temperature coefficient of the form

$$C(w,\mu_0,\bar{T}) = (\bar{T} - \bar{T}_{Ref}) \sum_{n=1}^{3} c_n(W)\ \mu_0^{n-1} \ , \tag{84}$$

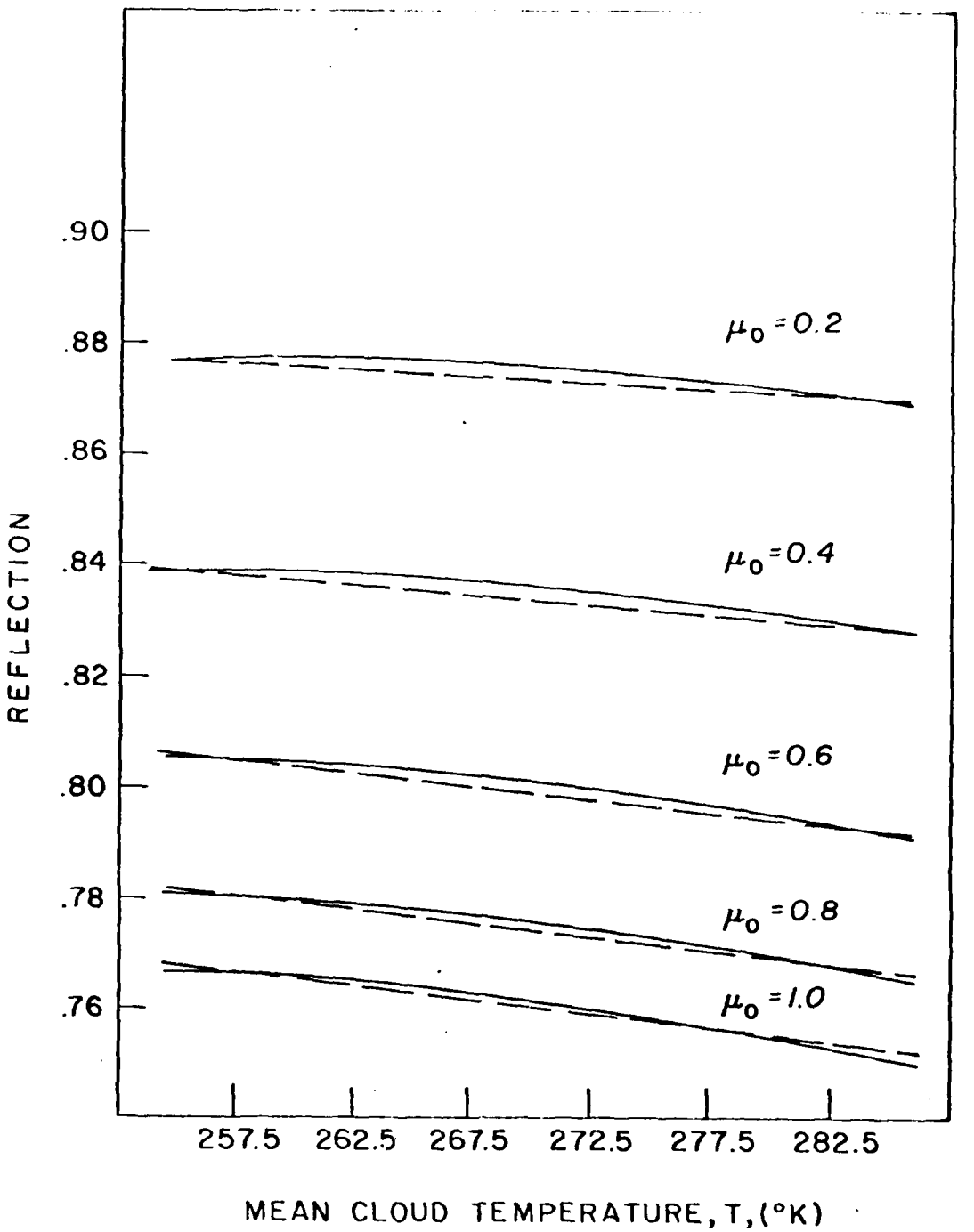

Fig. 24 The cumulus reflection versus the mean cloud temperature for constant solar zenith angles.

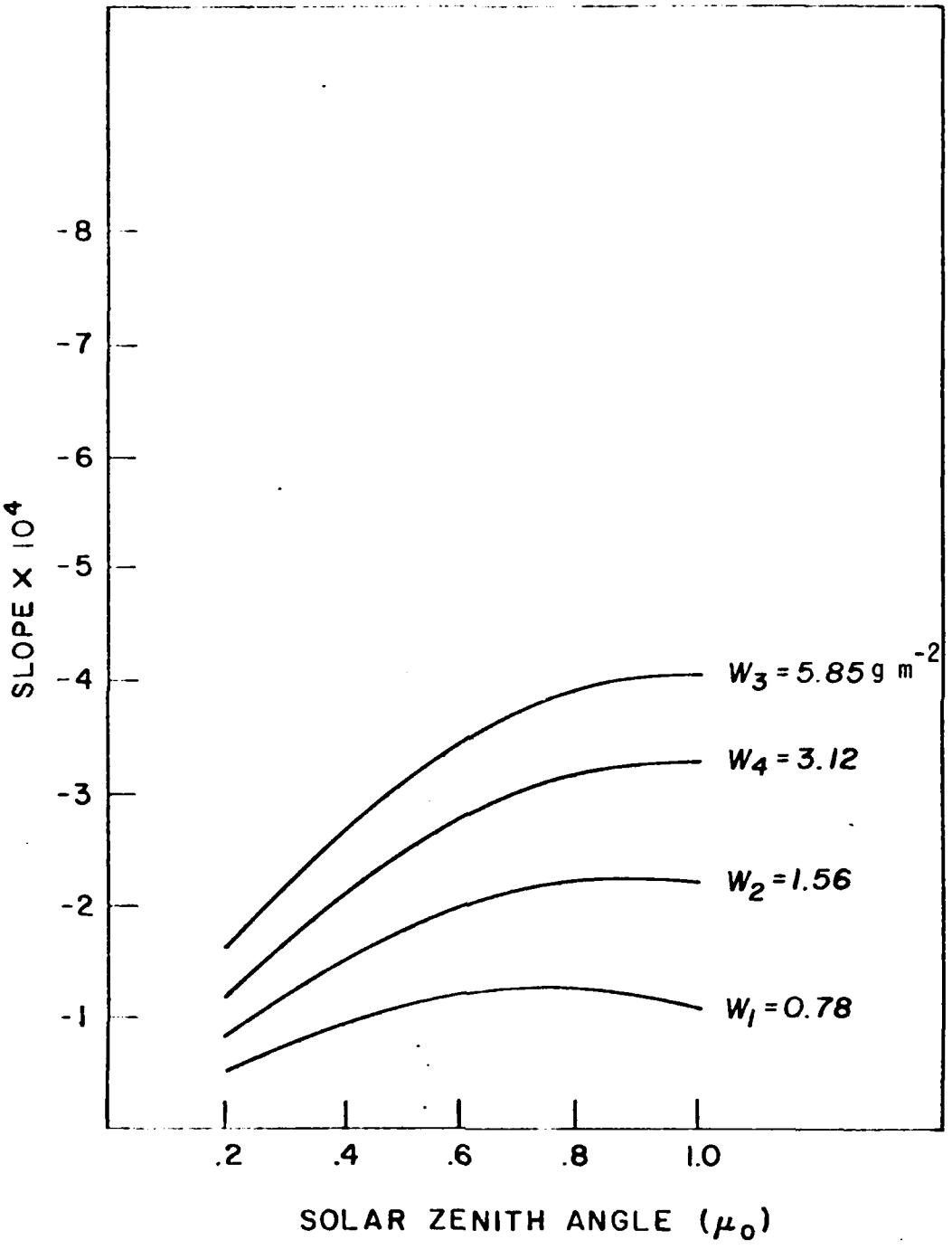

Fig. 25 Slope of the stratus reflection versus the solar zenith angle for constant vertical liquid water contents.

where

$$c_n(W) = \sum_{m=1}^{3} d_{n,m} W^{m-1} \quad . \tag{85}$$

$\overline{T}$ is the mean temperature of the cloud, and $\overline{T}_{Ref}$ is determined from the reference cloud base temperature for each cloud type. These reference temperatures are 265.2, 255.7, 231.7, and 268.7° K for cumulus, altostratus, cirrus, and stratus, respectively. These predictor coefficients and applicable temperature ranges are listed in Tables 19 - 26. The result of the cloud radiative parameterization is that once the cloud type, thickness, and base are fixed, the reflection and transmission are defined for given zenith angles. Deviations of the parameterized values from those of the more exact method when the temperature correction is made are within the range shown in Table 8.

5.3 Heating Rates and Net Fluxes in Cloudy Atmospheres

Heating rate calculations for an atmosphere containing a single cloud are divided into three general areas: the area above the cloud top, the area below the cloud base, and the cloud layer as shown in Fig. 26. In the formulation, direct and diffuse components of the solar flux contribute to the net flux and heating rate at each level in the cloud layer.

The cloud has a transmission, $t_1(\mu_0)$ and reflection, $r_1(\mu_0)$ which are functions of the vertical liquid water content and solar zenith angle obtained for an identical cloud when the surface albedo is set to zero. Additionally, the cloud has a global (or average) reflection $\overline{r}_1$, and global transmission, $\overline{t}_1$, with respect to diffuse radiation.

Table 19 Predictor coefficients for the temperature correction to the cumulus reflection. The temperature range used is from 250 to 290° K.

$d_{n,m}$ \ m	1	2	3
$d_{1,m}$	$1.66157x10^{-5}$	$-2.87867x10^{-5}$	$1.55598x10^{-7}$
$d_{2,m}$	$-4.25249x10^{-4}$	$-3.18357x10^{-4}$	$2.83799x10^{-5}$
$d_{3,m}$	$3.97082x10^{-4}$	$6.38750x10^{-4}$	$7.32911x10^{-4}$

Table 20 Predictor coefficients for the temperature correction to the cumulus transmission. The temperature range used is from 250 to 290° K.

$d_{n,m}$ \ m	1	2	3
$d_{1,m}$	$6.97908x10^{-6}$	$-2.16932x10^{-5}$	$2.39661x10^{-6}$
$d_{2,m}$	$-4.78117x10^{-4}$	$1.37384x10^{-4}$	$1.31107x10^{-5}$
$d_{3,m}$	$1.13848x10^{-4}$	$-2.53503x10^{-5}$	$1.82536x10^{-6}$

Table 21 Predictor coefficients for the temperature correction to the altostratus reflection. The temperature range used is from 245 to 285° K.

$d_{n,m}$ \ m	1	2	3
$d_{1,m}$	2.00546×10^{-5}	-5.73065×10^{-5}	5.80363×10^{-6}
$d_{2,m}$	-6.03168×10^{-4}	-2.35728×10^{-4}	4.12499×10^{-5}
$d_{3,m}$	3.57757×10^{-4}	9.05252×10^{-5}	-1.28976×10^{-5}

Table 22 Predictor coefficients for the temperature correction to the altostratus transmission. The temperature range used is from 245 to 285° K.

$d_{n,m}$ \ m	1	2	3
$d_{1,m}$	-6.24068×10^{-6}	-1.93991×10^{-5}	5.20037×10^{-6}
$d_{2,m}$	-3.48751×10^{-4}	2.56122×10^{-4}	-4.61342×10^{-5}
$d_{3,m}$	1.02351×10^{-4}	-7.42415×10^{-5}	1.32371×10^{-5}

Table 23 Predictor coefficients for the temperature correction to the cirrus reflection. The temperature range used is from 205 to 245° K.

$b_{n,m}$ \ m	1	2	3
$b_{1,m}$	-4.80458×10^{-5}	-5.23109×10^{-3}	4.93013×10^{-2}
$b_{2,m}$	2.39591×10^{-4}	7.74293×10^{-4}	-4.28070×10^{-2}
$b_{3,m}$	-1.84610×10^{-4}	2.96808×10^{-3}	2.89473×10^{-3}

Table 24 Predictor coefficients for the temperature correction to the cirrus transmission. The temperature range used is from 205 to 245° K.

$b_{n,m}$ \ m	1	2	3
$b_{1,m}$	-1.69587×10^{-4}	4.45949×10^{-3}	-4.90636×10^{-2}
$b_{2,m}$	-4.45260×10^{-5}	-3.44686×10^{-2}	4.84774×10^{-1}
$b_{3,m}$	1.71100×10^{-4}	1.75961×10^{-2}	-3.05332×10^{-1}

Table 25 Predictor coefficients for the temperature correction to the stratus reflection. The temperature range used is from 260 to 300° K.

$b_{n,m}$ \ m	1	2	3
$b_{1,m}$	1.97809×10^{-5}	-4.27582×10^{-6}	-5.50859×10^{-7}
$b_{2,m}$	-3.35439×10^{-4}	-1.52791×10^{-4}	1.34508×10^{-5}
$b_{3,m}$	2.44638×10^{-4}	4.42694×10^{-5}	-3.42760×10^{-6}

Table 26 Predictor coefficients for the temperature correction to the stratus transmission. The temperature range used is from 260 to 300° K.

$b_{n,m}$ \ m	1	2	3
$b_{1,m}$	2.00573×10^{-5}	-1.04484×10^{-5}	6.68055×10^{-7}
$b_{2,m}$	-4.00004×10^{-4}	7.22931×10^{-5}	-3.47647×10^{-6}
$b_{3,m}$	9.31966×10^{-5}	-1.11568×10^{-5}	-4.32319×10^{-8}

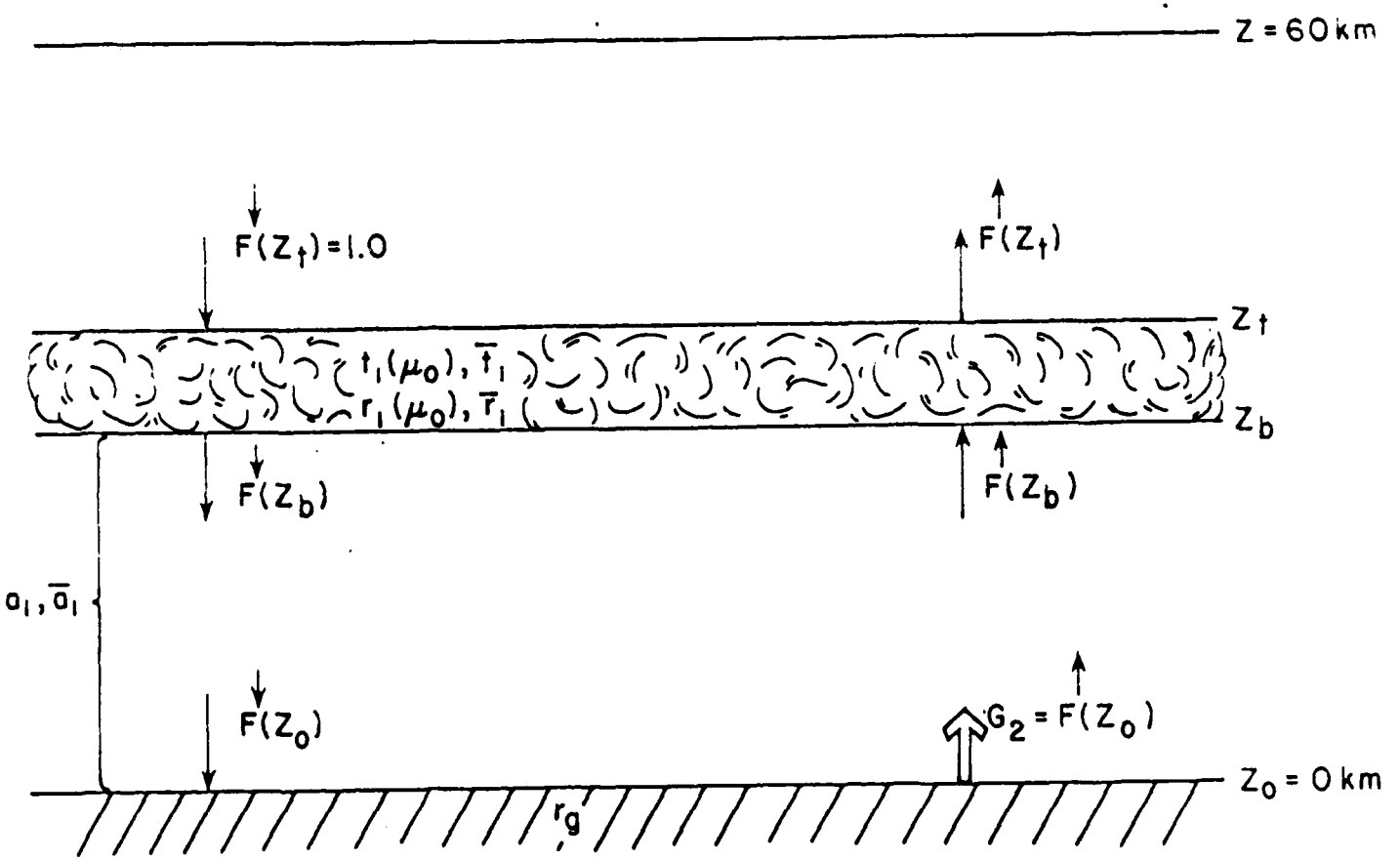

Fig. 26 Single cloud and reflecting surface system.

The Lambert reflecting surface at $z = 0$, has a value of r_g and subscripts t and b represent the cloud top and base, respectively.

Let a_1 be the total gaseous absorptivity between the reflecting surface and cloud base, and $\bar{a}_1$ the diffuse absorptivity in the same layer. Define G_2 as the "generation function" which generates the total upward diffuse flux at the surface and assign the downward flux at the cloud top a value of unity for simplicity, i.e., $F^{\downarrow}(z_t) = 1$. Let the upward flux at $z = 0$ after the first reflection be D. Then, the total upward flux at $z = 0$, defined by G_2, is given by the infinite series,

$$G_2 = D + D\, r_g\, \bar{r}_1^{*}\, (1 - \bar{a}_1)^2 + D\, r_g^2\, \bar{r}_1^{*2}\, (1 - \bar{a}_1)^4 + \ldots \qquad (86)$$

where D, as shown in Fig. 27 is given by

$$D = t_1(\mu_0)\, (1 - a_1)\, r_g\, . \qquad (87)$$

The star in Eq. (86) denotes reflected radiation originating below the cloud. This infinite series converges to

$$G_2 = D\, r_g\, \bar{r}_1^{*}\, (1 - \bar{a}_1)^2\, [1 - (1 - \bar{a}_1)^2\, r_g\, \bar{r}_1^{*}]^{-1}\, . \qquad (88)$$

If S_2 is defined as

$$S_2 = (1 - \bar{a}_1)^2\, r_g\, \bar{r}_1^{*}\, [1 - (1 - \bar{a}_1)^2\, r_g\, \bar{r}_1^{*}]^{-1}\, , \qquad (89)$$

then G_2 can be expressed by

$$G_2 = \underbrace{t_1(\mu_0)\, (1 - a_1)}_{A}\, r_g\, \underbrace{(1 + S_2)}_{B}\, , \qquad (90)$$

where term A represents the direct solar flux reaching the reflecting

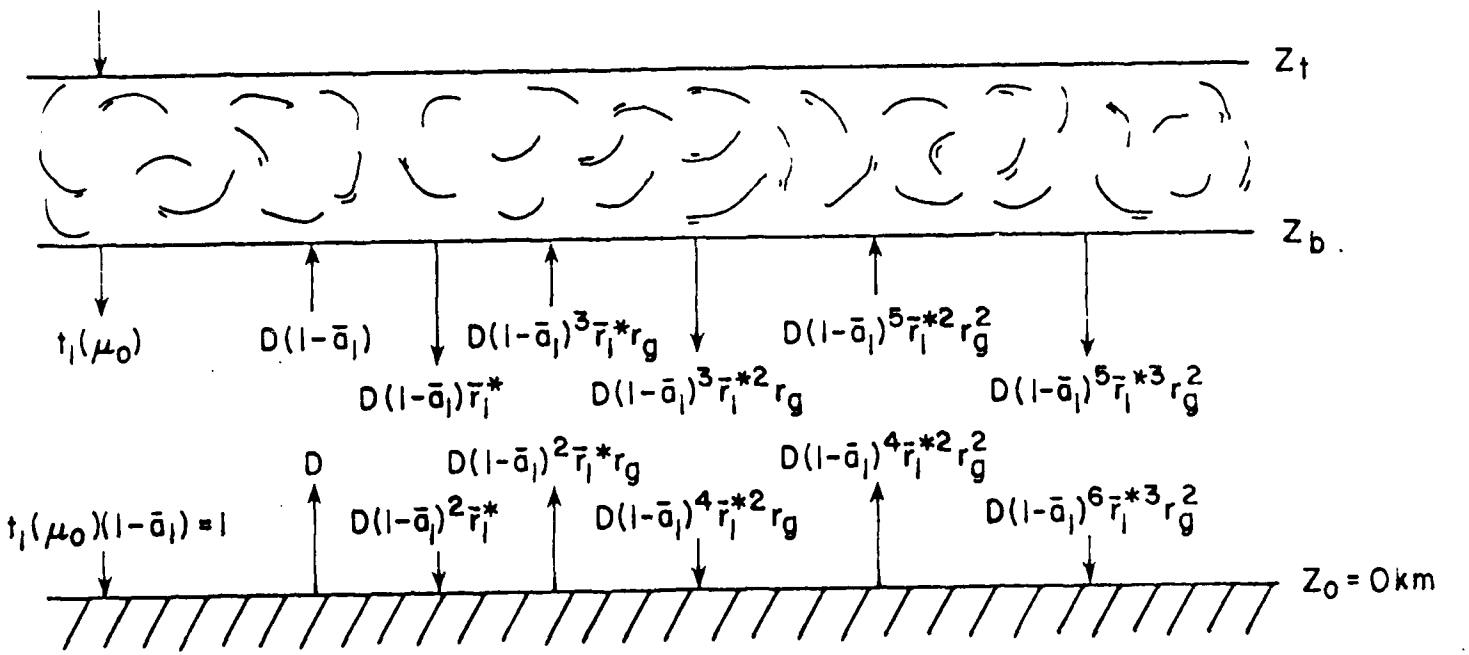

Fig. 27 Multiple reflections between the cloud and the surface.

surface and term B contains the multiple reflection effects which occur between the cloud and the reflecting surface. Since the downward flux at the cloud top is assumed to be unity, the upward flux at the surface $F^{\uparrow}(z_0) = G_2$.

The upward flux at the cloud base is the total upward flux at the earth's surface attenuated by the diffuse absorptivity of the atmospheric layer between z_0 and the cloud base. Consequently,

$$F^{\uparrow}(z_b) = G_2 \ (1 - \bar{a}_1) \ . \tag{91}$$

The downward flux arriving at the cloud base has two components. The first is direct solar flux transmitted through the cloud and the second represents diffuse solar flux originating at z_0 and reflected by the cloud. This solar flux is represented by

$$F^{\downarrow}(z_b) = t_1(\mu_0) + G_2 \ (1 - \bar{a}_1) \ \bar{r}_1^* \ . \tag{92}$$

The total downward flux at z_0 is Eq. (92) with each component attenuated by absorption in the layer between z_0 and the cloud base. Thus,

$$F^{\downarrow}(z_0) = t_1(\mu_0) \ (1 - a_1) + G_2 \ (1 - \bar{a}_1)^2 \ \bar{r}_1^* \ . \tag{93}$$

The total upward flux at the cloud top is the sum of the direct downward flux reflected by the cloud and additional diffuse solar flux which originates at z_0 and is subsequently transmitted through the cloud during the multiple reflection process. This final expression is given by

$$F^{\uparrow}(z_t) = r^*(\mu_0) = r_1(\mu_0) + G_2 \ (1 - \bar{a}_1) \ \bar{t}_1^* \ . \tag{94}$$

The heating rate at the middle of the cloud is

$$\frac{\partial T}{\partial t} = - \frac{1}{C_p \bar{\rho}_a} \frac{\Delta F}{\Delta z} , \tag{95}$$

where the radiative flux density divergence is given by

$$\Delta F = [F^{\downarrow}(z_t) - F^{\uparrow}(z_t)] - [F^{\downarrow}(z_b) - F^{\uparrow}(z_b)] , \tag{96}$$

and $\bar{\rho}_a$ is the mean air density of the cloud layer and Δz is the cloud thickness.

Since the upward and downward fluxes at the cloud base contain direct and diffuse components, heating rates in the clear atmosphere are determined as previously described for a cloud free atmosphere with the exception that the upward flux at level z above the cloud top is

$$F^{\uparrow}(z) = S_0 \mu_0 [1 - A(z_t)] r^*(\mu_0) [1 - \bar{A}(z)] \qquad z > z_t \tag{97}$$

where $\bar{A}(z) = A(1.66\ z)$. On the other hand, the downward and upward fluxes at level z below the cloud base takes the form

$$\begin{cases} F^{\downarrow}(z) = S_0 \mu_0 [1 - A(z_t)] \{ t_1(\mu_0) [1 - A(z)] \\ \qquad\qquad + G_2 (1 - \bar{a}_1) \bar{r}_1^* [1 - \bar{A}(z_b - z)] \\ F^{\uparrow}(z) = S_0 \mu_0 [1 - A(z_t)] (1 - a_1) G_2 [1 - \bar{A}(z)] , \\ \qquad\qquad z < z_b \end{cases}$$

Figures 28, 29 and 30 show heating rates for cumu[illegible]

AD-A123 396 PARAMETERIZATION OF BROADBAND SOLAR RADIATION TRANSFER IN CLEAR AND CLOUD.. (U) UTAH UNIV SALT LAKE CITY DEPT OF METEOROLOGY K HUTCHISON ET AL. 30 SEP 82 2/2

UNCLASSIFIED SCIENTIFIC-1 AFGL-TR-82-0364 F/G 4/1 NL

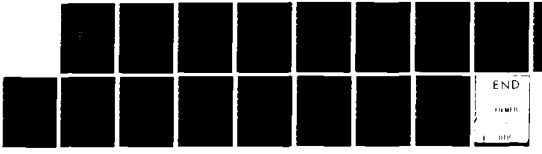

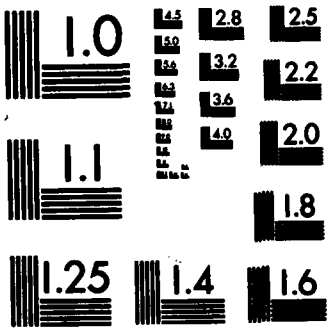

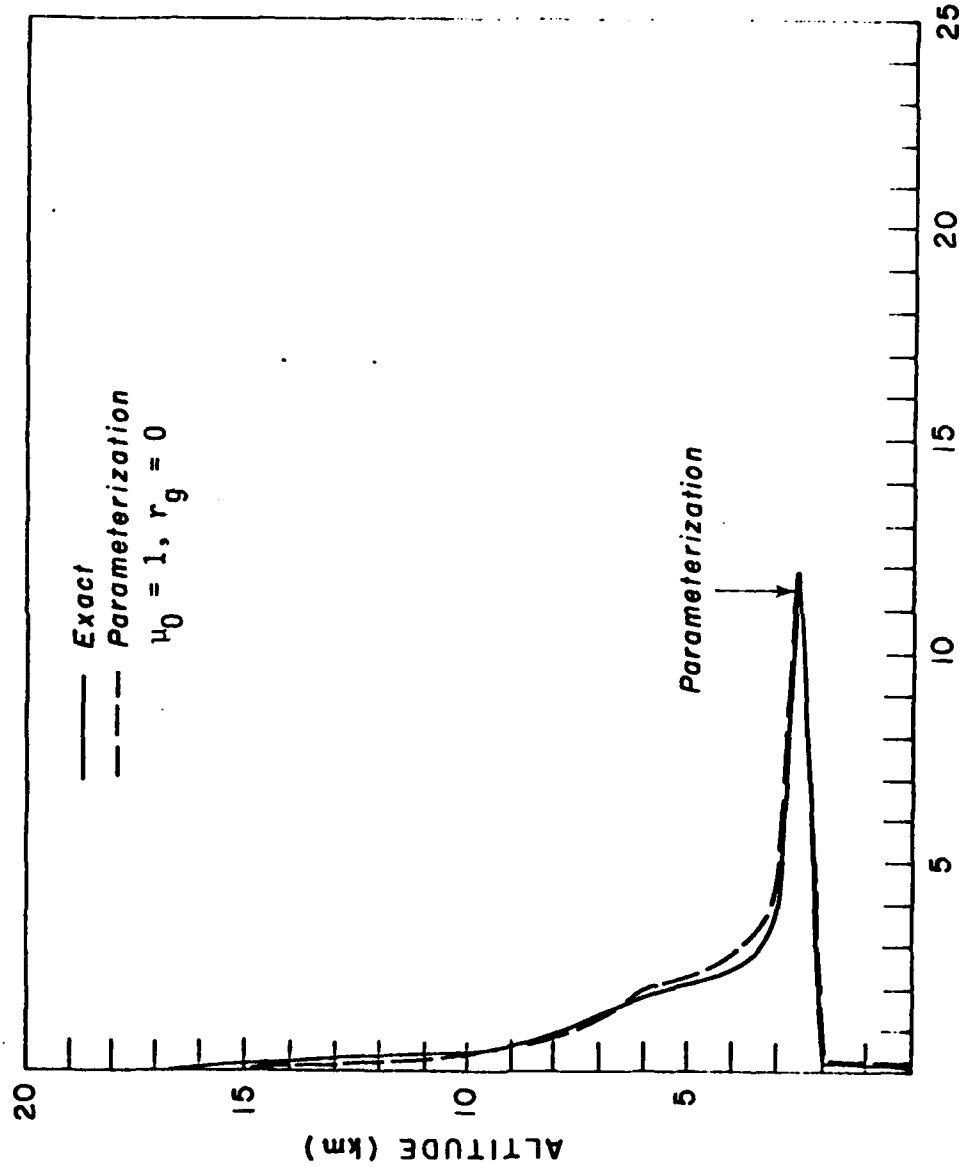

Fig. 28 Water vapor atmospheric and cumulus (2-3 km) cloud heating rates in a midlatitude winter profile.

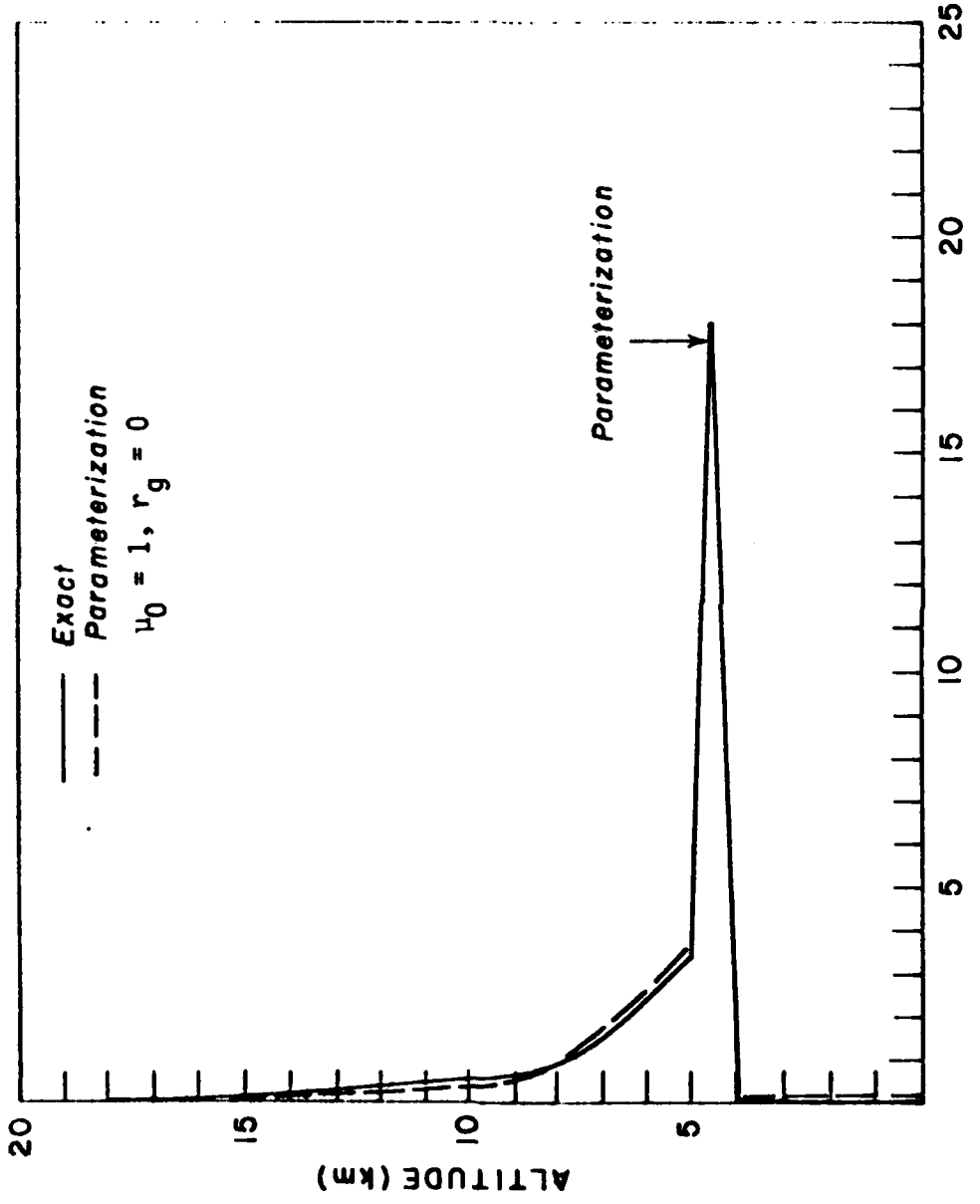

Fig. 29 Water vapor atmospheric and altostratus (4-5 km) cloud heating rates, in a midlatitude winter profile.

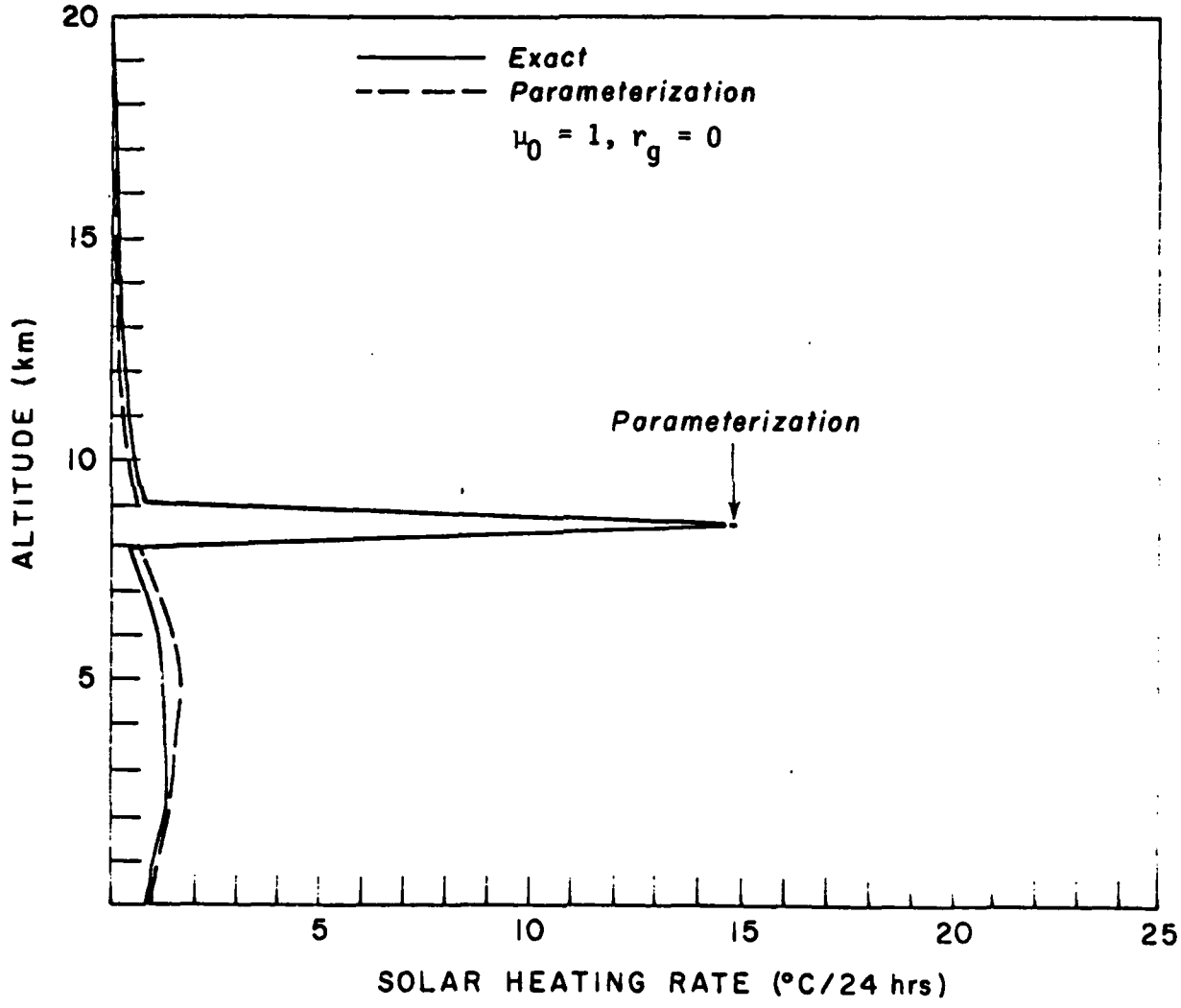

Fig. 30 Water vapor atmospheric and cirrus (8-9 km) cloud heating rates in a mid-latitude winter profile.

and cirrus clouds, respectively in a midlatitude winter atmosphere. Each cloud is one km thick and the sun directly overhead. The surface albedo was set to zero in all cases to maximize the effect of the absorption of the direct solar flux on heating rates in the three areas of the model. Important cloud properties are listed in Table 27.

Heating rates above and below the cloud are generally quite good for all three cloud cases. Poorer agreement is found immediately above the altostratus and cumulus clouds where the diffuse component dominates the heating. The reflection values of these clouds when $\mu_0 = 1$ are 0.823 and 0.763, respectively. Below the cirrus cloud, the parameterized model produces heating rates which are generally larger than the discrete-ordinates model. This results from a more accurate treatment of Rayleigh scatter in the exact method. Rayleigh scattering reduces the downward flux at each level below the cloud as seen in Fig. 16, thus reducing the heating rate in each layer.

The effect of Rayleigh scatter was also analyzed in each cloud layer and found to be most important for clouds which are semi-transparent such as cirrus. This information is also shown in Table 27. The upward flux densities at the base of the cumulus, altostratus, and cirrus clouds were 5.3, 3.0 and 42.5 W m^{-2}, respectively, in each of the cases. The comparable component in the parameterization model was zero in each case. Since, in the more exact model, energy absorbed by the cumulus cloud was 136 W m^{-2}, 164 W m^{-2} for altostratus, and 83 W m^{-2} for the cirrus cloud, it is obvious that Rayleigh scatter is very important in cirrus clouds while insignificant in the cumulus and altostratus clouds.

If the Rayleigh component is ignored, the cloud heating rates agree within 0.36° C/24 hr for cumulus and 0.20° C/24 hr for altostratus.

Table 27 Radiative properties and heating rates for three major cloud types in midlatitude winter atmospheres ($\mu_0 = 1$, $r_g = 0$).

Cloud Type	Cloud Base (km)	Cloud Top (km)	$r_1(\mu_0)$	$t_1(\mu_0)$	Heating Rate (°C/24 hr) Exact	Param. without Rayleigh Effect	Param. with Rayleigh Effect
Cu	2.0	3.0	.7633	.1306	11.88	11.52	11.88
As	4.0	5.0	.8236	.0500	18.04	17.68	18.04
Ci	8.0	9.0	.1211	.8470	14.69	7.3	14.89

However, the cirrus heating rate is 50% lower in the parameterization model. Adding the Rayleigh component to the parameterized model results in exact agreement in the first two cloud types and only a 0.2° C/24 hr error in the cirrus cloud case. Consequently, this Rayleigh scattering correction was parameterized using Eq. (80) for cirrus clouds and the effect is added to the absorptivity of the cirrus cloud.

Increasing the surface albedo allows the multiple reflections and diffuse radiation effects on cloud heating rates and net flux profiles to be studied. In Figs. 31 through 33, heating rate and net flux profiles are shown for a constant surface albedo of 15% (global albedo). Table 28 lists heating rates for the exact and parameterized models as a function of surface albedo. In all cases, the solar zenith angle is one and each cloud is 1 km thick. Agreements of heating rate and net flux profiles between the parameterization method and a more exact method are generally excellent. There is an area of disagreement between the two models in the 8-12 km region of the heating rate curves where the more exact model produces slightly larger results. Cumulus and altostratus net flux profiles contain no flux correction; but, as in the clear atmosphere, Rayleigh scattering in a cirrus cloudy atmosphere requires a correction to generate accurate net flux profiles. In the cirrus case, the upward Rayleigh component is calculated using Eq. (80) and the upward flux at each level between the cloud base and the surface is inferred as is done in the clear sky case.

Analysis of the data presented in Table 28 reveals that this method of accounting for multiple reflections between the cloud and ground actually overestimates the effects which occur in the discrete-ordinates method. The difference between the heating rates produced

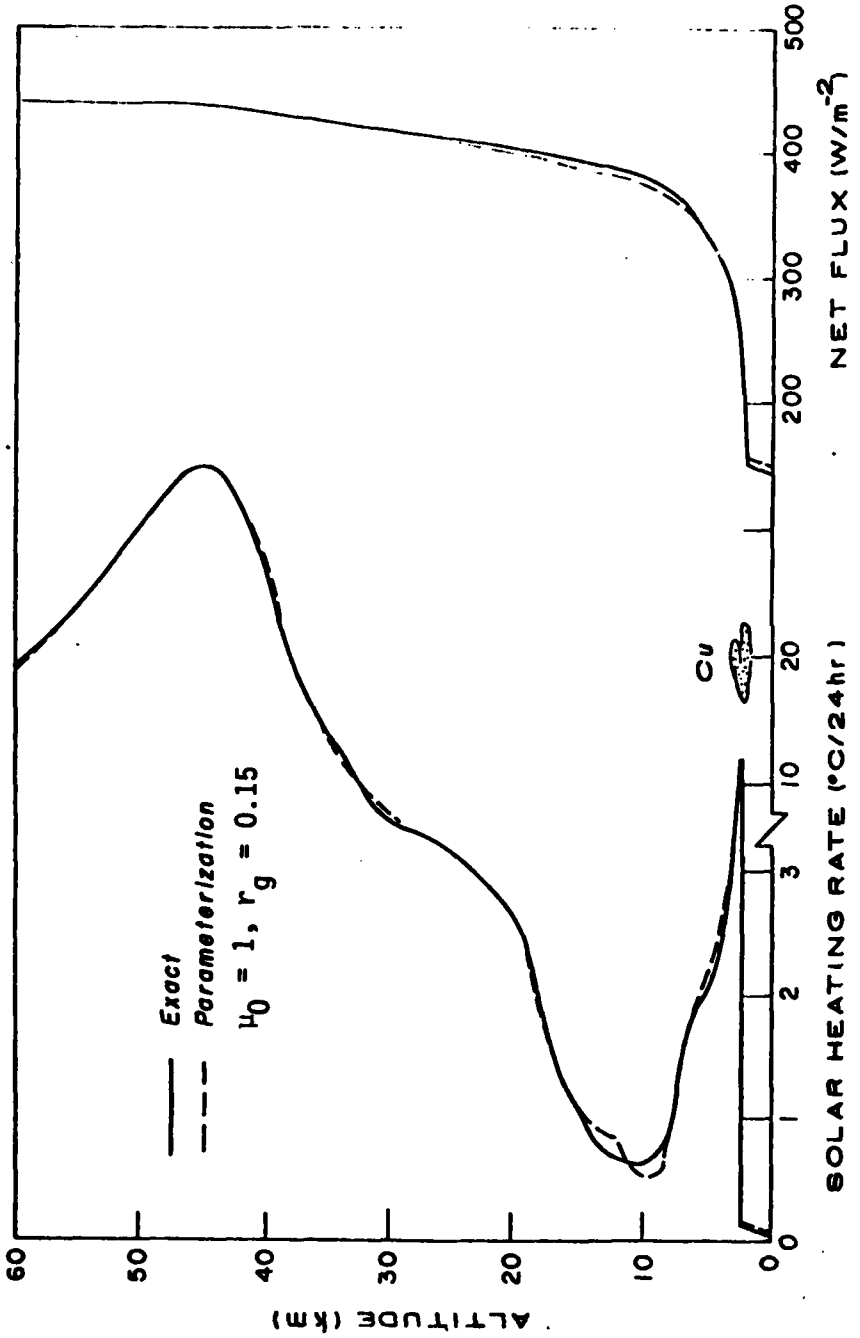

Fig. 31 Heating rate and net flux profiles in a midlatitude winter atmosphere containing a single cumulus (2-3 km) cloud.

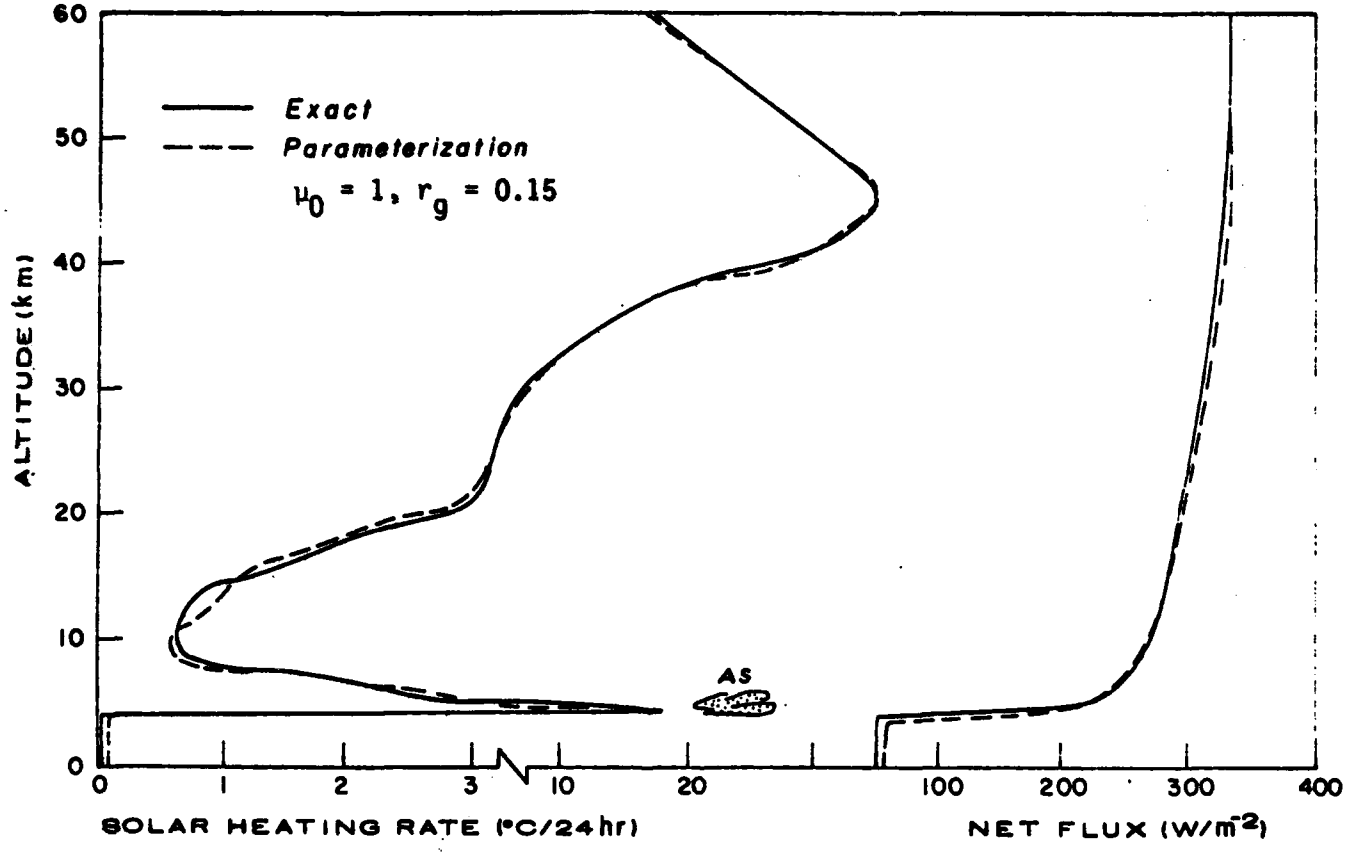

Fig. 32 Heating rate and net flux profiles in a midlatitude winter atmosphere containing a single altostratus (4-5 km) cloud.

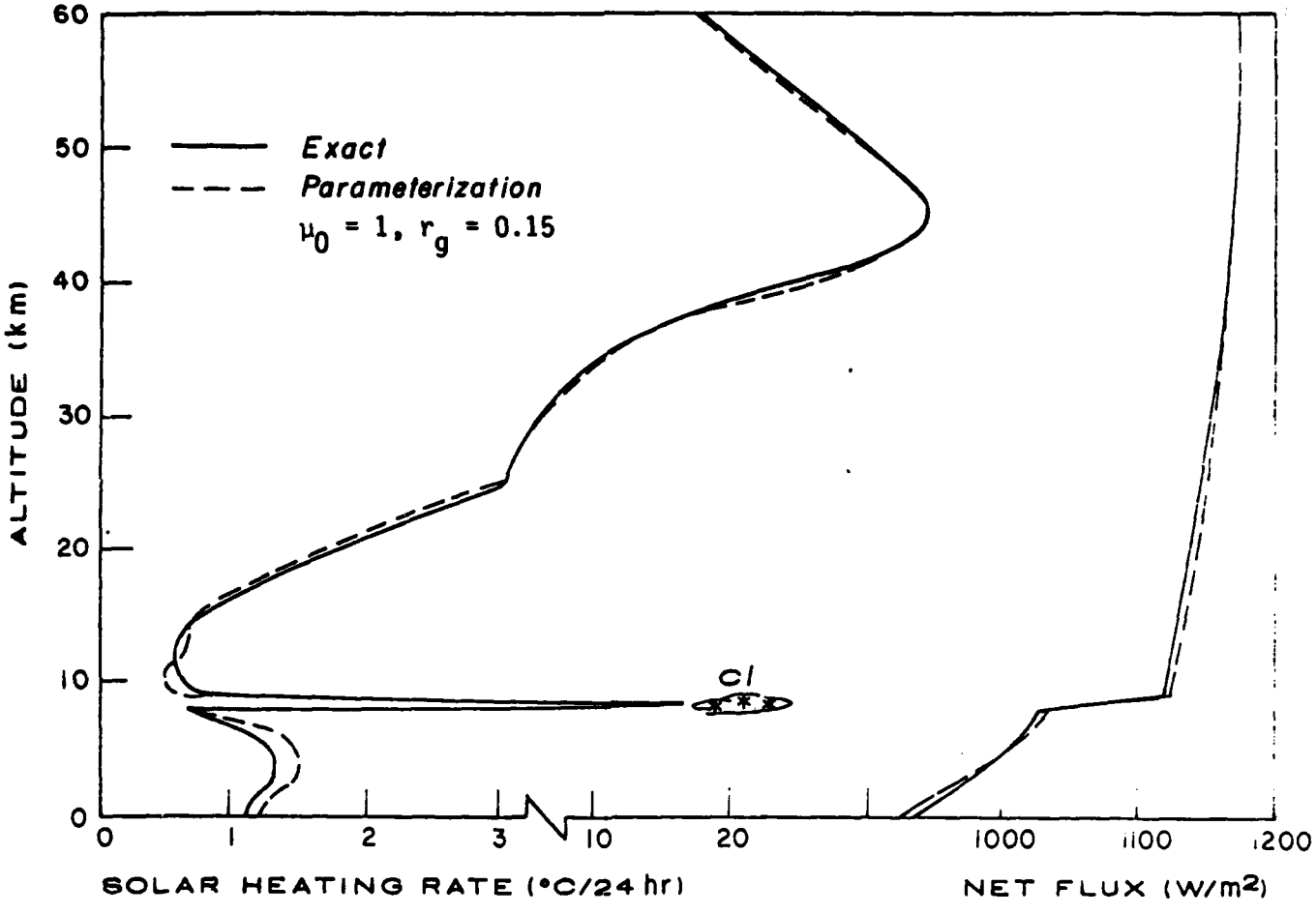

Fig. 33 Heating rate and net flux profiles in a midlatitude winter atmosphere containing a single cirrus (8-9 km) cloud.

Table 28 Effect of the surface albedo on the cloud heating rate in midlatitude winter atmospheres ($\mu_0 = 1$).

Cloud Type	Cloud Base (km)	Cloud Top (km)	Heating Rate (°C/24 hr) Exact	Heating Rate (°C/24 hr) Param.	r_g	Exact - Param.
Cu	2.0	3.0	11.88	11.54	0.00	.34
Cu	2.0	3.0	11.96	11.79	0.15	.17
As	4.0	5.0	18.04	17.68	0.00	.36
As	4.0	5.0	18.11	17.81	0.15	.30
As	4.0	5.0	18.25	19.27	0.80	-1.02
Ci	8.0	9.0	14.69	14.89	0.00	-.20
Ci	8.0	9.0	15.57	16.21	0.15	-.64
Ci	8.0	9.0	22.31	25.16	1.00	-2.85

by the exact and parameterization models for cumulus and altostratus clouds when the surface albedo was zero has been reduced by increasing the ground albedo to 15%. If the albedo is increased to 80% in the altostratus case, the parameterization model produces a heating rate about one degree larger than the exact model. The error in the multiple reflection effect is more clearly seen by observing this difference in the cirrus cloud case. The difference grows from -0.2, to -2.85° C/24 hr as the ground albedo is increased from zero to 100%. The difference in the multiple reflection effect of the parameterization model probab' results from a complicated relationship between ground albedo, atmospheric absorptivity of diffuse radiation, and Rayleigh scattering.

Section 6

SUMMARY AND CONCLUSIONS

It was previously stated that the parameterization approach to solving the solar radiative transfer equation is necessary because the more exact approximations, such as the discrete-ordinates method, are far too time consuming and expensive to use in global circulation models of the earth-atmosphere system. However, many of the earlier attempts at parameterizing the solar radiative transfer equations were too simple and known relationships, such as solar zenith angle and liquid water content dependence on the reflection and transmission of clouds, were not accurately considered. The primary objective of this reasearch was to develop a parameterization model which would generate reliable and economical solar heating rate and net flux profiles for inclusion into a global circulation model. The parameterization model developed in this report is based on physical and mathematical principles which govern radiative transfer in planetary atmospheres under clear and cloudy sky conditions.

First, consider the theoretical principles upon which this parameterization model is based. Under clear sky conditions, water vapor heating rates are assumed to result from gaseous absorption only. This assumption is consistent with other parameterization models. Heating rate comparisons between the parameterization and discrete-ordinates methods generally agreed within 0.2° C/24 hr for all solar zenith angles and any surface albedo. Ozone heating rates are known

to be dependent upon Rayleigh scatter and the surface albedo. Consequently, ozone was modeled as an absorbing layer overlaying a reflecting layer as described by Dave and Furukawa (1967), Lacis and Hansen (1974), and others. Ozone heating rate comparisons between the more exact and parameterization models were very good with about 1° C/24 hr being the largest disagreement in a profile which had a maximum heating of 35° C/24 hrs. It was found that a correction to the net fluxes in a clear atmosphere must be made if profiles generated by the two models are to agree well. The correction is necessary because Rayleigh scatter depletes the downward direct solar beam and increases the upward diffuse solar beam in the troposphere where molecular number densities are large.

In cloudy atmospheres, this parameterization model allows much more flexibility to designers of general circulation models while maintaining its strong theoretical basis. Most parameterization models assign constants to cloud reflections and transmissions or use a form of the two-stream approximation to calculate these properties from the optical depth of the cloud. Although the latter approximation is much more advanced than assigning climatological values to clouds based upon their type, it does not allow the solar zenith angle dependence upon cloud reflection and transmission, which can be rather large, to be taken into account. This parameterization method does consider this dependence. Additionally, cloud radiation properties are parameterized as a function of liquid water/ice content. Since global circulation models now forecast relative humidity and temperature fields, it is highly desirable that the parameterization of cloud radiative properties also possess a temperature dependence. This parameterization is the

only model known of at this time which accounts for the temperature dependence on the cloud radiative properties.

The modified adding method used in this parameterization model treats direct and diffuse radiative streams separately which allows highly accurate heating rates to be computed outside the clouds. Multiple reflection inside the cloud-reflection surface system have been considered and internal net fluxes are calculated at each level within the system. It was noted that the adding method, in its present form, tends to overestimate the multiple reflections effect on the cloud heating rate in an atmosphere containing a single cloud. However, the error is not significant when dealing with normal surface albedos in the 0.07-0.5 range.

Next, consider the computational efficiency of the parameterization model against that of the discrete-ordinates method. Table 29 depicts computational statistics for the discrete-ordinates method and the parameterization method developed in this research project. The exact method used 42 spectral band intervals to describe the solar spectrum. It was run for one solar zenith angle and for various numbers of layers in the atmospheric profile. One cloud was present in all the models shown in the table. The results readily demonstrate the need for parameterizing the radiative processes in GCM where solar heating rate calculations are needed at each grid point and for each time step. As the number of layers in the atmospheric profile increases the core size and CPU time required to compute the solar heating increases dramatically as in a non-linear fashion. The exact model will compute the solar heating rate in 10 layers for a single grid point and a single zenith angle in approximately five minutes

Table 29 Computation Statistics for Exact and Parameterization Models on UNIVAC 1110

Model	# Layers	Core Size	CPU Time	Cost
Exact	10	60 K	4 min	$17
Exact	15	77 K	12 min	$60
Exact	20	96 K	26 min	$165
Exact	25	120 K	50 min	$375
Parameterized	60	40 K	9 sec	$1.20

using nearly 60 K of storage in the UNIVAC 1110 here at the University of Utah. Increasing to 15 layers almost triples the CPU time required for the computations. This occurs because the unknowns in the system of equations, described in Section three, increase from 40 to 60. The core size increases significantly since numerous arrays are also increased from 40 to 60. For exactly the same reasons, increasing the number of layers in the atmosphere to 25 layers requires nearly an hour of CPU time at well over 100 K to solve the system of equations for only one solar zenith angle. Because a minimum of 20-25 layers are needed to adequately define the solar heating rate up to 60 km in a cloudy atmosphere, the exact method obviously is of little value in a global model.

Since the parameterization model uses analytical functions rather than the computationally slower and more inaccurate finite difference schemes, it can compute solar heating rates in a 60 layered atmospheric model in only about nine CPU seconds at less than 40 K on the UNIVAC 1110. With a nearly linear relationship between the number of calculations and the number of layers in the parameterization model, it is estimated that the parameterization model would execute in about 3 CPU seconds if the number of layers were reduced to 20. Similarly, the CPU should drop to about 13 K storage. Clearly, the parameterization model computes solar heating rates several orders of magnitude faster than the exact method.

The parameterization model is soundly based upon radiative principles which govern planetary atmospheres and is considerably more physically reliable than parameterizations currently being used in global circulation models especially when clouds are involved. The basic contribution of this research work is that maximum flexibility

is built into the cloud radiative properties since both cloud transmission and reflection remain functions of three independent cloud parameters: vertical liquid water/ice content, solar zenith angle, and mean cloud temperature. Heating rates are computed by analytical expressions at precise points rather than by finite difference approximations. Finally, separating the direct and diffuse solar flux allows accurate heating rates to be computed above, below, and between clouds.

REFERENCES

Dave, J.V. and P.M. Furukawa, 1967: The effects of scattering and ground reflection on the solar energy absorbed by ozone in a Rayleigh atmosphere. J. Atmos. Sci., 24, 174-181.

Fouquart, Y. and B. Bonnel, 1980: Computations of solar heating of the earth's atmosphere: A new parameterization. Con. Atmos. Phys., 53, 35-62.

Freeman, K.P. and K.N. Liou, 1979: Climatic effects of cirrus clouds. Advances in Geophys., 21, 231-287.

Geleyn, J.F. and A. Hollingsworth, 1979: An economical analytical method for the computation of the interaction between scattering and line absorption of radiation. Con. Atmos. Phys., 52, 1-16.

Goody, R.M., 1964: Atmospheric Radiation. Clarendon Press, Oxford, 436 pp.

Haltiner, G.J. and R.T. Williams, 1979: Numerical Weather Prediction and Dynamic Meteorology. Wiley, New York, 477 pp.

Haurwitz, B., 1948: Insolation in relation to cloud type. J. Meteor., 5, 110-113.

Howard, J.N., D.E. Burch and D. Williams, 1956: Infrared transmission of synthetic atmospheres, Parts I-V. J. Opt. Soc. Amer., 46, 186-190, 237-241, 242-245, 334-338, 452-455.

Howard, J.N., J.I.F. King and P.R. Gast, 1961: Thermal radiation. Handbook of Geophysics. Macmillan, New York, Chapter 16.

Inn, E.C.Y. and Y. Tanaka, 1953: Absorption coefficient of ozone in the ultraviolet and visible regions. J. Opt. Soc. Amer., 43, 870-873.

Katayama, A., 1972: A simplified scheme for computing radiative transfer in the troposphere. Tech. Rept. No. 6, Department of Meteorology, University of California at Los Angeles.

Lacis, A.A. and J.E. Hansen, 1974: A parameterization for the absorption of solar radiation in the earth's atmosphere. J. Atmos. Sci., 31, 118-133.

Liou, K.N., 1973: A numerical experiment on Chandrasekhar's discrete ordinate method for radiative transfer: Applications to cloudy and hazy atmospheres. J. Atmos. Sci., 30, 1303-1326.

Liou, K.N., 1976: On the absorption, reflection, and transmission of solar radiation in cloudy atmospheres. J. Atmos. Sci., 33, 798-805.

Liou, K.N., 1980: An Introduction to Atmospheric Radiation. Academic Press, New York, 404 pp.

Liou, K.N. and T. Sasamori, 1975: On the transfer of solar radiation in aerosol atmospheres. J. Atmos. Sci., 32, 2166-2177.

Liou, K.N. and G.D. Wittman, 1979: Parameteization of the radiative properties of clouds. J. Atmos. Sci., 36, 1261-1273.

Manabe, S. and F. Möller, 1961: On the radiative equilibrium and heat balance of the atmosphere. Mon. Weather Rev., 89, 503-532.

Manabe, S. and R.F. Strickler, 1964: Thermal equilibrium of the atmosphere with a convective adjustment. J. Atmos. Sci., 21, 361-385.

McClatchey, R.A., R.W. Fenn, J.E. Selby, F.E. Vol z and J.S. Garing, 1972: Optical properties of the atmosphere. (Third ed.) AFCRL-72-0497.

Park, J.H. and J. London, 1974: Ozone photochemistry and radiative heating of the middle atmosphere. J. Atmos. Sci., 31, 1898-1916.

Sasamori, T., J. London and D.V. Hoyt, 1972: Radiation budget of the southern hemisphere. Meteor. Monog., 13, No. 35, 9-23.

Sommerville, R.C., P.H. Stone, M. Halem, J.E. Hansen, J.S. Hogan, L.M. Druyan, G. Russell, A.A. Lacis, W.J. Quirk and J. Tennenbaum, 1974: The GISS model of the global atmosphere. J. Atmos. Sci., 31, 84-117.

Thekaekara, M.P., 1974: Extraterrestrial solar spectrum, 3000-6100 Å at 1-Å intervals. Appl. Opt., 3, 518-522.

van de Hulst, H.C. and K. Grossman, 1968: Multiple light scattering in planetary atmospheres. In The Atmospheres of Venus and Mars (J.C. Brandt and M.B. McElroy, eds.), pp. 35-55. Gordon and Breach, New York.

Vigroux, E., 1953: Contributions a l'etude experimentale de l'absorption de l'ozone. Annales de Physique, 8, 709-715.

Yamamoto, G., 1961: Direct absorption of solar radiation by atmospheric water vapor, carbon dioxide, and molecular oxygen. J. Atmos. Sci., 19, 182-188.